

1 Dear Dr. Maenhaut,

2

3 We kindly thank you for taking our manuscript into consideration. We have  
4 addressed the comments raised by you and prepared a new version of the  
5 manuscript and supplement. For clarity, a point-by-point response to the comments  
6 and versions of the manuscript and supplement in which our modifications are  
7 visible, are enclosed below. Your comments have been very helpful to improve the  
8 quality of the manuscript, and we would like to thank you for this. Together with our  
9 major revisions in response to the partially critical but very helpful comments made  
10 by the two reviewers, we are convinced our manuscript now provides an adequate  
11 presentation of our ClearfLo results along with a thorough discussion of the  
12 associated uncertainties.

13

14 Kind regards,

15 Suzanne Visser and co-authors

16

1 **Comment #1:**

2 *The very large discrepancy between the SR-XRF RDI and the ICP-MS filter data*  
3 *for the elements Na and Mg, with the SR-XRF data being a factor 2.5 larger than*  
4 *the ICP-MS data, points to a very serious problem. One source of uncertainty,*  
5 *which the authors fail to discuss in their manuscript, is self-absorption of the*  
6 *emitted X-rays for the lightest elements (especially Na and Mg). Very few details*  
7 *are given on the calibration of the SR-XRF measurements. On page 7, lines 18-*  
8 *35, it is said that use was made of multi-element standards. It is not stated how*  
9 *these were prepared, but reference is given to three earlier published papers. In*  
10 *the most recent one (i.e., Richard et al., 2010), it is said that multi-element*  
11 *standards were prepared from multi-element solutions using a high-resolution*  
12 *printing process. I presume that the standards were prepared in the same*  
13 *manner for the current work. How did the standards look like? Was a*  
14 *homogeneous thin layer created? If so, how thick was it and was correction made*  
15 *for self-absorption of the emitted X-rays within the layer? Or did the layer consist*  
16 *of individual particles of larger size than the aerosol particles in the RDI samples.*  
17 *In any case, X-ray self-absorption effects in general and those caused by particle*  
18 *size effects should not be neglected for the light elements (Na, Mg) in X-ray*  
19 *emission spectrometric (XRS) analysis. For a discussion of self-absorption*  
20 *because of the particle size effects in XRS analysis, I refer to a paper by*  
21 *Formenti et al. (JGR, 115, D01203, 2010) and references cities therein. If no*  
22 *correction for self-absorption is made in XRS, the data for the lightest elements*  
23 *are underestimated. It is very strange that the SR-XRF data for Na and Mg are*  
24 *much larger than the ICP-MS data. Could it be that the X-ray attenuation for Na*  
25 *and Mg in the standards was much larger than in the RDI samples and that no*  
26 *correction was made for this? In any case, I wonder how accurate the SR-XRF*  
27 *calibration factors for the elements Na and Mg are. An alternative way of*  
28 *calibrating is through making use of Micromatter standards*  
29 *(www.micromatter.com). These consist of a homogeneous thin layer of known*  
30 *thickness and composition, so that the correction for X-ray self-absorption can*  
31 *easily be calculated.*

32  
33 **Response:**

34 We greatly appreciate this extended comment about the discrepancy between SR-  
35 XRF and ICP data for Na and Mg. The Editor points to self-absorption as a potential  
36 reason for this discrepancy. Although we were aware of self-absorption effects in the  
37 lightest elements, we had previously assumed that these effects cancel out between  
38 ambient samples and calibration standards due to their similar foil loadings and  
39 composition, identical foil substrate, and identical SR-XRF measurement conditions.

40 However, a closer inspection of the calibration standards revealed that the printing  
41 process (similar to that of Richard et al., 2010), yields a layer of particles with  
42 diameters up to 45  $\mu\text{m}$  covering an estimated 15-20 % of the carrier substrate. The  
43 estimated average particle size is  $9 \pm 5 \mu\text{m}$  (geometric mean of the volume size  
44 distribution). This is much larger than the geometric mean of the ambient samples;  
45 5.0, 1.6 and 0.55  $\mu\text{m}$  for  $\text{PM}_{10-2.5}$ ,  $\text{PM}_{2.5-1.0}$  and  $\text{PM}_{1.0-0.3}$  fractions, respectively.  
46 Therefore, we agree that self-absorption correction factors should indeed be applied  
47 to the XRF data.

48  
49 We will address this issue by including the following text at the end of Section 2.2.1,  
50 at p. 8 of the current manuscript.

1 “XRF is sensitive to self-attenuation of fluorescence radiation in the sample and  
2 depends on the sample composition and density, as well as particle layer thickness  
3 or particle size. The PM sample thickness of the coarse and intermediate fractions  
4 was maximally 0.7-1.5  $\mu\text{m}$  at a maximum concentration of  $10 \mu\text{g m}^{-3}$  total PM mass  
5 for each sample. For these fractions, self-absorption therefore mainly occurs within  
6 the individual particles (geometric mean of 5 and 1.6  $\mu\text{m}$  for  $\text{PM}_{10-2.5}$  and  $\text{PM}_{2.5-1.0}$   
7 fractions, respectively). For the fine fraction the PM layer is several micrometres  
8 thick, resulting in absorption inside the PM layer. However, most mass of the lightest  
9 elements (Na-Si) is restricted to the coarse and intermediate fraction. We therefore  
10 neglect self-absorption effects in the fine fraction samples. The calculated layer  
11 thickness of the dried calibration solution on the calibration standards is negligible at  
12 3-60 nm, but the particle size of the dried droplets shows a geometric mean volume  
13 size distribution of  $9 \pm 5 \mu\text{m}$  and is therefore relevant for self-attenuation. Attenuation  
14 factors (AF) were calculated for the calibration standards as well as for the coarse  
15 and intermediate fraction samples for Na, Mg, Al and Si, as a function of density,  
16 mass attenuation coefficient and particle size, according to a simple attenuation  
17 model (Table 2; Formenti et al., 2010). The AF of heavier elements were negligible  
18 within the measurement uncertainties. The attenuation of the calibration standards is  
19 taken into account for all samples, and additional corrections are applied to the  
20 coarse and intermediate samples. Calzolari et al. (2010) found comparable self-  
21 absorption effects for samples of different composition, total loading and sampling  
22 site. Because the elemental composition and particle size distribution of each sample  
23 are unknown, we assume a uniform correction for each element within a given size  
24 fraction. The overall AF are 0.22-0.52, 0.32-0.55, 0.43-0.61 and 0.51-0.64 for Na,  
25 Mg, Al and Si, respectively (calculated as correction factor of calibration  
26 standard/sample).”

27  
28 **Table 2.** Self-absorption correction factors.

	Geometric mean diameter ( $\mu\text{m}$ )	Density <sup>a</sup> ( $\text{g cm}^{-3}$ )	Na <sup>b</sup>	Mg <sup>b</sup>	Al <sup>b</sup>	Si <sup>b</sup>
Calibration standard 1	9	2.19	0.22 <i>0.49</i>		0.43 <i>0.23</i>	
Calibration standard 2	9	2.27		0.32 <i>0.33</i>		0.51 <i>0.17</i>
$\text{PM}_{10-2.5}$ sample	5	2.00	0.43 <i>0.40</i>	0.58 <i>0.25</i>	0.70 <i>0.15</i>	0.79 <i>0.10</i>
$\text{PM}_{2.5-1.0}$ sample	1.6	2.00	0.74 <i>0.40</i>	0.83 <i>0.25</i>	0.89 <i>0.15</i>	0.93 <i>0.10</i>

29 <sup>a</sup> Average density of the calibration standards and of ambient aerosol. The composition of  
30 calibration standard 1 is  $\text{Na}_{3.76}\text{Al}_{3.76}\text{P}_{3.76}\text{Cl}_{3.76}\text{Ca}_{3.76}\text{CoN}_8\text{O}_{24}$ , of calibration standard 2  
31  $\text{Mg}_{3.76}\text{Si}_{3.76}\text{S}_{3.76}\text{K}_{3.76}\text{Ca}_{3.76}\text{CoN}_7\text{O}_{21}$ , and of ambient samples  $\text{C}_{39}\text{H}_{29}\text{N}_{10}\text{O}_{18}\text{S}_3\text{Fe}$ .

32 <sup>b</sup> Attenuation factors and *a* (italic values,  $\mu\text{m}^{-1}$ ;  $a = 2/3 \cdot \mu \cdot \rho$  with  $\mu$  the mass attenuation  
33 coefficient ( $\text{cm}^2 \text{g}^{-1}$ ) and  $\rho$  the particle mass density ( $\text{g cm}^{-3}$ )) according to Eq. (4) in Formenti  
34 et al. (2010).

35  
36 The correction factors are applied to all ambient samples for Na, Mg, Al and Si. With  
37 this corrected XRF data, XRF data and ICP filter data are in good agreement (Na  
38 factor 1.30, Mg factor 1.09, Al factor 0.89 for XRF to ICP data). This shows that self-  
39 absorption effects were indeed the source of the discrepancies between both  
40 measurement techniques.

41 All affected tables and figures have been updated accordingly, as well as values in  
42 the manuscript and supplement. In addition, the text has been adjusted.

1 The first paragraph of Section 3, p. 9 becomes:

2 “Here we compare RDI-SR-XRF data with independent filter data (24 h PM<sub>10</sub> trace  
3 element data analysed with ICP-MS; roughly 9 % uncertainty at a 95 % confidence  
4 interval) for 18 elements collected at MR and NK (no filter data was available at DE).  
5 For this comparison, the three size ranges of the RDI were summed up to total PM<sub>10</sub>  
6 and averaged to the filter collection period. Details of the intercomparison results can  
7 be found in Supplement C. In short, the majority of the elements (Al, Ca, Ti, Mn, Fe,  
8 Cu, Zn, Sr, Sb, Ba) agree within approximately ± 50 % with Pearson’s  $R > 0.78$ . Na  
9 and Mg agree as well, but have higher uncertainties due to self-absorption  
10 corrections. For the other elements, disagreement can be attributed to low or  
11 unknown filter sample extraction efficiencies (Ni, Mo) and differences in the particle  
12 size range sampled by the two measurement techniques (K, V, Sn, Pb). However, all  
13 elements are retained in the ensuing analysis as (1) they yield internally consistent  
14 results, as described in the following sections; (2) the ensuing analysis relies on  
15 relative changes/ratios per element across sites and is therefore not affected by a  
16 systematic bias in absolute magnitude.”

17

18 Point 4 and the following paragraph of Section 3, p. 10 become:

19 “4. SR-XRF measurement precision is affected by sample inhomogeneity, spectral  
20 analysis and self-absorption correction uncertainties. Sample inhomogeneity was  
21 assessed by Bukowiecki et al. (2009c) and found to contribute ± 20 % uncertainty.

22 For most elements, except Mn and the lightest elements, sample inhomogeneity is  
23 the largest source of uncertainty. Mn is affected by spectral analysis uncertainties  
24 due to peak overlap with Fe, which is present in much higher concentrations.  
25 Therefore, a small bias in the energy calibration as function of detector channel leads  
26 to a large change in the peak area of Mn. Self-absorption effects are a significant  
27 source of uncertainty for the lightest elements (Na-Si), but the good comparisons to  
28 the filter data suggest that the corrections lead to reasonable results. All data points  
29 lie well above their element detection limits, resulting in negligible uncertainties from  
30 the signal strength. In addition, RDI-SR-XRF measurements (both absolute/fractional  
31 and relative/ratio) are affected by atmospheric variability. This variability is likely the  
32 predominant source of the data spread evident in Table 3 and the following  
33 analyses.”

34

35 The description of the comparison between XRF and ICP data in Supplement C  
36 “Data intercomparison”, based on Fig. S3, Table S2 and Table S3 (see also  
37 response to Comment #2) has been changed accordingly. We would like to refer to  
38 the new version of the supplement, or to p. 58-63 of this document to see the  
39 changes.

40

41 The Editor also refers to the use of Micromatter standards. We agree that the use of  
42 certified reference materials for the XRF data calibration would, in theory, be helpful.  
43 These standards can certainly reduce the uncertainties in the self-absorption  
44 corrections, but this would require the re-measurement of all ambient samples and  
45 these calibration materials by use of identical geometry. At this stage, we are  
46 confident that by addressing the self-absorption effects of Na, Mg, Al and Si of both  
47 the multi-element standards and the ambient samples, we are able to accurately  
48 calibrate our samples, although with higher uncertainties.

49

1 **Comment #2:**

2 *Considering what I wrote above, self-absorption effects cannot be neglected at all*  
3 *as a source of uncertainty on page 10. It also follows that the estimated total*  
4 *uncertainties for the lightest elements (Na, Mg) should be substantially larger*  
5 *than those for an element as Fe; as a consequence, Table S3 needs to be*  
6 *modified.*

7

8 **Response:**

9 As a result of the response to Comment #1, the uncertainties based on corrections of  
10 self-absorption effects are estimated and included in the manuscript and supplement.  
11 The uncertainties mainly arise from the self-absorption effects in the calibration  
12 standards. The particle size of the dried droplets shows a geometric mean of the  
13 volume size distribution of  $9 \pm 5 \mu\text{m}$ . This estimation is based on the microscopic  
14 analysis of the particle size on the calibration standards. The resulting uncertainties  
15 in the applied correction factors are 54, 49, 41 and 35 % for Na, Mg, Al and Si,  
16 respectively. We assume a constant average size distribution of the coarse and  
17 intermediate fraction ambient samples. Therefore, and due to the smaller average  
18 size of the particles in the samples, the additional uncertainties from self-absorption  
19 corrections in the samples become negligible compared to the calibration standards.

20 We refer to the response to Comment #1 to see the changes in the text as a result of  
21 including self-absorption corrections and the associated uncertainties.

22

23 Table S3 in the supplement has been updated accordingly:

24

25 **Table S3.** Estimated total uncertainty (% of measured value) of the calculated element  
26 concentrations per size fraction, and detection limits for each element ( $\text{ng m}^{-3}$ ).

Element	PM <sub>10-2.5</sub> (%) <sup>a</sup>	PM <sub>2.5-1.0</sub> (%) <sup>a</sup>	PM <sub>1.0-0.3</sub> (%) <sup>a</sup>	DL ( $\text{ng m}^{-3}$ ) <sup>b</sup>
Na <sup>c</sup>	59	59	60	2.552
Mg	55	55	55	0.962
Al	48	48	48	1.709
Si	43	43	43	0.420
P	25	25	25	0.118
S	24	24	24	0.503
Cl	24	24	24	0.158
K	24	24	24	0.031
Ca	21	21	21	0.267
Ti	24	26	27	0.024
V	30	30	24	0.008
Cr	27	27	26	0.015
Mn	83	69	46	0.042
Fe	21	21	21	0.033
Ni	22	22	21	0.005
Cu	21	21	21	0.028
Zn	21	21	21	0.058
Br	21	21	21	0.117
Sr	21	21	21	0.036
Zr	21	21	21	0.036
Mo	21	21	21	0.037
Sn	21	21	21	0.061
Sb	21	21	21	0.052
Ba	21	21	21	0.254
Pb	21	21	21	0.137

1 <sup>a</sup> Combination of uncertainties regarding sample inhomogeneity (20 %), self-absorption  
2 corrections (Na-Si 54-35 %)<sup>d</sup>, RDI flow rate (5 %), absolute and relative calibration (Na-K 13  
3 %, Ca-Pb 2 %) and spectral analysis specific per element and size fraction (median  
4 uncertainties for all data points).

5 <sup>b</sup> Taken as 3x the standard deviation of the spectra signals used for continuum corrections.

6 <sup>c</sup> Na uncertainties might be underestimated due to the overlap with the L lines of Ni, Cu and  
7 Zn. In the current analysis the ratio of the L $\alpha$  to K $\alpha$  lines are determined empirically, and  
8 quantification of the associated uncertainties is under investigation.

9 <sup>d</sup> Uncertainties regarding self-absorption corrections are based on the microscopic analysis of  
10 the particle size on the calibration standards. The particle size of the dried droplets shows a  
11 geometric mean of the volume size distribution of 9  $\mu\text{m}$ , and 50 % of the particles are in the  
12 range 4-14  $\mu\text{m}$ .

### 14 **Comment #3:**

15 *Figure S3b and Table S2 indicate that the SR-XRF data for V are much lower*  
16 *than the ICP-MS filter data for this element. Yet, on page 6, bottom paragraph, of*  
17 *the Supplement the authors suggest that the ICP-MS data for V could be*  
18 *underestimated. But if this would indeed be the case, the discrepancy between*  
19 *the SR-XRF data and correct ICP-MS data would even become larger. Was there*  
20 *no problem of (serious) spectral interference for V in the SR-XRF analysis? Could*  
21 *it not be that the V K $\alpha$  peak area was underestimated for the RDI samples?*

### 23 **Response:**

24 We agree that the explanation of the comparison between SR-XRF and ICP-MS data  
25 for V is inconsistent. The extraction efficiency of ICP-MS is unknown for this element,  
26 but correct ICP data would indeed only lead to larger V concentrations. The spectral  
27 sensitivity analysis for V shows an uncertainty of 13-22 % in the detection of the K $\alpha$   
28 line, dependent on the size fraction. Although this is considerably higher than for  
29 most other elements (only a few percent), we believe that this is not the main reason  
30 for the large underestimation for the XRF data compared to the ICP data. However, V  
31 is typically emitted in the fine fraction from fuel-oil combustion or industrial sources.  
32 Therefore, it is more likely that the XRF data strongly underestimate the V  
33 concentrations, in line with K, Sn and Pb due to the differences in the particle size  
34 range sampled by both measurement techniques. As a result, it would be more  
35 accurate to group V with K, Sn and Pb in Fig. S3d. This has been done in the new  
36 supplement and the text in Supplement C has been changed accordingly.

### 38 **References**

39 Bukowiecki, N., Richard, A., Furger, M., Weingartner, E., Aguirre, M., Huthwelker, T.,  
40 Lienemann, P., Gehrig, R., and Baltensperger, U.: Deposition uniformity and particle  
41 size distribution of ambient aerosol collected with a rotating drum impactor, *Aerosol*  
42 *Sci. Technol.*, 43, 891-901, 2009c.

43 Calzolari, G., Chiari, M., Lucarelli, F., Nava, S., and Portarena, S.: Proton induced  
44 gamma-ray emission yields for the analysis of light elements in aerosol samples in an  
45 external beam set-up, *Nucl. Instrum. Methods Phys. Res. Sect. B-Beam Interact.*  
46 *Mater. Atoms*, 268, 1540-1545, 2010.

47 Formenti, P., Nava, S., Prati, P., Chevaillier, S., Klaver, A., Lafon, S., Mazzei, F.,  
48 Calzolari, G., and Chiari, M.: Self-attenuation artifacts and correction factors of light  
49 element measurements by X-ray analysis: Implication for mineral dust composition  
50 studies, *J. Geophys. Res.-Atmos.*, 115, 8, doi:10.1029/2009jd012701, 2010.

1 Richard, A., Bukowiecki, N., Lienemann, P., Furger, M., Fierz, M., Minguillon, M. C.,  
2 Weideli, B., Figi, R., Flechsig, U., Appel, K., Prevot, A. S. H., and Baltensperger, U.:  
3 Quantitative sampling and analysis of trace elements in atmospheric aerosols:  
4 impactor characterization and synchrotron-XRF mass calibration, Atmos. Meas.  
5 Tech., 3, 1473-1485, 2010.

6  
7

1 **Kerb and urban increment of highly time-resolved**  
2 **trace elements in PM<sub>10</sub>, PM<sub>2.5</sub> and PM<sub>1.0</sub> winter aerosol**  
3 **in London during ClearfLo 2012**

4

5 **S. Visser<sup>1</sup>, J.G. Slowik<sup>1</sup>, M. Furger<sup>1</sup>, P. Zotter<sup>1</sup>, N. Bukowiecki<sup>1</sup>, R. Dressler<sup>2</sup>, U.**  
6 **Flechsig<sup>3</sup>, K. Appel<sup>4\*</sup>, D.C. Green<sup>5</sup>, A.H. Tremper<sup>5</sup>, D.E. Young<sup>6</sup>, P.I. Williams<sup>6,7</sup>,**  
7 **J.D. Allan<sup>6,7</sup>, S.C. Herndon<sup>8</sup>, L.R. Williams<sup>8</sup>, C. Mohr<sup>9</sup>, L. Xu<sup>10</sup>, N.L. Ng<sup>10,11</sup>, A.**  
8 **Detournay<sup>12</sup>, J.F. Barlow<sup>13</sup>, C.H. Halios<sup>13</sup>, Z.L. Fleming<sup>7,14</sup>, U. Baltensperger<sup>1</sup> and**  
9 **A.S.H. Prévôt<sup>1</sup>**

10 [1] {Laboratory of Atmospheric Chemistry, Paul Scherrer Institute, Villigen,  
11 Switzerland

12 [2] {Laboratory of Radiochemistry and Environmental Chemistry, Paul Scherrer  
13 Institute, Villigen, Switzerland

14 [3] {Swiss Light Source, Paul Scherrer Institute, Villigen, Switzerland

15 [4] {HASYLAB, DESY Photon Science, Hamburg, Germany

16 [5] {School of Biomedical Sciences, King's College London, London, UK

17 [6] {School of Earth, Atmospheric and Environmental Sciences, University of  
18 Manchester, Manchester, UK

19 [7] {National Centre for Atmospheric Science, University of Manchester, Manchester,  
20 UK

21 [8] {Aerodyne Research, Inc., Billerica, MA, USA

22 [9] {Department of Atmospheric Sciences, University of Washington, Seattle, WA,  
23 USA

24 [10] {School of Chemical and Biomolecular Engineering, Georgia Institute of  
25 Technology, Atlanta, GA, USA

26 [11] {School of Earth and Atmospheric Sciences, Georgia Institute of Technology,  
27 Atlanta, GA, USA

28 [12] {Centre for Ecology and Hydrology, Penicuik, Midlothian, Scotland

29 [13] {Department of Meteorology, University of Reading, Reading, UK

30 [14] {Department of Chemistry, University of Leicester, Leicester, UK



1 [\*] {now at: European XFEL, Hamburg, Germany}

2 Correspondence to: M. Furger (markus.furger@psi.ch)

3

#### 4 **Abstract**

5 Ambient concentrations of trace elements with 2 h time resolution were measured in  
6  $PM_{10-2.5}$ ,  $PM_{2.5-1.0}$  and  $PM_{1.0-0.3}$  size ranges at kerbside, urban background and rural  
7 sites in London during winter 2012. Samples were collected using rotating drum  
8 impactors (RDIs) and subsequently analysed with synchrotron radiation-induced X-  
9 ray fluorescence spectrometry (SR-XRF). Quantification of kerb and urban  
10 increments (defined as kerb-to-urban and urban-to-rural concentration ratios,  
11 respectively), and assessment of diurnal and weekly variability provided insight into  
12 sources governing urban air quality and the effects of urban micro-environments on  
13 human exposure. Traffic-related elements yielded the highest kerb increments, with  
14 values in the range of 10.4 to 16.6 for SW winds (3.3-6.9 for NE) observed for  
15 elements influenced by brake wear (e.g. Cu, Sb, Ba) and 5.7 to 8.2 for SW (2.6-3.0  
16 for NE) for other traffic-related processes (e.g. Cr, Fe, Zn). Kerb increments for these  
17 elements were highest in the  $PM_{10-2.5}$  mass fraction, roughly 2 times that of the  $PM_{1.0-}$   
18  $_{0.3}$  fraction. These elements also showed the highest urban increments (~ 3.0),  
19 although no difference was observed between brake wear and other traffic-related  
20 elements. All elements influenced by traffic exhibited higher concentrations during  
21 morning and evening rush hour, and on weekdays compared to weekends, with the  
22 strongest trends observed at the kerbside site, and additionally enhanced by winds  
23 coming directly from the road, consistent with street canyon effects. Elements related  
24 to mineral dust (e.g. Al, Si, Ca, Sr) showed significant influences from traffic-induced  
25 resuspension, as evidenced by moderate kerb (3.4-5.4 for SW, 1.7-2.3 for NE) and  
26 urban (~ 2) increments and increased concentrations during peak traffic flow.  
27 Elements related to regional transport showed no significant enhancement at kerb or  
28 urban sites, with the exception of  $PM_{10-2.5}$  sea salt (factor of up to 2), which may be  
29 influenced by traffic-induced resuspension of sea and/or road salt. Heavy duty  
30 vehicles appeared to have a larger effect than passenger vehicles on the  
31 concentrations of all elements influenced by resuspension (including sea salt) and  
32 wearing processes. Trace element concentrations in London were influenced by both  
33 local and regional sources, with coarse and intermediate fractions dominated by  
34 traffic-induced resuspension and wearing processes and fine particles influenced by  
35 regional transport.

1

## 2 **1 Introduction**

3 Ambient particulate matter (PM) has long been recognized to have a detrimental  
4 effect on public health in urban areas (e.g. Dockery and Pope, 1994). Of particular  
5 interest are particles with an aerodynamic diameter less than 10  $\mu\text{m}$  ( $\text{PM}_{10}$ ) as these  
6 particles can penetrate deeply into the lungs (Franklin et al., 2008; Zhou et al., 2011).  
7 Reche et al. (2012) reported even higher toxicity to human cells for the  $\text{PM}_{2.5-1.0}$  than  
8 for the  $\text{PM}_{10-2.5}$  fraction. Particle toxicity is known to vary significantly with PM  
9 composition and emission sources (Kelly and Fussell, 2012), with identified toxic  
10 constituents including soluble secondary inorganic particles, elemental and organic  
11 carbon, and especially metals. Effective mitigation strategies therefore require  
12 detailed, size-dependent characterization of particle composition and emission  
13 sources.

14 In addition to their direct effects on human health, metals and trace elements are of  
15 importance because their high source specificity and atmospheric stability make  
16 them effective tracers for source apportionment. In Europe, four main source types in  
17  $\text{PM}_{10}$  are commonly identified: vehicles (with tracers including e.g. Fe, Ba, Zn, Cu),  
18 crustal materials (e.g. Al, Si, Ca, Fe), sea salt (mainly Na, Cl, Mg) and mixed  
19 industrial/fuel-oil combustion (mainly V, Ni, S) and secondary aerosol (mainly S)  
20 (Putaud et al., 2010; Viana et al., 2008). The contribution of mineral dust and sea salt  
21 in most urban areas is larger in  $\text{PM}_{10}$  than in  $\text{PM}_{2.5}$  (Harrison et al., 2001; Weijers et  
22 al., 2011). Emissions from vehicle exhaust, industry and secondary aerosol are  
23 predominantly emitted and formed as  $\text{PM}_{1.0}$  or in  $\text{PM}_{2.5}$  (Bukowiecki et al., 2010;  
24 Harrison et al., 2011; Richard et al., 2011). Several of these sources have been  
25 directly linked to adverse health effects. For example, the largest aerosol source of  
26 human toxicity in Barcelona was attributed to traffic activities (encompassing vehicle  
27 emissions, road dust and secondary nitrate), with fuel oil combustion and industrial  
28 emissions also contributing to increased cancer risk (Reche et al., 2012). Turoczi et  
29 al. (2012) observed higher toxicity from direct emissions (e.g. from traffic) than from  
30 photochemically processed aerosol.

31 The Clean Air for London project (ClearLo; [www.clearflo.ac.uk](http://www.clearflo.ac.uk)) is a multinational  
32 effort to elucidate the processes driving poor air quality in London, implemented  
33 through comprehensive measurements of particle- and gas-phase composition, and  
34 meteorological parameters (Bohnenstengel et al., 2014). ClearLo builds upon recent  
35 modelling and monitoring studies in London (Arnold et al., 2004; Bohnenstengel et  
36 al., 2011; Bohnenstengel et al., 2013; Harrison et al., 2012a; Mavrogianni et al.,

1 2011). Despite improved air quality,  $PM_{10}$  concentrations are not decreasing,  
2 resulting in frequent exceedances of the daily  $PM_{10}$  limit (Harrison et al., 2008). Such  
3 exceedances are caused by complex interactions of regional and local emission  
4 sources, together with meteorological factors such as wind speed, air mass origin,  
5 and daily cycles of the atmospheric boundary layer (Charron and Harrison, 2005;  
6 Harrison and Jones, 2005; Jones et al., 2010). Currently, emissions by industrial  
7 sources and stationary combustion are modest, while traffic is thought to contribute  
8 up to 80 % of the total  $PM_{10}$  in London, compared to less than 20 % for the entire UK,  
9 according to emission inventories between 1970 and 2001 (Dore et al., 2003).

10 The spatial density of emission sources found in typical urban environments leads to  
11 elevated particle concentrations compared to nearby rural locations. As an example,  
12 buildings may influence local meteorology by restricting air circulation (street canyon  
13 effect), producing human exposures that are orders of magnitude higher than those  
14 predicted by regional dispersion models (Zhou and Levy, 2008). This provides both  
15 acute exposure risk and increased long-term exposure for those passing through  
16 regularly, thereby producing a non-negligible impact on public health. To assess the  
17 impact of such micro-environments, we here investigate London trace element  
18 concentrations in terms of increments, defined as the concentration ratios between  
19 an environment of interest and a reference site (e.g. Charron et al., 2007).

20 Only a few studies have investigated trace elements through simultaneous  
21 measurements at multiple sites. Harrison et al. (2012b) reported increments of  
22 kerbside to urban background sites in London for non-size segregated aerosol with a  
23 time resolution of 1 to 4 days. Theodosi et al. (2011) found that at urban and  
24 suburban sites in Athens and a regional site in Finokalia, Greece crustal elements  
25 dominate coarse particles ( $PM_{10-2.5}$ ), whereas anthropogenic sources such as fossil  
26 fuel combustion were confined to fine particles (V, Ni and Pb have > 70 % of their  
27 mass in  $PM_{1.0}$ ). Bukowiecki et al. (2009a) and Bukowiecki et al. (2010) examined  
28 trace elements in  $PM_{10-2.5}$ ,  $PM_{2.5-1.0}$  and  $PM_{1.0-0.1}$  aerosol at street canyon and urban  
29 background sites in Zürich, Switzerland, and showed increasing increments (note: 1  
30 means no increment) with particle size from about 1.2 (fine mode) to 2.4 (coarse  
31 mode) (averaged over all elements). All these studies report increments close to 1 for  
32 elements originating from regional sources such as sea salt and Saharan dust, while  
33 local, especially traffic-related sources yield increments around 2 for resuspension-  
34 related elements and between 3 and 5 for traffic-related elements. Additionally, the 1  
35 h time resolution used by Bukowiecki et al. (2009a) and Bukowiecki et al. (2010)  
36 enabled identification of enhanced increments for resuspension and wearing related  
37 elements like Si and Sb during peak traffic flows.

1 There is a need for more high time-resolved size segregated increment analyses to  
2 assess the exposure to trace elements from emission sources within urban areas  
3 under varying meteorological conditions. Here we present size segregated  
4 measurements of aerosol trace elements with 2 h time resolution performed  
5 simultaneously at kerbside and urban background sites in London, and a rural site  
6 outside London. We assess the effects of urban micro-environments on human  
7 exposure to particulate pollutants through the quantification of urban and kerb  
8 increments. These exposures are further investigated in terms of contributing  
9 emission sources, diurnal and weekly variability, local wind patterns, and regional  
10 transport effects.

11

## 12 **2 Methods**

### 13 **2.1 Measurement campaigns**

14 The ClearLo project was a measurement program in and around London lasting two  
15 years (2011-2012) and including two month-long Intensive Observation Periods  
16 (IOPs) in 2012 (Bohnenstengel et al., 2014). This paper focuses on the winter IOP  
17 lasting from 6 January to 11 February 2012. Measurements took place at three  
18 sampling sites located at or near permanent air quality measurement stations in the  
19 Automatic Urban and Rural Network (AURN): a kerbside site close to a very busy  
20 road, an urban background site in a residential area, and a rural background site  
21 away from direct emission sources (see Fig. 1).

22 The urban background sampling site was at the grounds of the Sion Manning  
23 Secondary School in North Kensington (NK, lat 51°31'21"N, lon 0°12'49"W). NK is  
24 situated within a highly trafficked suburban area of London (Bigi and Harrison, 2010;  
25 Harrison et al., 2012a). During the ClearLo IOPs this site served as the main  
26 measurement site and was upgraded with a full suite of particle- and gas-phase  
27 instruments, and instruments to measure meteorological parameters (Bohnenstengel  
28 et al., 2014). The kerbside site was located at Marylebone Road (MR, lat 51°31'21"N,  
29 lon 0°09'17"W) about 4.1 km to the east of NK (Charron and Harrison, 2005;  
30 Harrison et al., 2011). This site is located at the southern side of a street canyon, with  
31 an axis running approximately 260° to 80°. Measurements took place at 1 m from a  
32 busy six-lane road with a traffic flow of approximately 73 000 vehicles per day of  
33 which 15 % consist of heavy duty vehicles. Braking and stationary vehicle queues  
34 are frequent at the site due to a heavily used pedestrian light-controlled crossing (65  
35 m west of MR) and a signal-controlled junction (200 m west of MR). The rural site at

1 the Kent Showgrounds at Detling (DE, lat 51°18'07"N, lon 0°35'22"E) was  
2 approximately 45 km to the southeast of London downtown on a plateau at 200 m  
3 a.s.l. surrounded by fields and villages, and was close to the permanent  
4 measurement station of Kent and Medway Air Quality Monitoring Network. The site  
5 provides excellent opportunities to compare the urban and kerbside air pollution with  
6 the rural background pollution levels (Bohnenstengel et al., 2014; Mohr et al., 2013).  
7 A busy road with ~ 160 000 vehicles per day is located approximately 150 m south of  
8 DE. Meteorological parameters were measured at DE and at the British Telecom  
9 (BT) Tower (lat 51°31'17"N, lon 0°08'20"W), ~ 0.5 km east of MR (Harrison et al.,  
10 2012a).

11

## 12 **2.2 Instrumentation**

### 13 **2.2.1 RDI-SR-XRF**

#### 14 **Rotating drum impactors**

15 Rotating drum impactors (RDIs) were deployed at MR, NK and DE with a 2 h time  
16 resolution (see Table 1 for details). A detailed description of the RDI can be found in  
17 Bukowiecki et al. (2005), Bukowiecki et al. (2009c) and Richard et al. (2010). In short,  
18 aerosols are sampled through an inlet that removes all particles with aerodynamic  
19 diameter  $d > 10 \mu\text{m}$  at a flow rate of  $1 \text{ m}^3 \text{ h}^{-1}$ . The particles are size segregated in  
20 three size ranges based on  $d$  ( $\text{PM}_{10-2.5}$  (coarse),  $\text{PM}_{2.5-1.0}$  (intermediate) and  $\text{PM}_{1.0-0.3}$   
21 (fine)) by passing sequentially through three rectangular nozzles of decreasing size.  
22 Particle deposition occurs via impaction on  $6 \mu\text{m}$  thick polypropylene (PP) foils  
23 mounted on aluminium wheels and coated with Apiezon to minimize particle  
24 bouncing effects. After the last impaction stage a backup filter samples all remaining  
25 particles before the air passes through a pump. After each 2 h sampling interval the  
26 three wheels rotate stepwise to a blank section of the foil before a new sampling  
27 interval takes place. The small-size collection limit of the fine fraction was previously  
28 estimated at 100 nm (Bukowiecki et al., 2009c; Richard et al., 2010). However, new  
29 laboratory measurements of the RDI collection efficiency indicate an instrument-  
30 dependent (i.e. based on the machining of the specific nozzle) small-end cut point of  
31 approximately 290-410 nm (see Supplement A for details). This results in sampling of  
32 a smaller size range ( $\text{PM}_{1.0-0.3}$ ) than the  $\text{PM}_{1.0-0.1}$  range reported in previous studies,  
33 and influences the measured concentrations of elements with significant mass near  
34 this cut point (S, K and Pb).

1

## 2 **SR-XRF analysis**

3 Trace element analysis on the RDI samples was performed with synchrotron  
4 radiation-induced X-ray fluorescence spectrometry (SR-XRF) at the X05DA beamline  
5 (Flechsigt et al., 2009) at the Swiss Light Source (SLS) at Paul Scherrer Institute  
6 (PSI), Villigen PSI, Switzerland and at Beamline L at Hamburger  
7 Synchrotronstrahlungslabor (HASYLAB) at Deutsches Elektronen-Synchrotron  
8 (DESY), Hamburg, Germany (beamline dismantled November 2012). The samples  
9 with the deposited particles were placed directly into the X-ray beam. Irradiation of  
10 the samples took place at a 45° angle for 30 s. The light spot of the incoming beam  
11 was ~ 140 by 70 µm at SLS (monochromatic excitation at 10.5 keV, in vacuum) and  
12 ~ 80 by 150 µm at HASYLAB (polychromatic excitation, in air). Fluorescence light  
13 produced by the elements in the samples was detected by energy-dispersive  
14 detectors (silicon drift detector at SLS, nitrogen cooled Si(Li)-detector at HASYLAB)  
15 at a 90° angle relative to the incoming beam. At SLS K $\alpha$  lines of the elements with  
16 atomic number  $Z = 11-30$  (Na-Zn) were measured, and at HASYLAB K $\alpha$  lines of the  
17 elements with  $Z = 22-56$  (Ti-Ba) and L $\alpha$  lines of  $Z = 82$  (Pb).

18 The fluorescence counts per element were calibrated to the element mass  
19 concentration using multi-element standards, where each standard consisted of a set  
20 of preselected elements in 5 different concentrations ranging between 0.05 and 0.4  
21 µg cm<sup>-2</sup>. The absolute element concentrations in these standards were determined  
22 with inductively coupled plasma-optical emission spectroscopy (ICP-OES). The  
23 absolute calibration factor for the SR-XRF system was referenced to Fe and  
24 determined from the linear relation between the SR-XRF response and the ICP-OES  
25 measurements. Because the fluorescence yield increases with atomic number  $Z$ , a  
26 relative calibration curve was constructed as follows: for each element present in the  
27 standards and having a detectable K $\alpha_1$  line, an absolute calibration factor was  
28 determined as for Fe, and a dimensionless relative response factor was calculated as  
29 the ratio of this absolute factor to that of Fe. These relative response factors were  
30 plotted as a function of line energy and a polynomial curve was fit to obtain response  
31 factors by interpolation for elements not present in the standard. In total 25 elements  
32 were quantified (Na, Mg, Al, Si, P, S, Cl, K, Ca, Ti, V, Cr, Mn, Fe, Ni, Cu, Zn, Br, Sr,  
33 Zr, Mo, Sn, Sb, Ba, Pb). Details of the methodology can be found elsewhere  
34 (Bukowiecki et al., 2005; Bukowiecki et al., 2008; Richard et al., 2010), with the  
35 following significant changes (see Supplement B for further details):

1 1. At SLS, we used an e2v SiriusSD detector (SiriusSD-30133LE-IS) and in-house  
2 built vacuum chamber to extend the measured range of elements down to Na and  
3 Mg.

4 2. Reference standards for calibration of element fluorescence counts to mass  
5 concentrations were produced on the same 6  $\mu\text{m}$  PP substrate as used for RDI  
6 sampling allowing the use of identical geometry and irradiation time for RDI samples  
7 and reference standards, thereby reducing uncertainties in absolute and relative  
8 calibrations.

9 3. Data were processed with the Spectral Analysis for Multiple Instruments – toolkit  
10 for XRF (SAMI-XRF) developed in-house within the IGOR Pro software environment  
11 (Wavemetrics, Inc., Portland, OR, USA). SAMI handles spectral fitting, quantification  
12 of associated uncertainties, and calculation and application of calibration parameters.

13 XRF is sensitive to self-attenuation of fluorescence radiation in the sample and  
14 depends on the sample composition and density, as well as particle layer thickness  
15 or particle size. The PM sample thickness of the coarse and intermediate fractions  
16 was maximally 0.7-1.5  $\mu\text{m}$  at a maximum concentration of 10  $\mu\text{g m}^{-3}$  total PM mass  
17 for each sample. For these fractions, self-absorption therefore mainly occurs within  
18 the individual particles (geometric mean of 5 and 1.6  $\mu\text{m}$  for  $\text{PM}_{10-2.5}$  and  $\text{PM}_{2.5-1.0}$   
19 fractions, respectively). For the fine fraction the PM layer is several micrometres  
20 thick, resulting in absorption inside the PM layer. However, most mass of the lightest  
21 elements (Na-Si) is restricted to the coarse and intermediate fraction. We therefore  
22 neglect self-absorption effects in the fine fraction samples. The calculated layer  
23 thickness of the dried calibration solution on the calibration standards is negligible at  
24 3-60 nm, but the particle size of the dried droplets shows a geometric mean volume  
25 size distribution of  $9 \pm 5 \mu\text{m}$  and is therefore relevant for self-attenuation. Attenuation  
26 factors (AF) were calculated for the calibration standards as well as for the coarse  
27 and intermediate fraction samples for Na, Mg, Al and Si, as a function of density,  
28 mass attenuation coefficient and particle size, according to a simple attenuation  
29 model (Table 2; Formenti et al., 2010). The AF of heavier elements were negligible  
30 within the measurement uncertainties. The attenuation of the calibration standards is  
31 taken into account for all samples, and additional corrections are applied to the  
32 coarse and intermediate samples. Calzolari et al. (2010) found comparable self-  
33 absorption effects for samples of different composition, total loading and sampling  
34 site. Because the elemental composition and particle size distribution of each sample  
35 are unknown, we assume a uniform correction for each element within a given size  
36 fraction. The overall AF are 0.22-0.52, 0.32-0.55, 0.43-0.61 and 0.51-0.64 for Na,

1 | Mg, Al and Si, respectively (calculated as correction factor of calibration  
2 | standard/sample).

### 4 | **2.2.2 Other measurements**

5 Here a short description is given of relevant particle- and gas-phase instruments  
6 deployed at MR, NK and DE during the winter IOP. Daily PM<sub>10</sub> filter samples  
7 (midnight to midnight) were collected at MR and NK using Partisol 2025 samplers  
8 (Thermo Scientific, Inc.). The filters were digested in a 1:2 mixture of perchloric and  
9 hydrofluoric acid, and subsequently analysed by ICP-mass spectrometry (ICP-MS,  
10 calibration with NIST standards) for the determination of Na, Al, Ca, Ti, V, Mn, Fe, Ni,  
11 Cu, Zn, Sr, Mo, Sb, Ba and Pb. Additionally, Mg, K and Sn were available at NK.  
12 High-resolution time-of-flight aerosol mass spectrometers (HR-ToF-AMS, Aerodyne  
13 Research, Inc., Billerica, MA, USA) were deployed at MR (5 min time resolution), NK  
14 (5 min resolution every 30 min), and DE (2 min resolution) to characterise the non-  
15 refractory submicron aerosol components (DeCarlo et al., 2006). PM<sub>10</sub> mass  
16 concentrations were measured at all three sites with FDMS-TEOM (Filter Dynamics  
17 Measurement System Tapered Element Oscillating Microbalances; Thermo  
18 Scientific, Inc.) with a 1 h time resolution. NO<sub>x</sub> measurements at MR and NK were  
19 performed with a NO<sub>x</sub> chemiluminescent analyser with a single chamber and a single  
20 detector (API, A Series, model M200A; 15 min resolution). At DE NO was determined  
21 with a Thermo Scientific 42i analyser and NO<sub>2</sub> with an Aerodyne CAPS-NO<sub>2</sub> (SN  
22 1002) and an Aerodyne QCL-76-D. These NO and NO<sub>2</sub> measurements were  
23 summed together to obtain NO<sub>x</sub> (1 min resolution). Black carbon (BC) was measured  
24 with a 2-wavelength Aethalometer ( $\lambda = 370$  and 880 nm, model AE22, Magee  
25 Scientific) at MR and a 7-wavelength Aethalometer ( $\lambda = 370-950$  nm, model AE31,  
26 Magee Scientific) at NK and DE (5 min resolution), with a 2.5  $\mu\text{m}$  cyclone at MR and  
27 DE and a 3.5  $\mu\text{m}$  cyclone at NK. Traffic counts by vehicle group at MR from road  
28 sensors (number of vehicles per 15 min) were available as well. Wind direction and  
29 wind speed data for MR and NK were taken from the BT Tower (30 min resolution)  
30 where anemometers were placed to the top of an open lattice scaffolding tower of 18  
31 m height on top of the main structure (190.8 m a.g.l.; Wood et al., 2010), whereas  
32 local data were used at DE (1 min resolution). Air mass origins were analysed with  
33 back trajectory simulations using the UK Met Office's Numerical Atmospheric  
34 Modelling Environment (NAME) dispersion model (Jones et al., 2007).

35



### 3 Data intercomparison and uncertainty

Here we compare RDI-SR-XRF data with independent filter data (24 h PM<sub>10</sub> trace element data analysed with ICP-MS; roughly 9 % uncertainty at a 95 % confidence interval) for 18 elements collected at MR and NK (no filter data was available at DE). For this comparison, the three size ranges of the RDI were summed up to total PM<sub>10</sub> and averaged to the filter collection period. Details of the intercomparison results can be found in Supplement C. In short, the majority of the elements (Al, Ca, Ti, Mn, Fe, Cu, Zn, Sr, Sb, Ba) agree within approximately  $\pm 50$  % with Pearson's  $R > 0.78$ . Na and Mg agree as well, but have higher uncertainties due to self-absorption corrections. Fit coefficients deviate more from the other elements, disagreement can be attributed due to low or unknown filter sample extraction efficiencies (V, Ni, Mo), uncertainties in the XRF relative calibration (Na, Mg) and differences in the particle size range sampled by the two measurement techniques (K, V, Sn, Pb). Thus, for the measured size range, the intercomparison calls into question only the absolute magnitudes of Na and Mg concentrations determined by the XRF. However, all these elements are retained in the ensuing analysis as (1) they are well correlated with the filters (Pearson's  $R > 0.89$ ); (2) they yield internally consistent results (e.g. appropriate ratio for sea salt), as described in the following sections; (23) the ensuing analysis relies on relative changes/ratios per element across sites and is therefore not affected by a systematic bias in absolute magnitude.

The agreement between XRF and filter measurements in the present study compares favourably with that obtained in previous intercomparisons of trace element measurement techniques. Comparison of RDI-SR-XRF with daily element concentrations from a high volume sampler followed by subsequent analysis using laboratory-based wavelength dispersive XRF (Bukowiecki et al., 2005) and by ICP-OES and ICP-MS (Richard et al., 2010) yielded slopes between 0.7 and 1.6 (except for S and K) with Pearson's  $R > 0.5$ . The spread/biases in these intercomparisons are not necessarily due to SR-XRF issues, as can be seen from a comparison by Salcedo et al. (2012) of ICP with proton-induced X-ray emission (PIXE) and AMS trace element measurements. Agreement between ICP and PIXE data was in the same range as between either method and the AMS data, with slopes ranging between 0.06 and 0.93 with Pearson's  $R$  from about 0.3 to 0.7.

Estimated uncertainties (per size fraction) and detection limits for each measured element are given in Supplement Table S3. A brief overview is presented here:

1 1. RDI sampling: the fluctuations in the flow rate are negligible within 5 % (Richard et  
2 al., 2010) and the uncertainties in the size cut off are discussed in Supplement A.

3 2. SR-XRF accuracy: uncertainties in the absolute and relative calibrations affect  
4 absolute/fractional concentrations, but cancel out for relative changes/ratios, because  
5 all samples were measured under the same calibration conditions.

6 3. Issues such as imperfect flatness of the sample foils and detector dead time  
7 corrections (Richard et al., 2010) reduce measurement precision but affect all  
8 elements with the same scaling factor.

9 4. SR-XRF measurement precision is affected by sample inhomogeneity, ~~and~~  
10 spectral analysis and self-absorption correction uncertainties. Sample inhomogeneity  
11 was assessed by Bukowiecki et al. (2009c) and found to contribute  $\pm 20$  %  
12 uncertainty.

13 For most elements, except Mn and the lightest elements, sample inhomogeneity is  
14 the largest source of uncertainty. Mn is affected by spectral analysis uncertainties  
15 due to peak overlap with Fe, which is present in much higher concentrations.  
16 Therefore, a small bias change in the energy calibration as function of detector  
17 channel leads to a large change in the peak area of Mn. Self-absorption effects are a  
18 significant source of uncertainty for the lightest elements (Na-Si), but the good  
19 comparisons to the filter data suggest that the corrections lead to reasonable results.

20 All data points lie well above their element detection limits, resulting in negligible  
21 uncertainties from the signal strength. In addition, RDI-SR-XRF measurements (both  
22 absolute/fractional and relative/ratio) are affected by atmospheric variability. This  
23 variability is likely the predominant source of the data spread evident in Table 3 and  
24 the following analyses.

## 25 26 **4 Results and discussion**

### 27 **4.1 Trace element concentrations**

28 During the ClearfLo winter IOP total mass concentrations of the analysed trace  
29 elements ranged from less than  $0.1 \mu\text{g m}^{-3}$  to  $\sim 2013 \mu\text{g m}^{-3}$ . Typically,  
30 concentrations were highest at MR and lower at NK and DE, and decreased with  
31 particle size. An overview of the obtained trace element concentrations as a function  
32 of size and site is given in Table 3. Note that S is not a trace element, but is  
33 commonly reported in trace element studies and is a good tracer for regional

1 transport. Among the analysed trace elements, highest concentrations at MR were  
2 found for Cl (28 %), Na (27 %) and Fe (21 %). At NK this was the case for Cl (33 %),  
3 Na (22 %) and Fe (11 %) and at DE Cl (30 %), Na (25 %) and S (20 %)~~Na (37 %), Cl~~  
4 ~~(19 %) and Fe (17 %)~~. At NK this was the case for ~~Na (47 %), Cl (19 %) and Fe (7 %)~~  
5 ~~and at DE Na (49 %), S (11 %) and Mg (7 %)~~. Total analysed mass measured by the  
6 RDI-SR-XRF (trace elements + S) contributed on average 2416 % to the total PM<sub>10</sub>  
7 mass (from FDMS-TEOM) of 32 (5-74) µg m<sup>-3</sup> at MR (not extrapolated to the  
8 corresponding oxides), 4712 % to the mass of 23 (1.4-63) µg m<sup>-3</sup> at NK and 4410 %  
9 to the mass of 17 (0.5-58) µg m<sup>-3</sup> at DE.

10 A comparison between the contributions of coarse, intermediate and fine fractions to  
11 the total PM<sub>10</sub> mass of each trace element is shown in Fig. 2 for the three sites. Trace  
12 elements at MR are dominated by the coarse fraction. Analysis in the following  
13 sections and previous measurements at this site (Charron and Harrison, 2005)  
14 suggest this is caused by large contributions of resuspension and traffic-related  
15 mechanical abrasion processes, which primarily contribute to the coarse fraction. For  
16 all elements at this site, except S, Br and Pb, the coarse fraction contributes more  
17 than 50 %. Mass fractions of intermediate mode elements to total PM<sub>10</sub> are rather  
18 constant with contributions ranging from 13 to 27 %. The fine fraction contributes up  
19 to 50 % of total mass for S, K, Zn, Br and Pb; for other elements fine contributions  
20 are less than 20 %. S, K, Zn, Br and Pb are typically dominated by the fine fraction  
21 with known sources including heavy oil combustion (S, K, Zn; Lucarelli et al., 2000),  
22 traffic exhaust (Br, Pb; Formenti et al., 1996), industrial processes (Zn, Pb; Moffet et  
23 al., 2008), and secondary sulphate and wood combustion (S, K, Pb; Richard et al.,  
24 2011).

25 For most elements, particle mass contributions of the smaller size fractions are more  
26 important as one moves from kerbside to urban background to rural sites (Fig. 2).  
27 The relatively large fine fraction contribution at DE is probably caused by the  
28 absence of local traffic which results in lower contributions of resuspension and  
29 traffic-related processes to total element concentrations. A different behaviour is  
30 observed for Cr, Ni and Mo with on average 80 % of their mass at DE in the coarse  
31 fraction, compared to 73 % at MR and 60 % at NK. The time series of these coarse  
32 mode species are very spiky, are slightly enhanced with SW winds, but are not  
33 collocated with measurements of BC and AMS species, suggesting emissions from a  
34 local industrial source, potentially from stainless steel production (Querol et al., 2007;  
35 Witt et al., 2010) near DE rather than regional transport.

1 Comparing the contributions of groups of elements to total trace element  
2 concentrations at the sites provides an overview of local and regional sources  
3 affecting London; a detailed source apportionment study will be the subject of a  
4 future manuscript. Na, Mg and Cl are typical sea salt elements and contribute around  
5 65.8 % to the total PM<sub>10</sub> trace element mass at all three sites, indicating that the air  
6 pollutant levels caused by elements are dominated by natural emission sources  
7 being transported to London. Mineral dust elements (Al, Si, Ca, Ti) mainly brought  
8 into the air via resuspension contribute on average 44.2 % at MR, NK and DE. For  
9 some specific brake wear elements (Cu, Sb, Ba) these contributions are 4.1.5,  
10 0.40.7 and 0.30.4 % at MR, NK and DE, respectively. Although these metals  
11 contribute a small fraction of total PM<sub>10</sub> mass concentrations, they induce adverse  
12 health effects. Xiao et al. (2013) e.g. found that Zn, Fe, Pb and Mn were the major  
13 elements responsible for plasmid DNA damage, whereas Kelly and Fussell (2012)  
14 found that increases in PM<sub>10</sub> as a result of increased Ni, V, Zn and Cu contributions  
15 showed highest mortality risks, as opposed to increased Al and Si.

## 17 **4.2 Urban and kerb increment**

### 18 **4.2.1 Urban increment**

19 The urban increment compares the trace element concentrations at the urban  
20 background site to the concentrations at the rural site, and is calculated here as the  
21 ratio of concentrations at NK to DE. Figure 3 shows the mean, median and 25-75th  
22 percentile urban increment ratios for the coarse, intermediate and fine fractions per  
23 element. Most elements, except Ni and coarse mode Cr are enriched at the urban  
24 background site by factors between 1.0 and 6.5 (median ratios). Increments  
25 decrease towards smaller sizes. Ni and coarse mode Cr show higher concentrations  
26 at DE relative to NK, as does the mean value of coarse Mo. Especially at DE Cr and  
27 Ni show strong correlations with Pearson's *R* of 0.85. As discussed in the previous  
28 section, enhanced coarse mode Cr, Ni and Mo may indicate an industrial source near  
29 the rural site.

30 Coarse mode Zr exhibits low concentrations at DE, where the median value actually  
31 falls below detection limit, though discrete events above detection limit also exist. For  
32 this reason, the median-based urban increment is not plotted, while the mean ratio is  
33 driven by several large concentration peaks at NK, resulting in a large mean ratio of  
34 21. In the case of Cl, a large spread in the urban increment values is seen for all

1 three size ranges. Cl is likely depleted relative to other sea salt elements like Na and  
2 Mg (throughout the campaign Cl concentrations fall to 0, whereas Na and Mg  
3 concentrations remain positive) due to replacement by nitrate, and the extent of such  
4 depletion is greater in small particles (Nolte et al., 2008). At DE, Cl depletion seems  
5 apparent at all size ranges, whereas at MR depletion mainly takes place in the PM<sub>1.0-0.3</sub>  
6 fraction. NK shows Cl depletion especially in the PM<sub>1.0-0.3</sub> fraction, but to some  
7 extent also in intermediate mode particles.

8 For ease of discussion, we empirically group elements based on similar urban  
9 increment values. Mn, Fe, Cu, Zn, Zr, Mo, Sn, Sb and Ba show urban increments on  
10 average of 3.5 in the coarse, 3.1 in the intermediate and 2.0 in the fine fraction (Fig.  
11 3). These have been identified as traffic-related elements by e.g. Amato et al. (2011);  
12 Bukowiecki et al. (2010); Minguillón et al. (2014); Richard et al. (2011) and Viana et  
13 al. (2008). Zr has also been linked to mineral dust (Moreno et al., 2013). We can  
14 understand that from analysing the Enrichment Factors of these elements (EF). EF is  
15 a measure of the enrichment of elements relative to the upper continental crust  
16 (UCC) and is defined as ppm metal in the sample / ppm metal in UCC with Si as  
17 reference material (UCC from Wedepohl, 1995). Zr is the only element in this traffic  
18 group that is depleted in the atmosphere relative to their UCC concentrations, but  
19 with concentrations at NK higher than at DE. Most other elements clearly indicate  
20 anthropogenic origin with EF > 10. Dependent on the method, Zr can be either  
21 grouped with traffic-related elements or with dust elements. The urban increments  
22 are similar to that of NO<sub>x</sub>, where concentrations at NK were on average a factor 4.9  
23 higher than at DE (the mean concentration at NK was 68 ppb, at DE 14 ppb). Black  
24 carbon (BC), a marker for both traffic and wood burning emissions, had an urban  
25 increment of only 1.1 (concentration at NK 757 ng m<sup>-3</sup>, at DE 633 ng m<sup>-3</sup>), likely due  
26 to local wood burning emissions around DE (Mohr et al., 2013). Al, Si, Ca, Ti and Sr  
27 as markers for mineral dust (e.g. Amato et al., 2009; Lin et al., 2005; Lucarelli et al.,  
28 2000) show a factor 2.0 higher concentrations at NK relative to DE in the coarse, 1.9  
29 in the intermediate and 1.6 in the fine fraction (EF < 10). These results indicate that  
30 moving from rural to urban backgrounds yields a larger relative increase in traffic  
31 than in mineral dust elements. Surprisingly, sea salt elements (Na, Mg, Cl) show  
32 higher concentrations at NK than at DE of up to a factor of 2 for the coarse mode,  
33 despite the expected dominance of regional over local sources. This highlights the  
34 potential importance of sea or road salt resuspension by traffic. Similar urban  
35 increment values for traffic-related, resuspension and sea salt elements have been  
36 observed by Lee et al. (1994) for particles below a few µm. Theodosi et al. (2011)

1 also found higher increments ( $> 2$ ) for trace elements in  $PM_{10}$  aerosol from local  
2 anthropogenic sources like fossil fuel combustion (V, Ni, Cd) and traffic (Cu), relative  
3 to long-range transported Saharan dust (Fe, Mn) with increments close to 1.  
4 However, our study suggests that the non-size-resolved increment values reported in  
5 the cited studies do not fully capture the urban/rural differences.

6 The influence of regional transport by anthropogenically produced elements (Fig. 3)  
7 is seen by the low urban increments between 1.1 and 1.8 for P, S, K, Zn, Br, Sn and  
8 Pb in  $PM_{1.0-0.3}$  (EF  $> 25$ ) and of 1.6 for total  $PM_{10}$  mass (concentration at NK  $23 \mu\text{g m}^{-3}$ ,  
9 at DE  $17 \mu\text{g m}^{-3}$ ). The concentrations of the main components in  $PM_{10}$  (sulphate,  
10 nitrate and secondary organic compounds) within an urban area are mostly  
11 influenced by regional transport, as found in London during the REPARTEE project  
12 (Harrison et al., 2012a) and in Paris during the MEGAPOLI project (Crippa et al.,  
13 2013; Freutel et al., 2013), resulting in low increments for total  $PM_{10}$  mass. Similar  
14 urban increment values (1.3 to 1.8) for 1 and 24 h total  $PM_{2.5}$  mass concentrations  
15 were reported across many sites in the UK (Harrison et al., 2012c).

16

17 **4.2.2 Kerb increment**

18 While the urban increment investigates the effect of diffuse emission sources on  
19 particle concentrations, the kerb increment investigates an urban micro-environment,  
20 specifically the local effects of roadside emissions and activities. Here, the kerb  
21 increment is calculated as the ratio of concentrations at MR to NK. However,  
22 observed concentrations at MR strongly depend on wind direction, because the road  
23 runs from approximately  $260^\circ$  to  $80^\circ$  and the street canyon with the surrounding  
24 buildings and intersections creates a complex wind circulation system (Balogun et al.,  
25 2010). Since the measurement station is located at the southern side of the canyon,  
26 measurements during time periods with winds from the south are influenced by on-  
27 road emissions on top of the urban background pollution. Higher concentrations were  
28 observed with SSE winds, i.e. perpendicular to the direction of the road by e.g.  
29 Balogun et al. (2010), Charron and Harrison (2005) and Harrison et al. (2012b).

30 In this study, the RDI-SR-XRF data was split into four equally spaced wind direction  
31 sectors based on wind direction data; N ( $315 - 45^\circ$ ), E ( $45 - 135^\circ$ ), S ( $135 - 225^\circ$ ) and  
32 W ( $225 - 315^\circ$ ). Figure 4 shows size-resolved trace element concentrations per wind  
33 sector normalized to the global median concentration for each element at MR. As  
34 expected, winds from the south yield the highest concentrations, whereas northern  
35 winds yield the lowest, independent of size fraction. West and east winds are parallel

1 to the street canyon and yield intermediate concentrations. Similar behaviour is  
2 observed for NO<sub>x</sub>, and no directional biases for high wind speeds are observed  
3 (Supplement Fig. S6).

4 Traffic-related and some other anthropogenically-related elements (V, Cr, Mn, Fe, Ni,  
5 Cu, Zn, Zr, Mo, Sn, Sb, Ba) show the strongest wind direction dependency with up to  
6 a factor of 2-3 higher concentrations during S relative to N winds for the three size  
7 fractions (Fig. 4). A factor of 1.5-2 is obtained for resuspended dust elements.  
8 Harrison et al. (2012b) found a ratio of 2 for Fe (as tracer for brake wear) and 1.2 for  
9 Al (as tracer for mineral dust) for SW versus NE winds for particles between 2 and 3  
10 µm. However, they were limited by their time resolution of several days, resulting in  
11 potentially substantial wind direction variations during each measurement, which  
12 would blur the different conditions and yield reduced ratios.

13 Other elements show only minor correlations with wind direction (Fig. 4), indicating  
14 more influence from regional transport, instead of being locally affected by traffic.  
15 Only fine mode S, K and Br seem to be enriched with winds from the east, potentially  
16 related to long-range transport from the European continent.

17 Local wind direction has a greatly reduced effect at urban background and rural sites.  
18 At NK, the element concentrations are only subject to high concentration outliers for  
19 E winds (Supplement Fig. S4), potentially caused by the transport of pollutants from  
20 downtown London, or by lower wind speeds occurring with E winds resulting in  
21 reduced dilution and increased concentrations of traffic pollutants (e.g. NO<sub>x</sub>)  
22 throughout the city (Supplement Fig. S6). The rural site hardly shows wind direction  
23 dependent concentrations (Supplement Fig. S5-6). Interpretation of data from the E  
24 sector is unclear due to the low number of data points (45 out of 318 data points).  
25 Only data from the N sector show enhanced concentrations for several elements  
26 correlating with higher wind speeds and back trajectories consistent with transport  
27 from continental Europe.

28 To simplify reporting of the kerb increment and facilitate comparison with previous  
29 studies (e.g. Harrison et al., 2012b), we combined the south/west sectors and the  
30 north/east sectors into SW (135-315°) and NE (315-135°) sectors. To eliminate  
31 meteorological and/or regional transport effects, this segregation is performed at both  
32 MR and NK. The kerb increment is then calculated as the ratio of MR to NK and  
33 shown in Fig. 5 (Supplement Fig. S7 shows the increments for the 4 individual  
34 sectors). As with the urban increment, we focus on the ratio of the medians at MR  
35 and NK to reduce the effects of outliers. Two features become directly visible; the

1 kerb increment is much higher for coarse than for intermediate and fine particles, and  
2 kerb increments are much higher for SW than for NE wind conditions. With the latter,  
3 kerb increments are on average 2.7, 1.6 and 1.7 for coarse, intermediate and fine  
4 mode particles, respectively. This significant enhancement is likely due to  
5 recirculation of particles within the street canyon following their resuspension and/or  
6 emission by traffic. However, these increments are much smaller than those  
7 observed in the SW sector, where enhancements relative to NK of 6.7, 3.3 and 3.1  
8 (coarse, intermediate, fine) are observed. These results indicate the existence of  
9 micro-environments within the street canyon dependent on wind direction.

10 As in the previous discussion, we again group elements by kerb increment (Fig. 5).  
11 The first group consists of Cu, Zr, Mo, Sn, Sb and Ba and yields the highest  
12 increments in the coarse mode ranging from 10.4 to 16.6 in the SW sector (3.3-6.9  
13 for NE). These elements are typically associated with brake wear (e.g. Bukowiecki et  
14 al., 2009b; Harrison et al., 2012b), and are much higher than the increments of 4.1 to  
15 4.4 reported by Harrison et al. (2012b) at the same sites for particles < 21  $\mu\text{m}$ . They  
16 assigned Fe, Cu, Sb and Ba to brake wear, but in the current study Fe has a  
17 significantly lower kerb increment than other brake wear tracers, suggesting a  
18 significant alternative source. When combining all size fractions and ignoring wind  
19 direction influences, increments in this study are about 4.9, and more similar to  
20 previous studies. The discrepancies between the kerb increments obtained using  
21 these two calculation strategies highlights the difficulties in characterizing human  
22 exposure to locally generated pollutants in urban environments, as the detailed  
23 topography and microscale meteorology greatly alter particle concentrations, and the  
24 effects are size-dependent. Amato et al. (2011) calculated road side increments in  
25 Barcelona for trace elements in  $\text{PM}_{10}$  with a 1 h time resolution and found increments  
26 for brake wear elements of only 1.7 (based on Fe, Cu, Sb, Cr, Sn ). These low  
27 increments are probably due to the reduced dispersion in Barcelona caused by a  
28 complex topography, resulting in high urban background levels.

29 The second group consists of V, Cr, Mn, Fe, Ni, Zn and Pb with increments of 5.7-8.2  
30 ( $\text{PM}_{10-2.5}$ ) in the SW sector (2.6-3.0 for NE) (Fig. 5). V and Ni are typically assigned to  
31 industrial sources and heavy-oil combustion (e.g. Mazzei et al., 2007; Viana et al.,  
32 2008), Zn is usually associated with tire wear (e.g. Harrison et al., 2012b; Lin et al.,  
33 2005), and the other elements are commonly associated with traffic-related  
34 emissions (e.g. Amato et al., 2013; Bukowiecki et al., 2009a; Richard et al., 2011).

35 | We label this group as anthropogenically-influenced (ANTH). The EF of V, Cr and Ni



1 | are much lower than those of the other elements in this group (24 vs. > 10),  
2 | indicating at least to some extent different source origins. These kerb increments are  
3 | similar to the ones for NO<sub>x</sub> of 8.5 for SW and 2.4 for NE, confirming the  
4 | anthropogenic influence (traffic and other sources) on these elements. The high  
5 | braking frequency at MR due to congested traffic probably resulted in increased kerb  
6 | increments of brake wear relative to ANTH elements that are also influenced by local  
7 | traffic and other sources around NK. Increments of these ANTH elements are higher  
8 | than previously reported values of 1.8-4.5 for studies with low time resolution and  
9 | non-size segregated particles (Boogaard et al., 2011; Janssen et al., 1997). The high  
10 | increments presented here might be caused by street canyon effects, trapping  
11 | pollutants emitted at street level and preventing dilution to the urban background.  
12 | The enhanced kerb increments for brake wear relative to ANTH elements are  
13 | apparent in all three size fractions, although increments become more similar  
14 | towards smaller sizes with a factor 1.7 between both element groups in the coarse,  
15 | 1.5 in the intermediate and 1.4 in the fine mode. Both groups show the additional  
16 | information gained with size-segregated aerosol, where exposure to trace elements  
17 | in the street canyon relative to the urban background increases with particle size,  
18 | either caused by increased traffic-related emissions with particle size or by more  
19 | efficient transport of submicron particles from street sites to the urban background.  
20 | Furthermore, the highly time-resolved element measurements presented here  
21 | enabled us to resolve the systematic, wind direction dependent variability in kerb  
22 | increments.

23 | The third group is associated with mineral dust (Al, Si, Ca, Ti, Sr) with coarse mode  
24 | increments of 3.4-5.4 for SW winds (1.7-2.3 for NE) (Fig. 5). These elements are  
25 | brought into the air both by traffic-induced resuspension and transport from other  
26 | locations. This second process increases both urban background and kerbside  
27 | concentrations, and thus reduces kerb increments relative to direct traffic-related  
28 | elements. Lower kerb increments for mineral dust than traffic-related elements are  
29 | generally observed in increment studies (Amato et al., 2011; Boogaard et al., 2011;  
30 | Bukowiecki et al., 2009b; Harrison et al., 2012b), although the dust increments found  
31 | in this study are larger than most reported increments (typically 1-2). As in the traffic-  
32 | related groups, increments increase with particle size, indicating enhanced human  
33 | exposure at the street side of particles above 1 µm.

34 | Na, Mg and Cl (sea salt) form the fourth group and yield kerb increments of 1.0 to  
35 | 2.7, independent of size fraction but with slightly enhanced ratios with SW compared  
36 | to NE winds (Fig. 5). Similar increments were observed for total PM<sub>10</sub> mass. As

1 discussed for urban increments, even though these elements have regional sources,  
2 they are influenced by resuspension processes within the urban area which are  
3 enhanced at kerbside sites.

4 The remaining elements (P, S, K, Br) can be grouped together. In the coarse mode,  
5 these elements yield increments similar to the mineral dust group, indicating that this  
6 group is influenced by resuspension processes in the street canyon (Fig. 5).  
7 However, especially in the fine mode increments around 1 were found, consistent  
8 with regional transport dominating over local emission sources.

9

### 10 **4.3 Temporal trends in trace element concentrations**

11 In contrast to traditional trace element measurements, the RDI-SR-XRF enables  
12 measurement of element concentrations with high time resolution (2 h in this work).  
13 This enables investigation of diurnal cycles, which are useful both for source  
14 discrimination and in determining the processes contributing to elevated PM levels.  
15 We also discuss weekly cycles, which can be useful in distinguishing emissions from  
16 heavy duty and passenger vehicles (HDV and LDV); HDV numbers typically diminish  
17 during the weekend. Back trajectory analysis aids source discrimination by  
18 understanding regional transport influences by different air mass origin. Here we  
19 discuss the temporal trends of trace elements in five groups based on expected  
20 sources and the increment analyses in Sect. 4.2, in order of increasing local  
21 influence: regional background, sea salt, mineral dust, traffic-related and brake wear.

22 Figures 6 and 7 show size-segregated median diurnal and weekly cycles,  
23 respectively, for 5 elements representative of the classes mentioned above: Na (sea  
24 salt), Si (mineral dust), S (regional background), Fe (traffic-related) and Sb (brake  
25 wear) at the three sites. Because of the wind direction effect evident at MR, diurnal  
26 cycles at all three sites are shown for SW and NE winds. Wind direction analyses are  
27 not incorporated into the weekly cycles because the month-long campaign provided  
28 insufficient data points for meaningful division. This also means that weekly cycles  
29 are subject to influences by mesoscale events. For example, sea salt shows no clear  
30 weekly cycle, except for a peak on Fridays in intermediate and fine fractions  
31 coinciding with westerly winds, which coincidentally occurred more frequently on  
32 Fridays than on other days. Except for such events, regionally dominated elements  
33 tend to display flat, featureless diurnal/weekly cycles, while elements dominated by  
34 recurring local processes (e.g. traffic patterns) show interpretable features. Diurnal

1 and weekly cycles of all other elements can be found in Supplement Fig. S8-9. For  
2 comparison, diurnal and weekly cycles of NO<sub>x</sub> and total PM<sub>10</sub> mass at all sites, and of  
3 traffic flow at MR are shown in Fig. 8. The time series of these species were  
4 averaged to the RDI collection times before obtaining the cycles. BC diurnal and  
5 weekly cycles (not shown) are very similar to those of NO<sub>x</sub>.

6

7 **4.3.1 Regional influences**

8 Elements dominated by regional sources (P, S, K, Br) occur mainly in the fine fraction  
9 and are similar to total PM<sub>10</sub> mass in showing no obvious diurnal and weekly  
10 patterns. This interpretation is consistent with the urban/kerb increment analysis  
11 discussed in Sect. 4.2. Weekly patterns suggest fine Zn and Pb are also dominated  
12 by regional transport (Supplement Fig. S9). P, S and K have been identified as  
13 tracers for mixed wood combustion and secondary sulphate (Amato et al., 2011;  
14 Richard et al., 2011), whereas Hammond et al. (2008) have identified S, K and Pb  
15 from mixed secondary sulphate and coal combustion. Br is usually associated with  
16 sea salt (Lee et al., 1994; Mazzei et al., 2007) or traffic emissions (Gotschi et al.,  
17 2005; Lee et al., 1994), but Maenhaut (1996) has also found Br, together with S, K,  
18 Pb and other elements in biomass burning. In this study, the diurnal cycle of fine Br is  
19 different from the Na, Mg and Cl cycles, but more similar to K. Br is thus likely more  
20 associated with wood burning than with other sources.

21 The time series of fine S, K, Zn, Pb at NK (very similar at MR and DE) are explored in  
22 relation to total PM<sub>10</sub> mass, wind direction and air mass origin, and compared to  
23 representative elements from the other emission groups (coarse Na, Si, S, Sb; Fig.  
24 9). Air mass origin was studied with back trajectories simulated for three case study  
25 periods (marine, European mainland and locally influenced) using the NAME model  
26 (Jones et al., 2007). Particles are released into the model atmosphere from the  
27 measurement location and their origin is tracked using meteorological fields from the  
28 Unified Model, a numerical weather prediction model. Each particle carries mass of  
29 one or more pollutant species and evolves by various physical and chemical  
30 processes during 24 h preceding arrival at NK. Potential emission source regions can  
31 be highlighted along the pathway to the measurement site at 0-100 m above ground.

32 Under marine air mass origin (case A, 18-24 January, Fig. 9) with strong W winds the  
33 concentrations of the fine mode elements are fairly low, whereas sea salt  
34 concentrations are enhanced (see Na in Fig. 9). Although the air mass has also  
35 passed over Ireland and the Midlands, the influence of these rather sparsely

1 populated regions on pollution levels seems small. This is confirmed by low total  
2 PM<sub>10</sub> mass and NO<sub>x</sub> concentrations. Enhanced fine fraction and total PM<sub>10</sub> mass  
3 concentrations (latter not shown) occur during north easterlies with high wind speeds  
4 from the European mainland (case B) bringing in pollutants through regional  
5 transport.

6 During this episode, both the urban background and rural site observed the highest  
7 concentrations for these trace elements of the entire campaign. Traffic influenced  
8 species were not enhanced during this pollution episode. Elevated concentrations of  
9 all trace elements, NO<sub>x</sub> and PM<sub>10</sub> mass occurred only during a local pollution episode  
10 of roughly 3 days caused by local air mass stagnation over London and the south  
11 eastern UK (case C). The very high concentrations observed in case B through  
12 regional transport from the European mainland were identified as the main reason for  
13 PM<sub>10</sub> limit exceedances at urban background sites in London by Charron et al.  
14 (2007), while exceedances were much less frequent under marine influenced air as  
15 represented by case A in this study.

16

#### 17 **4.3.2 Sea salt**

18 The sea salt group yields comparable, rather flat diurnal cycles for fine and  
19 intermediate mode Na, Mg and Cl, and coarse mode Na and Cl (Na in Fig. 6; others  
20 in Supplement Fig. S8), and no obvious weekly patterns (Na in Fig. 7; others in  
21 Supplement Fig. S9). This indicates that the regional transport of sea salt is probably  
22 the main source of Na, Mg and Cl, as seen in case A in Fig. 9.

23 Interestingly, although coarse mode sea salt exhibits no obvious temporal trend, the  
24 urban and kerb increments indicate additional source contributions besides regional  
25 transported sea salt. The urban increment might be caused by the natural sea salt  
26 gradient observed in the UK, with reducing concentrations from west to east (Fowler  
27 and Smith, 2000), while the kerb increment could be the result of road salt  
28 resuspension in addition to sea salt resuspension. Coarse mode Mg originates  
29 probably both from mineral dust and sea salt, because at MR with SW winds Mg  
30 correlates with Al and Si temporal trends, while with NE winds Mg correlates better  
31 with Na and Cl.

32

### 1 4.3.3 Mineral dust and traffic

2 Both mineral dust and traffic-related elements are strongly influenced by traffic  
3 patterns at MR, which are shown in Fig. 8 as the number of vehicles per 2 h split in  
4 LDV and HDV (shorter/longer than 5.2 m). HDV numbers peak in the morning,  
5 whereas LDV numbers peak in the evening when the flow of traffic leaves the urban  
6 area, consistent with Harrison et al. (2012b). A single peak during midday in the  
7 weekend compared to a double peak at weekdays is observed for LDV. HDV  
8 numbers show a similar pattern during weekdays, but with a reduced maximum on  
9 Saturday and a small maximum that is shifted towards midday on Sunday. Charron  
10 and Harrison (2005) reported similar traffic patterns during two years of traffic counts,  
11 and stated very small week-to-week variability, except during holidays.

12 The element diurnal (Fig. 6 for Si, Fe and Sb; Supplement Fig. S8 for others) and  
13 weekly (Fig. 7 for Si, Fe and Sb; Supplement Fig. S9 for others) cycles yield highest  
14 concentrations at MR and lower concentrations at NK and DE, consistent with  
15 observed urban and kerb increments. More importantly, and only retrievable with  
16 high time-resolved data, concentrations are higher during the day than at night, with  
17 night time concentrations at MR and NK similar to median urban background and  
18 rural concentrations, respectively, demonstrating the effects of local traffic and  
19 enhanced human exposure during daytime. Weekdays yield stronger increments  
20 than weekends and closely follow NO<sub>x</sub> and HDV traffic patterns (Fig. 8), indicating  
21 the strong influence of these vehicles on element concentrations. This confirms  
22 observations by Charron et al. (2007), who stated that PM<sub>10</sub> limit exceedances at MR  
23 are more likely to occur on weekdays, in combination with large regional  
24 contributions from the European mainland with easterly winds. Similarly,  
25 Barmpadimos et al. (2011) found strong weekly cycles for PM<sub>10-2.5</sub> and PM<sub>2.5</sub> mass  
26 concentrations in Switzerland over a 7-12 year period, with higher concentrations on  
27 weekdays and lowest on Sundays.

28 In the street canyon with SW winds, all coarse mode elements (including dust  
29 elements) except Na and Cl exhibit a double peak in the diurnal cycles, closely  
30 following the flow of traffic and confirming that traffic-related processes such as  
31 braking and resuspension dominate the concentration of most elements. With NE  
32 winds, source discrimination is possible between mineral dust (Si in Fig. 6) and  
33 traffic-related elements (Fe and Sb in Fig. 6). Mineral dust yields a strong maximum  
34 between 8:00 and 14:00 LT, and continued high concentrations throughout the day,  
35 while the traffic-related group yields a reduced double peak relative to SW winds.  
36 The increase in dust concentrations coincides with the start of traffic flows at 6:00 LT

1 resulting in resuspension of particles within the street canyon. However,  
2 concentrations decrease before traffic flows reduce, possibly as a result of increased  
3 mixing and dilution during boundary layer growth. At NK diurnal and weekly patterns  
4 of the dust and traffic groups yield similar variability but reduced concentrations  
5 relative to MR, which suggests increased human exposure during day time and  
6 weekdays and confirms that traffic dominates urban background element  
7 concentrations in London (see Dore et al., 2003). At DE, freshly emitted pollutants  
8 from London and other cities in the south eastern UK have been diluted and mixed  
9 with other pollutants during their transport to the rural background, resulting in no  
10 obvious diurnal and weekly patterns independent of size range.

11 The kerb increments at MR under SW winds were divided into two traffic-related  
12 groups: brake wear and other traffic-related elements. However, the diurnal and  
13 weekly cycles of all these elements correlate well and no obvious split into two  
14 groups is seen. Apparently, both groups are co-emitted as a single group under  
15 comparable vehicle fleet and/or set of driving conditions, at least on a 2 h time scale,  
16 but in different ratios at MR and NK. The ratio of these two element classes for SW to  
17 NE wind sectors at MR is almost 2, with the lack of difference between these classes  
18 supporting co-emission. In a future manuscript we will further explore the diurnal  
19 variability of emission sources at both sites with statistical analyses based on the  
20 Multilinear Engine (Canonaco et al., 2013; Paatero, 1999).

21

## 22 **5 Conclusions**

23 Aerosol trace element composition was measured at kerbside, urban background  
24 and rural sites in the European megacity of London during winter 2012. Sampling  
25 with rotating drum impactors (RDI) and subsequent measurements with synchrotron  
26 radiation-induced X-ray fluorescence spectrometry (SR-XRF) yielded trace element  
27 mass concentrations in  $PM_{10-2.5}$ ,  $PM_{2.5-1.0}$  and  $PM_{1.0-0.3}$  aerosol with a 2 h time  
28 resolution. Total median element mass concentrations of 5.44.0, 2.92.0 and 4.10.7  
29  $\mu\text{g m}^{-3}$  were found at kerbside, urban background and rural sites, respectively, which  
30 constitutes 4410 to 2416 % to total  $PM_{10}$  mass (highest at kerbside; lowest at rural  
31 site), neglecting the corresponding oxides. The contribution of emission sources to  
32 coarse fraction elements was on average largest at kerbside (6365 %) and reduced  
33 for urban background (5051 %) and rural sites (4749 %).

34 Urban and kerb increments were defined as the concentration ratios of urban  
35 background to rural, and kerbside to urban background, respectively, and the kerb

1 increments were further explored as a function of wind direction. The group with the  
2 largest kerb increments consisted of elements typically associated with brake wear  
3 (Cu, Zr, Mo, Sn, Sb, Ba). The second largest kerb increments were observed for  
4 anthropogenically-influenced elements typically assigned to non-brake wear traffic  
5 emissions (Cr, Mn, Fe, Zn, Pb) but also V and Ni. This could indicate either a traffic  
6 source for these elements or a similar kerbside-to-urban emission gradient. Kerb  
7 increments were larger for the brake wear group and under SW winds due to local  
8 street canyon effects, with coarse fraction increments between 10.4 and 16.6 for SW  
9 winds (3.3-6.9 for NE winds) against increments for the anthropogenically-influenced  
10 group between 5.7 and 8.2 for SW winds (2.6-3.0 for NE winds). The kerb increments  
11 for all these elements in the  $PM_{10-2.5}$  size fraction are roughly twice that of the  $PM_{1.0-0.3}$   
12 fraction. Urban increments (no distinction between both groups) were around 3.0. In  
13 addition to direct emissions, traffic-related processes influence the concentrations of  
14 other elements by resuspension, with mineral dust (Al, Si, Ca, Ti, Sr) increments of  
15 1.3-3.3.

16 The highly time-resolved data enabled studying diurnal patterns. The cycles of  
17 mineral dust elements and coarse Na, Mg and Cl both indicate major concentration  
18 enhancements during periods of heavy traffic, whereas regionally-influenced  
19 elements (fine P, S, K, Zn, Br, Pb) showed no enhancements. All traffic-related  
20 elements at the kerbside site yielded temporal patterns similar to variations in heavy  
21 duty vehicle numbers as opposed to total vehicle numbers, and resulted in enhanced  
22 exposure to elements during day time and weekdays. Traffic-related processes  
23 therefore exhibit a dominant influence on air quality at the kerbside and urban  
24 background sites, and should be the main focus of health effect studies and  
25 mitigation strategies. With technological improvements for the reduction of traffic  
26 exhaust emissions, the traffic contribution to coarse PM is becoming more important  
27 as shown by decreasing  $PM_{2.5}$  mass trends with no significant changes of coarse PM  
28 (Barmpadimos et al., 2012).

29 Trace element and total  $PM_{10}$  mass concentrations are also affected by mesoscale  
30 meteorology, increasing with the transport of air masses from the European  
31 mainland. Under these conditions, coarse and intermediate fraction trace elements  
32 are hardly affected, but fine fraction elements showed elevated concentrations. Trace  
33 element concentrations in London are therefore influenced by both local and regional  
34 sources, with coarse and intermediate fractions dominated by anthropogenic  
35 activities (particularly traffic-induced resuspension and wearing processes), whereas  
36 fine fractions are significantly influenced by regional processes.

1 These observations highlight both the strong influence of regional factors on overall  
2 air quality, as well as the need for detailed characterization of urban micro-  
3 environments for accurate assessment of human exposure to airborne particulates  
4 and the associated health risks.

5

## 6 **Acknowledgements**

7 This research, which was conducted in the context of the ClearfLo project, is mainly  
8 financed by the Swiss National Science Foundation (SNSF grant 200021\_132467/1),  
9 the ClearfLo project (NERC grant NE/H00324X/1) and the European Community's  
10 Seventh Framework Programme (FP/2007-2013, grant number 312284). The Detling  
11 site was supported by the US Department of Energy Atmospheric Systems Research  
12 Program (DOE Award No. DE-SC0006002). J.G. Slowik acknowledges support from  
13 the SNSF through the Ambizione program (grant PX00P2\_31673). Filter digestions  
14 were carried out by the wet geochemistry laboratory at Royal Holloway, University of  
15 London. Empa loaned us a RDI during the ClearfLo project. Parts of the work were  
16 carried out at the Swiss Light Source, Paul Scherrer Institute, Villigen, Switzerland.  
17 We thank Andreas Jaggi for technical support at the beamline X05DA. Parts were  
18 performed at the light source facility DORIS III at HASYLAB/DESY. DESY is a  
19 member of the Helmholtz Association (HGF). We thank Christophe Friehe for excellent  
20 support in acquiring and testing the detector, and we thank Peter Lienemann and  
21 Sylvia Köchli for valuable input for the production of calibration standards.

22

## 23 **References**

- 24 Amato, F., Pandolfi, M., Escrig, A., Querol, X., Alastuey, A., Pey, J., Perez, N., and  
25 Hopke, P. K.: Quantifying road dust resuspension in urban environment by Multilinear  
26 Engine: A comparison with PMF2, *Atmos. Env.*, 43, 2770-2780, 2009.
- 27 Amato, F., Viana, M., Richard, A., Furger, M., Prevot, A. S. H., Nava, S., Lucrelli, F.,  
28 Bukowiecki, N., Alastuey, A., Reche, C., Moreno, T., Pandolfi, M., Pey, J., and  
29 Querol, X.: Size and time-resolved roadside enrichment of atmospheric particulate  
30 pollutants, *Atmos. Chem. Phys.*, 11, 2917-2931, 2011.
- 31 Amato, F., Schaap, M., Denier van der Gon, H. A. C., Pandolfi, M., Alastuey, A.,  
32 Keuken, M., and Querol, X.: Short-term variability of mineral dust, metals and carbon  
33 emission from road dust resuspension, *Atmos. Env.*, 74, 134-140, 2013.
- 34 Arnold, S. J., ApSimon, H., Barlow, J., Belcher, S., Bell, M., Boddy, J. W., Britter, R.,  
35 Cheng, H., Clark, R., Colvile, R. N., Dimitroulopoulou, S., Dobre, A., Grealley, B.,  
36 Kaur, S., Knights, A., Lawton, T., Makepeace, A., Martin, D., Neophytou, M., Neville,  
37 S., Nieuwenhuijsen, M., Nickless, G., Price, C., Robins, A., Shallcross, D.,  
38 Simmonds, P., Smalley, R. J., Tate, J., Tomlin, A. S., Wang, H., and Walsh, P.:



1 Introduction to the DAPPLE Air Pollution Project, *Sci. Total Environ.*, 332, 139-153,  
2 2004.

3 Balogun, A. A., Tomlin, A. S., Wood, C. R., Barlow, J. F., Belcher, S. E., Smalley, R.  
4 J., Lingard, J. J. N., Arnold, S. J., Dobre, A., Robins, A. G., Martin, D., and  
5 Shallcross, D. E.: In-street wind direction variability in the vicinity of a busy  
6 intersection in central London, *Bound.-Layer Meteorol.*, 136, 489-513,  
7 doi:10.1007/s10546-010-9515-y, 2010.

8 Barmpadimos, I., Nufer, M., Oderbolz, D. C., Keller, J., Aksoyoglu, S., Hueglin, C.,  
9 Baltensperger, U., and Prévôt, A. S. H.: The weekly cycle of ambient concentrations  
10 and traffic emissions of coarse (PM<sub>10</sub>–PM<sub>2.5</sub>) atmospheric particles, *Atmos. Env.*,  
11 45, 4580-4590, 2011.

12 Barmpadimos, I., Keller, J., Oderbolz, D., Hueglin, C., and Prévôt, A. S. H.: One  
13 decade of parallel fine (PM<sub>2.5</sub>) and coarse (PM<sub>10</sub>–PM<sub>2.5</sub>) particulate matter  
14 measurements in Europe: trends and variability, *Atmos. Chem. Phys.*, 12, 3189-  
15 3203, doi:10.5194/acp-12-3189-2012, 2012.

16 Bigi, A., and Harrison, R. M.: Analysis of the air pollution climate at a central urban  
17 background site, *Atmos. Env.*, 44, 2004-2012, 2010.

18 Bohnenstengel, S. I., Evans, S., Clark, P. A., and Belcher, S. E.: Simulations of the  
19 London urban heat island, *Quart. J. Roy. Meteorol. Soc.*, 137, 1625-1640,  
20 doi:10.1002/qj.855, 2011.

21 Bohnenstengel, S. I., Hamilton, I., Davies, M., and Belcher, S. E.: Impact of  
22 anthropogenic heat emissions on London's temperatures, *Quart. J. Roy. Meteorol.*  
23 *Soc.*, doi:10.1002/qj.2144, 2013.

24 Bohnenstengel, S. I., Belcher, S. E., Aiken, A., Allan, J. D., Allen, G., Bacak, A.,  
25 Bannan, T. J., Barlow, J. F., Beddows, D. C. S., Bloss, W. J., Booth, A. M., Chemel,  
26 C., Coceal, O., Di Marco, C. F., Dubey, M. K., Faloon, K. H., Fleming, Z. L., Furger,  
27 M., Gietl, J. K., Graves, R. R., Green, D. C., Grimmond, C. S. B., Halios, C. H.,  
28 Hamilton, J. F., Harrison, R. M., Heal, M. R., Heard, D. E., Helfter, C., Herndon, S.  
29 C., Holmes, R. E., Hopkins, J. R., Jones, A. M., Kelly, F. J., Kotthaus, S., Langford,  
30 B., Lee, J. D., Leigh, R. J., Lewis, A. C., Lidster, R. T., Lopez-Hilfiker, F. D.,  
31 McQuaid, J. B., Mohr, C., Monks, P. S., Nemitz, E., Ng, N. L., Percival, C. J., Prévôt,  
32 A. S. H., Ricketts, H. M. A., Sokhi, R., Stone, D., Thornton, J. A., Tremper, A. H.,  
33 Valach, A. C., Visser, S., Whalley, L. K., Williams, L. R., Xu, L., Young, D. E., and  
34 Zotter, P.: Meteorology, air quality, and health in London: The ClearLo project, *Bull.*  
35 *Am. Meteor. Soc.*, (online release), doi:10.1175/bams-d-12-00245.1, 2014.

36 Boogaard, H., Kos, G. P. A., Weijers, E. P., Janssen, N. A. H., Fischer, P. H., van der  
37 Zee, S. C., de Hartog, J. J., and Hoek, G.: Contrast in air pollution components  
38 between major streets and background locations: Particulate matter mass, black  
39 carbon, elemental composition, nitrogen oxide and ultrafine particle number, *Atmos.*  
40 *Env.*, 45, 650-658, 2011.

41 Bukowiecki, N., Hill, M., Gehrig, R., Zwicky, C. N., Lienemann, P., Hegedus, F.,  
42 Falkenberg, G., Weingartner, E., and Baltensperger, U.: Trace metals in ambient air:  
43 Hourly size-segregated mass concentrations determined by synchrotron-XRF,  
44 *Environ. Sci. Technol.*, 39, 5754-5762, 2005.

45 Bukowiecki, N., Lienemann, P., Zwicky, C. N., Furger, M., Richard, A., Falkenberg,  
46 G., Rickers, K., Grolimund, D., Borca, C., Hill, M., Gehrig, R., and Baltensperger, U.:  
47 X-ray fluorescence spectrometry for high throughput analysis of atmospheric aerosol  
48 samples: The benefits of synchrotron X-rays, *Spectrochim. Acta B*, 63, 929-938,  
49 2008.

- 1 Bukowiecki, N., Gehrig, R., Lienemann, P., Hill, M., Figi, R., Buchmann, B., Furger,  
2 M., Richard, A., Mohr, C., Weimer, S., Prevot, A. S. H., and Baltensperger, U.: PM10  
3 emission factors of abrasion particles from road traffic, Schweizerische  
4 Eidgenossenschaft, 2009a.
- 5 Bukowiecki, N., Lienemann, P., Hill, M., Figi, R., Richard, A., Furger, M., Rickers, K.,  
6 Falkenberg, G., Zhao, Y. J., Cliff, S. S., Prevot, A. S. H., Baltensperger, U.,  
7 Buchmann, B., and Gehrig, R.: Real-world emission factors for antimony and other  
8 brake wear related trace elements: Size-segregated values for light and heavy duty  
9 vehicles, *Environ. Sci. Technol.*, 43, 8072-8078, 2009b.
- 10 Bukowiecki, N., Richard, A., Furger, M., Weingartner, E., Aguirre, M., Huthwelker, T.,  
11 Lienemann, P., Gehrig, R., and Baltensperger, U.: Deposition uniformity and particle  
12 size distribution of ambient aerosol collected with a rotating drum impactor, *Aerosol  
13 Sci. Technol.*, 43, 891-901, 2009c.
- 14 Bukowiecki, N., Lienemann, P., Hill, M., Furger, M., Richard, A., Amato, F., Prevot, A.  
15 S. H., Baltensperger, U., Buchmann, B., and Gehrig, R.: PM10 emission factors for  
16 non-exhaust particles generated by road traffic in an urban street canyon and along a  
17 freeway in Switzerland, *Atmos. Env.*, 44, 2330-2340, 2010.
- 18 Calzolari, G., Chiari, M., Lucarelli, F., Nava, S., and Portarena, S.: Proton induced  
19 gamma-ray emission yields for the analysis of light elements in aerosol samples in an  
20 external beam set-up, *Nucl. Instrum. Methods Phys. Res. Sect. B-Beam Interact.  
21 Mater. Atoms*, 268, 1540-1545, 2010.
- 22 Canonaco, F., Crippa, M., Slowik, J. G., Baltensperger, U., and Prevot, A. S. H.:  
23 SoFi, an IGOR-based interface for the efficient use of the generalized multilinear  
24 engine (ME-2) for the source apportionment: ME-2 application to aerosol mass  
25 spectrometer data, *Atmos. Meas. Tech.*, 6, 3649-3661, doi:10.5194/amt-6-3649-  
26 2013, 2013.
- 27 Charron, A., and Harrison, R. M.: Fine (PM<sub>2.5</sub>) and coarse (PM<sub>2.5-10</sub>) particulate  
28 matter on a heavily trafficked London highway: Sources and processes, *Environ. Sci.  
29 Technol.*, 39, 7768-7776, doi:10.1021/es050462i, 2005.
- 30 Charron, A., Harrison, R. M., and Quincey, P.: What are the sources and conditions  
31 responsible for exceedences of the 24 h PM<sub>10</sub> limit value (50 µg m<sup>-3</sup>) at a heavily  
32 trafficked London site?, *Atmos. Env.*, 41, 1960-1975, 2007.
- 33 Crippa, M., DeCarlo, P. F., Slowik, J. G., Mohr, C., Heringa, M. F., Chirico, R.,  
34 Poulain, L., Freutel, F., Sciare, J., Cozic, J., Di Marco, C. F., Elsasser, M., Nicolas, J.  
35 B., Marchand, N., Abidi, E., Wiedensohler, A., Drewnick, F., Schneider, J., Borrmann,  
36 S., Nemitz, E., Zimmermann, R., Jaffrezo, J. L., Prévôt, A. S. H., and Baltensperger,  
37 U.: Wintertime aerosol chemical composition and source apportionment of the  
38 organic fraction in the metropolitan area of Paris, *Atmos. Chem. Phys.*, 13, 961-981,  
39 doi:10.5194/acp-13-961-2013, 2013.
- 40 DeCarlo, P. F., Kimmel, J. R., Trimborn, A., Northway, M. J., Jayne, J. T., Aiken, A.  
41 C., Gonin, M., Fuhrer, K., Horvath, T., Docherty, K. S., Worsnop, D. R., and Jimenez,  
42 J. L.: Field-deployable, high-resolution, time-of-flight aerosol mass spectrometer,  
43 *Anal. Chem.*, 78, 8281-8289, doi:10.1021/ac061249n, 2006.
- 44 Dockery, D. W., and Pope, C. A., III: Acute respiratory effects of particulate air  
45 pollution, in: *Annual Review of Public Health*, edited by: Omenn, G. S., *Annual  
46 Review of Public Health*, Annual Reviews Inc., P.O. Box 10139, 4139 El Camino  
47 Way, Palo Alto, California 94306, USA, 107-132, 1994.
- 48 Dore, C. J., Goodwin, J. W. L., Watterson, J. D., Murrels, T. P., Passant, N. R.,  
49 Hobson, M. M., Haigh, K. E., Baggott, S. L., Pye, S. T., Coleman, P. J., and King, K.

1 R.: UK Emissions of Air Pollutants 1970 to 2001, National Atmospheric Emissions  
2 Inventory, 2003.

3 Flechsig, U., Jaggi, A., Spielmann, S., Padmore, H. A., and MacDowell, A. A.: The  
4 optics beamline at the Swiss Light Source, Nucl. Instrum. Methods Phys. Res. Sect.  
5 A-Accel. Spectrom. Dect. Assoc. Equip., 609, 281-285, 2009.

6 Formenti, P., Prati, P., Zucchiatti, A., Lucarelli, F., and Mando, P. A.: Aerosol study in  
7 the town of Genova with a PIXE analysis, Nucl. Instrum. Methods Phys. Res. Sect.  
8 B-Beam Interact. Mater. Atoms, 113, 359-362, 1996.

9 Formenti, P., Nava, S., Prati, P., Chevaillier, S., Klaver, A., Lafon, S., Mazzei, F.,  
10 Calzolari, G., and Chiari, M.: Self-attenuation artifacts and correction factors of light  
11 element measurements by X-ray analysis: Implication for mineral dust composition  
12 studies, J. Geophys. Res.-Atmos., 115, 8, doi:10.1029/2009jd012701, 2010.

13 Fowler, D., and Smith, R.: Spatial and temporal variability in the deposition of  
14 acidifying species in the UK between 1986 and 1997, Department of Environment,  
15 Food and Rural Affairs, 2000.

16 Franklin, M., Koutrakis, P., and Schwartz, J.: The role of particle composition on the  
17 association between PM<sub>2.5</sub> and mortality, Epidemiology, 19, 680-689,  
18 doi:10.1097/ede.0b013e3181812bb7, 2008.

19 Freutel, F., Schneider, J., Drewnick, F., von der Weiden-Reinmüller, S. L., Crippa,  
20 M., Prévôt, A. S. H., Baltensperger, U., Poulain, L., Wiedensohler, A., Sciare, J.,  
21 Sarda-Estève, R., Burkhardt, J. F., Eckhardt, S., Stohl, A., Gros, V., Colomb, A.,  
22 Michoud, V., Doussin, J. F., Borbon, A., Haeffelin, M., Morille, Y., Beekmann, M., and  
23 Borrmann, S.: Aerosol particle measurements at three stationary sites in the  
24 megacity of Paris during summer 2009: meteorology and air mass origin dominate  
25 aerosol particle composition and size distribution, Atmos. Chem. Phys., 13, 933-959,  
26 doi:10.5194/acp-13-933-2013, 2013.

27 Gotschi, T., Hazenkamp-Von Arxb, M. E., Heinrich, J., Bono, R., Burney, P.,  
28 Forsberg, B., Jarvis, D., Maldonado, J., Norback, D., Stern, W. B., Sunyer, J., Toren,  
29 K., Verlato, G., Villani, S., and Kunzli, N.: Elemental composition and reflectance of  
30 ambient fine particles at 21 European locations, Atmos. Env., 39, 5947-5958, 2005.

31 Hammond, D. M., Dvonch, J. T., Keeler, G. J., Parker, E. A., Kamal, A. S., Barres, J.  
32 A., Yip, F. Y., and Brakefield-Caldwell, W.: Sources of ambient fine particulate matter  
33 at two community sites in Detroit, Michigan, Atmos. Env., 42, 720-732, 2008.

34 Harrison, R. M., and Jones, A. M.: Multisite study of particle number concentrations  
35 in urban air, Environ. Sci. Technol., 39, 6063-6070, doi:10.1021/es040541e, 2005.

36 Harrison, R. M., Yin, J., Mark, D., Stedman, J., Appleby, R. S., Booker, J., and  
37 Moorcroft, S.: Studies of the coarse particle (2.5–10 µm) component in UK urban  
38 atmospheres, Atmos. Env., 35, 3667-3679, 2001.

39 Harrison, R. M., Stedman, J., and Derwent, D.: New Directions: Why are PM<sub>10</sub>  
40 concentrations in Europe not falling?, Atmos. Env., 42, 603-606, 2008.

41 Harrison, R. M., Beddows, D. C. S., and Dall'Osto, M.: PMF analysis of wide-range  
42 particle size spectra collected on a major highway, Environ. Sci. Technol., 45, 5522-  
43 5528, 2011.

44 Harrison, R. M., Dall'Osto, M., Beddows, D. C. S., Thorpe, A. J., Bloss, W. J., Allan,  
45 J. D., Coe, H., Dorsey, J. R., Gallagher, M., Martin, C., Whitehead, J., Williams, P. I.,  
46 Jones, R. L., Langridge, J. M., Benton, A. K., Ball, S. M., Langford, B., Hewitt, C. N.,  
47 Davison, B., Martin, D., Petersson, K. F., Henshaw, S. J., White, I. R., Shallcross, D.  
48 E., Barlow, J. F., Dunbar, T., Davies, F., Nemitz, E., Phillips, G. J., Helfter, C., Di  
49 Marco, C. F., and Smith, S.: Atmospheric chemistry and physics in the atmosphere of

1 a developed megacity (London): an overview of the REPARTEE experiment and its  
2 conclusions, *Atmos. Chem. Phys.*, 12, 3065-3114, 2012a.

3 Harrison, R. M., Jones, A. M., Gietl, J., Yin, J., and Green, D. C.: Estimation of the  
4 contributions of brake dust, tire wear, and resuspension to nonexhaust traffic  
5 particles derived from atmospheric measurements, *Environ. Sci. Technol.*, 46, 6523-  
6 6529, doi:10.1021/es300894r, 2012b.

7 Harrison, R. M., Laxen, D., Moorcroft, S., and Laxen, K.: Processes affecting  
8 concentrations of fine particulate matter (PM<sub>2.5</sub>) in the UK atmosphere, *Atmos. Env.*,  
9 46, 115-124, 2012c.

10 Janssen, N. A. H., Van Mansom, D. F. M., Van Der Jagt, K., Harssema, H., and  
11 Hoek, G.: Mass concentration and elemental composition of airborne particulate  
12 matter at street and background locations, *Atmos. Env.*, 31, 1185-1193, 1997.

13 Jones, A. M., Harrison, R. M., and Baker, J.: The wind speed dependence of the  
14 concentrations of airborne particulate matter and NO<sub>x</sub>, *Atmos. Env.*, 44, 1682-1690,  
15 2010.

16 Jones, A. R., Thomson, D. J., Hort, M., and Devenish, B.: The UK Met Office's next-  
17 generation atmospheric dispersion model, NAME III, *Air Pollution Modeling and its*  
18 *Application XVII*, edited by: Borrego, C., and Norman, A.-L., Springer, 2007.

19 Kelly, F. J., and Fussell, J. C.: Size, source and chemical composition as  
20 determinants of toxicity attributable to ambient particulate matter, *Atmos. Env.*, 60,  
21 504-526, 2012.

22 Lee, D. S., Garland, J. A., and Fox, A. A.: Atmospheric concentrations of trace  
23 elements in urban areas of the United Kingdom, *Atmos. Env.*, 28, 2691-2713, 1994.

24 Lin, C. C., Chen, S. J., Huang, K. L., Hwang, W. I., Chang-Chien, G. P., and Lin, W.  
25 Y.: Characteristics of metals in nano/ultrafine/fine/coarse particles collected beside a  
26 heavily trafficked road, *Environ. Sci. Technol.*, 39, 8113-8122, 2005.

27 Lucarelli, F., Mando, P. A., Nava, S., Valerio, M., Prati, P., and Zucchiatti, A.:  
28 Elemental composition of urban aerosol collected in Florence, Italy, *Environ. Monit.*  
29 *Assess.*, 65, 165-173, 2000.

30 Maenhaut, W.: "Global Change" related and other atmospheric aerosol research at  
31 the University of Gent, and the role of PIXE therein, *Nucl. Instrum. Methods Phys.*  
32 *Res. Sect. B-Beam Interact. Mater. Atoms*, 109, 419-428, 1996.

33 Mavrogianni, A., Davies, M., Batty, M., Belcher, S. E., Bohnenstengel, S. I.,  
34 Carruthers, D., Chalabi, Z., Croxford, B., Demanuele, C., Evans, S., Giridharan, R.,  
35 Hacker, J. N., Hamilton, I., Hogg, C., Hunt, J., Kolokotroni, M., Martin, C., Milner, J.,  
36 Rajapaksha, I., Ridley, I., Steadman, J. P., Stocker, J., Wilkinson, P., and Ye, Z.: The  
37 comfort, energy and health implications of London's urban heat island, *Build Serv.*  
38 *Eng. Res. Technol.*, 32, 35-52, doi:10.1177/0143624410394530, 2011.

39 Mazzei, F., Lucarelli, F., Nava, S., Prati, P., Valli, G., and Vecchi, R.: A new  
40 methodological approach: The combined use of two-stage streaker samplers and  
41 optical particle counters for the characterization of airborne particulate matter, *Atmos.*  
42 *Env.*, 41, 5525-5535, 2007.

43 Minguillón, M. C., Cirach, M., Hoek, G., Brunekreef, B., Tsai, M., de Hoogh, K.,  
44 Jedynska, A., Kooter, I. M., Nieuwenhuijsen, M., and Querol, X.: Spatial variability of  
45 trace elements and sources for improved exposure assessment in Barcelona, *Atmos.*  
46 *Env.*, 89, 268-281, 2014.

47 Moffet, R. C., Desyaterik, Y., Hopkins, R. J., Tivanski, A. V., Gilles, M. K., Wang, Y.,  
48 Shutthanandan, V., Molina, L. T., Abraham, R. G., Johnson, K. S., Mugica, V.,

- 1 Molina, M. J., Laskin, A., and Prather, K. A.: Characterization of aerosols containing  
2 Zn, Pb, and Cl from an industrial region of Mexico City, *Environ. Sci. Technol.*, 42,  
3 7091-7097, 2008.
- 4 Mohr, C., Lopez-Hilfiker, F. D., Zotter, P., Prévôt, A. S. H., Xu, L., Ng, N. L., Herndon,  
5 S. C., Williams, L. R., Franklin, J. P., Zahniser, M. S., Worsnop, D. R., Knighton, W.  
6 B., Aiken, A. C., Gorkowski, K. J., Dubey, M. K., Allan, J. D., and Thornton, J. A.:  
7 Contribution of nitrated phenols to wood burning brown carbon light absorption in  
8 Detling, United Kingdom during winter time, *Environ. Sci. Technol.*, 47, 6316-6324,  
9 doi:10.1021/es400683v, 2013.
- 10 Moreno, T., Karanasiou, A., Amato, F., Lucarelli, F., Nava, S., Calzolari, G., Chiari,  
11 M., Coz, E., Artinano, B., Lumberras, J., Borge, R., Boldo, E., Linares, C., Alastuey,  
12 A., Querol, X., and Gibbons, W.: Daily and hourly sourcing of metallic and mineral  
13 dust in urban air contaminated by traffic and coal-burning emissions, *Atmos. Env.*,  
14 68, 33-44, doi:10.1016/j.atmosenv.2012.11.037, 2013.
- 15 Nolte, C. G., Bhave, P. V., Arnold, J. R., Dennis, R. L., Zhang, K. M., and Wexler, A.  
16 S.: Modeling urban and regional aerosols—Application of the CMAQ-UCD Aerosol  
17 Model to Tampa, a coastal urban site, *Atmos. Env.*, 42, 3179-3191, 2008.
- 18 Paatero, P.: The multilinear engine—A table-driven, least squares program for  
19 solving multilinear problems, including the n-way parallel factor analysis model, *J.*  
20 *Comput. Graph. Stat.*, 8, 854-888, doi:10.1080/10618600.1999.10474853, 1999.
- 21 Putaud, J. P., Van Dingenen, R., Alastuey, A., Bauer, H., Birmili, W., Cyrys, J.,  
22 Flentje, H., Fuzzi, S., Gehrig, R., Hansson, H. C., Harrison, R. M., Herrmann, H.,  
23 Hitenberger, R., Hüglin, C., Jones, A. M., Kasper-Giebl, A., Kiss, G., Koussa, A.,  
24 Kuhlbusch, T. A. J., Löschau, G., Maenhaut, W., Molnar, A., Moreno, T., Pekkanen,  
25 J., Perrino, C., Pitz, M., Puxbaum, H., Querol, X., Rodriguez, S., Salma, I., Schwarz,  
26 J., Smolik, J., Schneider, J., Spindler, G., ten Brink, H., Tursic, J., Viana, M.,  
27 Wiedensohler, A., and Raes, F.: A European aerosol phenomenology – 3: Physical  
28 and chemical characteristics of particulate matter from 60 rural, urban, and kerbside  
29 sites across Europe, *Atmos. Env.*, 44, 1308-1320, 2010.
- 30 Querol, X., Viana, M., Alastuey, A., Amato, F., Moreno, T., Castillo, S., Pey, J., de la  
31 Rosa, J., Sánchez de la Campa, A., Artíñano, B., Salvador, P., García Dos Santos,  
32 S., Fernández-Patier, R., Moreno-Grau, S., Negral, L., Minguillón, M. C., Monfort, E.,  
33 Gil, J. I., Inza, A., Ortega, L. A., Santamaría, J. M., and Zabalza, J.: Source origin of  
34 trace elements in PM from regional background, urban and industrial sites of Spain,  
35 *Atmos. Env.*, 41, 7219-7231, 2007.
- 36 Reche, C., Moreno, T., Amato, F., Viana, M., van Drooge, B. L., Chuang, H.-C.,  
37 Bérubé, K., Jones, T., Alastuey, A., and Querol, X.: A multidisciplinary approach to  
38 characterise exposure risk and toxicological effects of PM10 and PM2.5 samples in  
39 urban environments, *Ecotox. Environ. Safe.*, 78, 327-335, 2012.
- 40 Richard, A., Bukowiecki, N., Lienemann, P., Furger, M., Fierz, M., Minguillon, M. C.,  
41 Weideli, B., Figi, R., Flechsig, U., Appel, K., Prevot, A. S. H., and Baltensperger, U.:  
42 Quantitative sampling and analysis of trace elements in atmospheric aerosols:  
43 impactor characterization and synchrotron-XRF mass calibration, *Atmos. Meas.*  
44 *Tech.*, 3, 1473-1485, 2010.
- 45 Richard, A., Gianini, M. F. D., Mohr, C., Furger, M., Bukowiecki, N., Minguillon, M. C.,  
46 Lienemann, P., Flechsig, U., Appel, K., DeCarlo, P. F., Heringa, M. F., Chirico, R.,  
47 Baltensperger, U., and Prevot, A. S. H.: Source apportionment of size and time  
48 resolved trace elements and organic aerosols from an urban courtyard site in  
49 Switzerland, *Atmos. Chem. Phys.*, 11, 8945-8963, 2011.

1 Salcedo, D., Laskin, A., Shutthanandan, V., and Jimenez, J. L.: Feasibility of the  
2 detection of trace elements in particulate matter using online high-resolution aerosol  
3 mass spectrometry, *Aerosol Sci. Technol.*, 46, 1187-1200,  
4 doi:10.1080/02786826.2012.701354, 2012.

5 Theodosi, C., Grivas, G., Zarnpas, P., Chaloulakou, A., and Mihalopoulos, N.: Mass  
6 and chemical composition of size-segregated aerosols (PM<sub>1</sub>, PM<sub>2.5</sub>, PM<sub>10</sub>) over  
7 Athens, Greece: local versus regional sources, *Atmos. Chem. Phys.*, 11, 11895-  
8 11911, doi:10.5194/acp-11-11895-2011, 2011.

9 Turoczi, B., Hoffer, A., Toth, A., Kovats, N., Acs, A., Ferincz, A., Kovacs, A., and  
10 Gelencser, A.: Comparative assessment of ecotoxicity of urban aerosol, *Atmos.*  
11 *Chem. Phys.*, 12, 7365-7370, doi:10.5194/acp-12-7365-2012, 2012.

12 Viana, M., Kuhlbusch, T. A. J., Querol, X., Alastuey, A., Harrison, R. M., Hopke, P.  
13 K., Winiwarter, W., Vallius, A., Szidat, S., Prevot, A. S. H., Hueglin, C., Bloemen, H.,  
14 Wahlin, P., Vecchi, R., Miranda, A. I., Kasper-Giebl, A., Maenhaut, W., and  
15 Hitzenberger, R.: Source apportionment of particulate matter in Europe: A review of  
16 methods and results, *J. Aerosol Sci.*, 39, 827-849,  
17 doi:10.1016/j.jaerosci.2008.05.007, 2008.

18 Wedepohl, K.: The composition of the continental crust, *Geochim. Cosmochim. Ac.*,  
19 59, 1217-1232, doi:10.1016/0016-7037(95)00038-2, 1995.

20 Weijers, E. P., Schaap, M., Nguyen, L., Matthijsen, J., van der Gon, H., ten Brink, H.  
21 M., and Hoogerbrugge, R.: Anthropogenic and natural constituents in particulate  
22 matter in the Netherlands, *Atmos. Chem. Phys.*, 11, 2281-2294, doi:10.5194/acp-11-  
23 2281-2011, 2011.

24 Witt, M. L. I., Meheran, N., Mather, T. A., de Hoog, J. C. M., and Pyle, D. M.: Aerosol  
25 trace metals, particle morphology and total gaseous mercury in the atmosphere of  
26 Oxford, UK, *Atmos. Env.*, 44, 1524-1538, doi:10.1016/j.atmosenv.2010.01.008, 2010.

27 Wood, C. R., Lacser, A., Barlow, J. F., Padhra, A., Belcher, S. E., Nemitz, E., Helfter,  
28 C., Famulari, D., and Grimmond, C. S. B.: Turbulent flow at 190 m height above  
29 London during 2006-2008: A climatology and the applicability of similarity theory,  
30 *Bound.-Layer Meteor.*, 137, 77-96, doi:10.1007/s10546-010-9516-x, 2010.

31 Xiao, Z. H., Shao, L. Y., Zhang, N., Wang, J., and Wang, J. Y.: Heavy metal  
32 compositions and bioreactivity of airborne PM<sub>10</sub> in a valley-shaped city in  
33 northwestern China, *Aerosol Air Qual. Res.*, 13, 1116-1125,  
34 doi:10.4209/aaqr.2012.10.0287, 2013.

35 Zhou, J. A., Ito, K., Lall, R., Lippmann, M., and Thurston, G.: Time-series analysis of  
36 mortality effects of fine particulate matter components in Detroit and Seattle, *Environ.*  
37 *Health Perspect.*, 119, 461-466, doi:10.1289/ehp.1002613, 2011.

38 Zhou, Y., and Levy, J. I.: The impact of urban street canyons on population exposure  
39 to traffic-related primary pollutants, *Atmos. Env.*, 42, 3087-3098, 2008.

40

1 **Tables**

2

3 **Table 1.** Measurement campaign details.

Site	Start/End date	Site type	Sampling time	Inlet height	Sampling platform
MR	11 Jan – 14 Feb 2012	kerbside	2 h	4 m	container at 1 m from road
NK	11 Jan – 9 Feb 2012	urban background	2 h	4 m	container
DE	17 Jan – 13 Feb 2012	rural	2 h	1.5 m	grass field

4

5

1 | **Table 2. Self-absorption correction factors.**

	Geometric mean diameter ( $\mu\text{m}$ )	Density <sup>a</sup> ( $\text{g cm}^{-3}$ )	Na <sup>b</sup>	Mg <sup>b</sup>	Al <sup>b</sup>	Si <sup>b</sup>
Calibration standard 1	9	2.19	0.22 <i>0.49</i>		0.43 <i>0.23</i>	
Calibration standard 2	9	2.27		0.32 <i>0.33</i>		0.51 <i>0.17</i>
PM <sub>10-2.5</sub> sample	5	2.00	0.43 <i>0.40</i>	0.58 <i>0.25</i>	0.70 <i>0.15</i>	0.79 <i>0.10</i>
PM <sub>2.5-1.0</sub> sample	1.6	2.00	0.74 <i>0.40</i>	0.83 <i>0.25</i>	0.89 <i>0.15</i>	0.93 <i>0.10</i>

2 | <sup>a</sup> Average density of the calibration standards and of ambient aerosol. The composition of  
3 | calibration standard 1 is Na<sub>3.76</sub>Al<sub>3.76</sub>P<sub>3.76</sub>Cl<sub>3.76</sub>Ca<sub>3.76</sub>CoN<sub>8</sub>O<sub>24</sub>, of calibration standard 2  
4 | Mg<sub>3.76</sub>Si<sub>3.76</sub>S<sub>3.76</sub>K<sub>3.76</sub>Ca<sub>3.76</sub>CoN<sub>7</sub>O<sub>21</sub>, and of ambient samples C<sub>39</sub>H<sub>29</sub>N<sub>10</sub>O<sub>18</sub>S<sub>3</sub>Fe.

5 | <sup>b</sup> Attenuation factors and *a* (italic values,  $\mu\text{m}^{-1}$ ;  $a = 2/3 * \mu * \rho$  with  $\mu$  the mass attenuation  
6 | coefficient ( $\text{cm}^2 \text{g}^{-1}$ ) and  $\rho$  the particle mass density ( $\text{g cm}^{-3}$ )) according to Eq. (4) in Formenti  
7 | et al. (2010).

8  
9



1 **Table 3.** Mean, median and 25-75th percentile trace element concentrations (ng m<sup>-3</sup>)  
 2 for PM<sub>10-2.5</sub>, PM<sub>2.5-1.0</sub> and PM<sub>1.0-0.3</sub> at MR, NK and DE.

Marylebone Road												
Element	PM <sub>10-2.5</sub>				PM <sub>2.5-1.0</sub>				PM <sub>1.0-0.3</sub>			
	mean	median	25th perc	75th perc	mean	median	25th perc	75th perc	mean	median	25th perc	75th perc
<b>Na</b>	926.6	866.2	454.2	1319.9	122.0	85.5	53.8	159.7	27.3	15.7	10.6	27.8
<b>Mg</b>	105.4	96.4	66.2	136.5	25.4	19.7	13.6	34.4	8.4	7.1	5.0	9.7
<b>Al</b>	84.2	68.0	45.9	105.1	22.9	20.5	15.3	28.0	5.9	5.5	3.7	7.3
<b>Si</b>	184.4	142.6	87.2	237.0	55.4	44.2	25.6	71.6	14.7	12.1	7.3	18.7
<b>P</b>	16.3	14.5	9.9	20.8	6.7	6.0	3.9	8.9	4.8	3.7	2.5	6.5
<b>S</b>	125.1	110.9	78.8	154.4	64.3	53.7	38.4	81.2	196.1	83.0	37.6	285.9
<b>Cl</b>	989.5	862.8	366.4	1457.3	296.2	149.9	41.7	448.3	115.0	35.7	7.2	146.5
<b>K</b>	42.9	38.4	27.4	52.1	16.3	14.0	9.4	21.5	17.8	11.9	8.0	23.2
<b>Ca</b>	233.4	176.2	108.2	307.0	74.2	52.5	31.9	94.9	20.3	15.0	9.0	25.1
<b>Ti</b>	7.5	5.9	3.4	10.0	2.6	2.0	1.2	3.6	0.8	0.7	0.4	1.1
<b>V</b>	2.2	1.9	1.1	2.9	0.9	0.8	0.4	1.1	0.4	0.4	0.2	0.6
<b>Cr</b>	6.3	3.6	2.0	6.0	1.7	1.4	0.9	2.4	0.6	0.4	0.3	0.7
<b>Mn</b>	9.4	7.7	4.6	12.2	3.4	2.9	2.0	4.4	1.4	1.0	0.6	1.7
<b>Fe</b>	693.1	601.7	347.0	929.9	259.9	226.8	136.4	348.6	90.4	75.8	43.6	122.3
<b>Ni</b>	2.1	0.6	0.4	1.0	0.3	0.2	0.1	0.4	0.2	0.1	0.1	0.2
<b>Cu</b>	26.0	22.9	12.6	33.3	9.5	8.2	4.6	12.5	3.3	2.6	1.4	4.5
<b>Zn</b>	10.9	8.9	5.2	14.1	4.3	3.6	2.0	5.6	4.6	3.0	1.6	6.5
<b>Br</b>	2.3	1.8	1.0	3.0	0.8	0.6	0.4	1.0	1.7	1.1	0.6	2.3
<b>Sr</b>	1.1	0.9	0.7	1.4	0.4	0.4	0.2	0.6	0.2	0.1	0.1	0.2
<b>Zr</b>	2.5	1.8	0.9	3.3	1.1	0.8	0.4	1.4	0.4	0.2	0.1	0.5
<b>Mo</b>	3.1	2.2	1.1	3.9	1.3	1.0	0.6	1.6	0.5	0.4	0.2	0.6
<b>Sn</b>	4.1	3.3	1.9	5.5	1.7	1.5	0.8	2.3	0.7	0.6	0.3	1.0
<b>Sb</b>	3.3	2.5	1.3	4.4	1.3	1.0	0.6	1.8	0.5	0.4	0.3	0.7
<b>Ba</b>	18.3	14.5	8.3	24.7	7.6	6.5	3.9	10.3	2.7	2.1	1.2	3.7
<b>Pb</b>	1.6	0.9	0.6	1.7	0.7	0.5	0.3	0.9	1.6	0.8	0.4	2.1

North Kensington												
Element	PM <sub>10-2.5</sub>				PM <sub>2.5-1.0</sub>				PM <sub>1.0-0.3</sub>			
	mean	median	25th perc	75th perc	mean	median	25th perc	75th perc	mean	median	25th perc	75th perc
Na	603.5	518.8	273.4	910.6	123.9	87.4	56.6	164.2	28.4	14.1	9.8	31.4
Mg	57.7	50.3	30.5	84.6	23.1	18.0	12.7	31.0	7.2	5.3	3.1	9.0
Al	31.5	26.6	16.7	41.7	16.9	15.4	10.1	20.5	4.5	3.9	2.8	5.5
Si	61.2	49.7	24.9	76.3	33.5	26.8	14.9	45.5	8.2	5.8	3.4	10.0
P	6.5	5.6	3.3	9.0	4.2	3.7	2.3	5.3	3.3	2.3	1.4	4.1
S	63.5	56.4	38.2	85.6	53.9	43.0	30.3	65.9	174.8	82.0	37.9	211.5
Cl	545.2	429.4	138.4	879.0	271.3	107.8	24.8	394.8	90.2	14.0	3.5	94.3
K	22.3	19.8	12.8	30.7	14.2	12.2	8.3	19.9	15.4	10.2	6.2	18.7
Ca	92.4	70.2	40.5	114.5	49.9	37.2	21.0	59.9	11.8	8.6	4.9	14.1
Ti	2.7	1.7	0.9	3.2	1.6	1.2	0.5	2.3	0.4	0.3	0.1	0.5
V	0.6	0.4	0.2	0.7	0.4	0.3	0.1	0.5	0.2	0.2	0.1	0.3
Cr	1.2	0.8	0.4	1.5	0.6	0.5	0.3	0.8	0.2	0.1	0.0	0.2
Mn	2.4	1.7	1.0	3.0	1.7	1.5	0.8	2.2	0.8	0.5	0.1	0.9
Fe	163.8	120.8	69.9	202.6	98.8	72.7	39.0	126.0	30.1	18.5	9.6	34.8
Ni	0.4	0.2	0.1	0.4	0.1	0.1	0.0	0.2	0.1	0.1	0.0	0.1
Cu	4.9	3.6	1.8	6.4	3.7	2.5	1.4	4.6	1.2	0.6	0.4	1.4
Zn	2.9	1.9	1.0	3.4	2.1	1.5	0.8	2.8	3.2	1.9	0.8	4.3
Br	1.3	1.0	0.4	1.8	0.7	0.5	0.3	1.0	1.6	1.1	0.5	1.9
Sr	0.5	0.4	0.2	0.6	0.3	0.2	0.2	0.4	0.1	0.1	0.0	0.1
Zr	0.5	0.2	0.1	0.4	0.3	0.2	0.1	0.4	0.1	0.1	0.0	0.1
Mo	0.8	0.3	0.2	0.7	0.5	0.3	0.1	0.6	0.2	0.1	0.1	0.2
Sn	0.7	0.5	0.2	0.9	0.5	0.4	0.2	0.7	0.3	0.2	0.1	0.3
Sb	0.5	0.3	0.2	0.6	0.4	0.2	0.1	0.5	0.2	0.2	0.1	0.3
Ba	4.3	2.1	1.2	4.5	2.7	1.8	0.9	3.5	1.0	0.6	0.3	1.2
Pb	0.4	0.2	0.1	0.4	0.4	0.2	0.1	0.6	1.4	0.7	0.3	1.8

Detling Element	PM <sub>10-2.5</sub>				PM <sub>2.5-1.0</sub>				PM <sub>1.0-0.3</sub>			
	mean	median	25th perc	75th perc	mean	median	25th perc	75th perc	mean	median	25th perc	75th perc
Na	275.8	197.5	17.4	443.1	66.4	37.4	13.0	82.4	21.1	11.3	5.0	28.1
Mg	27.7	21.0	5.2	40.2	12.4	8.8	2.7	17.1	6.3	4.5	1.7	7.9
Al	16.0	14.7	7.6	22.0	13.2	12.8	6.6	18.2	3.3	3.2	1.5	4.8
Si	31.5	25.5	13.4	40.3	17.6	13.8	6.2	25.6	5.4	4.2	2.4	7.8
P	3.1	2.5	1.1	4.2	2.0	1.6	0.8	2.7	3.2	1.6	0.9	4.1
S	36.2	31.7	6.8	48.0	33.3	30.5	13.1	47.9	224.1	59.8	27.8	242.8
Cl	237.3	50.8	3.6	380.1	135.0	9.2	2.6	148.4	64.3	10.3	3.4	57.2
K	13.8	11.8	3.5	17.7	8.2	7.5	2.6	12.5	19.9	8.2	3.6	19.8
Ca	37.5	28.8	11.1	46.6	20.0	14.7	5.9	25.1	8.2	4.9	2.7	8.3
Ti	1.0	0.6	0.3	1.3	0.7	0.4	0.2	1.0	0.2	0.2	0.1	0.3
V	0.2	0.1	0.1	0.2	0.1	0.1	0.1	0.2	0.2	0.1	0.0	0.3
Cr	4.0	0.9	0.3	2.9	0.8	0.3	0.2	0.6	0.1	0.1	0.0	0.2
Mn	1.8	0.6	0.3	1.3	1.1	1.2	0.3	1.6	0.7	0.3	0.0	0.7
Fe	55.2	36.8	19.9	66.2	26.8	21.5	11.5	37.7	9.8	7.8	4.3	13.3
Ni	4.3	0.7	0.2	2.6	0.6	0.1	0.1	0.3	0.9	0.1	0.0	0.5
Cu	1.4	0.8	0.4	1.8	0.9	0.7	0.4	1.1	0.7	0.3	0.1	0.5
Zn	3.4	0.9	0.4	1.8	1.3	0.7	0.3	1.7	4.3	1.6	0.6	5.7
Br	1.1	0.4	0.1	1.3	0.4	0.2	0.1	0.5	1.9	1.1	0.5	2.4
Sr	0.2	0.2	0.1	0.3	0.1	0.1	0.0	0.2	0.1	0.0	0.0	0.1
Zr	0.0	0.0	-0.1	0.1	0.1	0.0	0.0	0.1	0.0	0.0	0.0	0.0
Mo	1.9	0.1	0.1	0.7	0.2	0.1	0.0	0.2	0.1	0.1	0.0	0.1
Sn	0.3	0.1	0.0	0.2	0.2	0.1	0.1	0.2	0.2	0.1	0.1	0.3
Sb	0.2	0.1	0.0	0.2	0.1	0.1	0.0	0.1	0.2	0.1	0.0	0.2
Ba	1.0	0.4	0.2	0.8	0.5	0.4	0.2	0.7	0.3	0.2	0.1	0.4
Pb	0.3	0.1	0.0	0.3	0.3	0.1	0.1	0.5	1.6	0.5	0.2	1.8

1

2

1 **Figure captions**

2

3 **Figure 1.** Map of south eastern UK. Indicated are the sampling sites MR (kerbside  
4 site Marylebone Road), NK (urban background site North Kensington), DE (rural site  
5 Detling), and the elevated BT Tower site for meteorological measurements (adapted  
6 from Google Maps).

7

8 **Figure 2.** Relative contribution for trace elements in  $PM_{10-2.5}$ ,  $PM_{2.5-1.0}$  and  $PM_{1.0-0.3}$  to  
9 total  $PM_{10}$  mean concentration per element at MR (top), NK (middle) and DE  
10 (bottom). Absolute mean total  $PM_{10}$  element concentrations are shown above each  
11 bar.

12

13 **Figure 3.** Mean, median and 25-75th percentile urban increment values for trace  
14 elements at NK relative to DE for  $PM_{10-2.5}$  (top),  $PM_{2.5-1.0}$  (middle) and  $PM_{1.0-0.3}$   
15 (bottom). Note that the median of Zr in  $PM_{10-2.5}$  is below detection limit.

16

17 **Figure 4.** Mean, median and 25-75th percentile trace element concentrations at MR  
18 split in four wind direction sectors (N, E, S, W) normalized to the global median  
19 concentration per element for  $PM_{10-2.5}$  (top),  $PM_{2.5-1.0}$  (middle) and  $PM_{1.0-0.3}$  (bottom).  
20 See Sect. 4.2.2 for the definition of the wind direction sectors.

21

22 **Figure 5.** Mean, median and 25-75th percentile kerb increment values for trace  
23 elements at MR relative to NK for  $PM_{10-2.5}$  (top),  $PM_{2.5-1.0}$  (middle) and  $PM_{1.0-0.3}$   
24 (bottom) split in SW and NE wind sectors. See Sect. 4.2.2 for the definition of the  
25 wind direction sectors.

26

27 **Figure 6.** Diurnal cycles of 2 h median concentrations of Na, Si, S, Fe and Sb for  
28  $PM_{10-2.5}$  (left),  $PM_{2.5-1.0}$  (middle) and  $PM_{1.0-0.3}$  (right) at MR, NK, DE split in SW and NE  
29 wind sectors. See Sect. 4.2.2 for the definition of the wind direction sectors. Hour of  
30 day is start of 2 h sampling period, so 00:00 LT means sampling from 00:00 to 02:00  
31 LT.

32

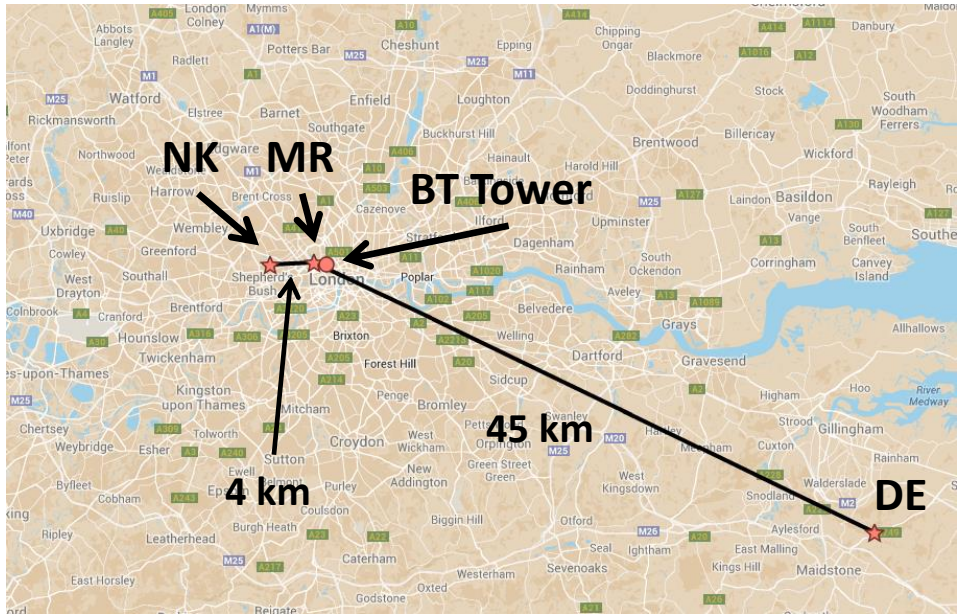
33 **Figure 7.** Weekly cycles of 2 h median concentrations of Na, Si, S, Fe and Sb for  
34  $PM_{10-2.5}$  (left),  $PM_{2.5-1.0}$  (middle) and  $PM_{1.0-0.3}$  (right) at MR, NK, DE.

35

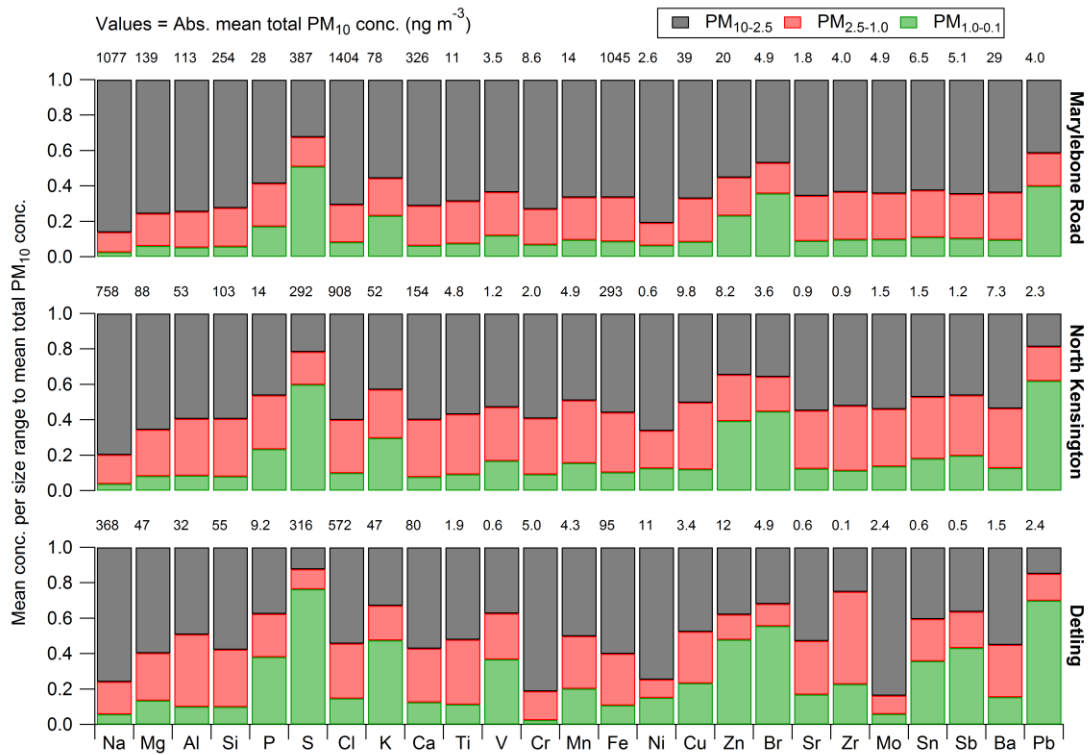
1 **Figure 8.** (top) Diurnal (left) and weekly (right) cycles of traffic flow at MR, (middle  
2 and bottom left) diurnal cycles of 2 h median  $\text{NO}_x$  and total  $\text{PM}_{10}$  mass  
3 concentrations at MR, NK and DE split in SW and NE wind sectors, and (middle and  
4 bottom right) weekly cycles of 2 h median  $\text{NO}_x$  and total  $\text{PM}_{10}$  mass concentrations at  
5 MR, NK and DE. See Sect. 4.2.2 for the definition of the wind direction sectors. Time  
6 stamp is start of 2 h averaging period, so 00:00 LT means averaging between 00:00  
7 and 02:00 LT.

8  
9 **Figure 9.** (top panel) Time series of (top left axis)  $\text{PM}_{1.0-0.3}$  S, K, Zn and Pb  
10 concentrations at NK and (top right axis) wind direction from BT Tower, time series of  
11 (bottom left axis)  $\text{PM}_{10-2.5}$  Na, Si, S and Sb concentrations at NK and (bottom right  
12 axis) total  $\text{PM}_{10}$  mass concentration at NK; (bottom panel) three NK footprints  
13 simulated with the NAME model corresponding to the vertical lines (A, B, C) indicated  
14 in the top panel. Trajectories are simulated for particles released from NK and  
15 followed back at 0-100 m a.g.l. for the previous 24 h at: **(A)** 23 January 2012 09:00  
16 LT, **(B)** 31 January 2012 21:00 LT, **(C)** 6 February 2012 18:00 LT; particle  
17 concentrations increase from blue to red.

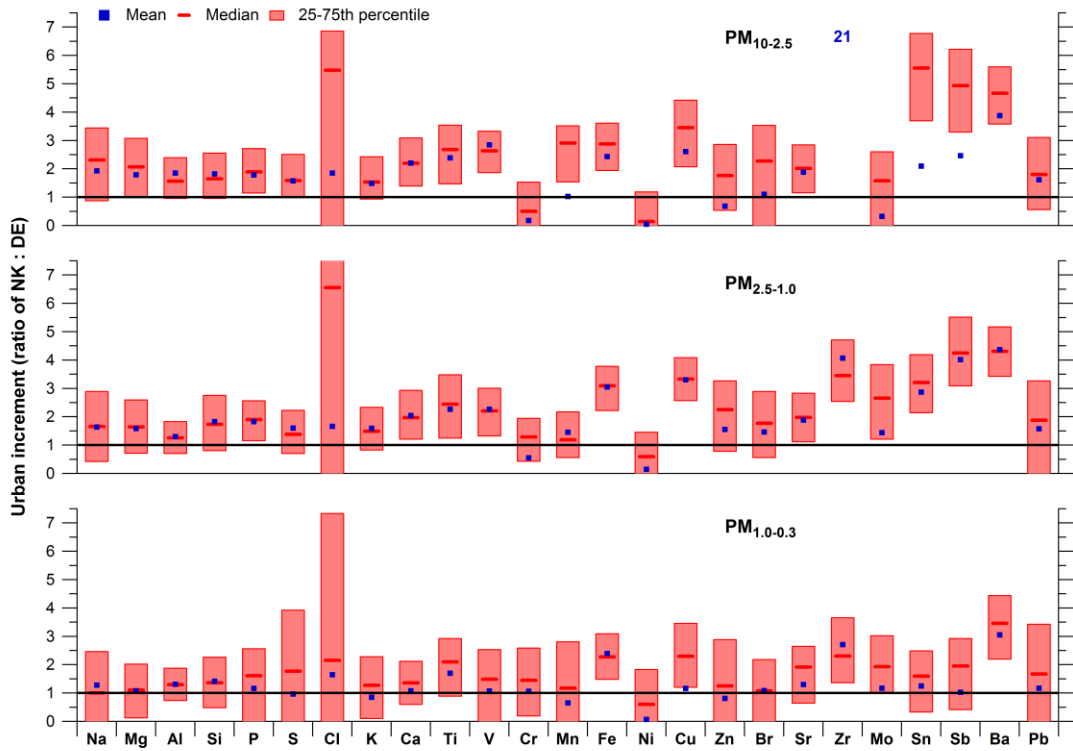
18  
19



1  
2 **Figure 1.** Map of south eastern UK. Indicated are the sampling sites MR (kerbside  
3 site Marylebone Road), NK (urban background site North Kensington), DE (rural site  
4 Detling), and the elevated BT Tower site for meteorological measurements (adapted  
5 from Google Maps).  
6



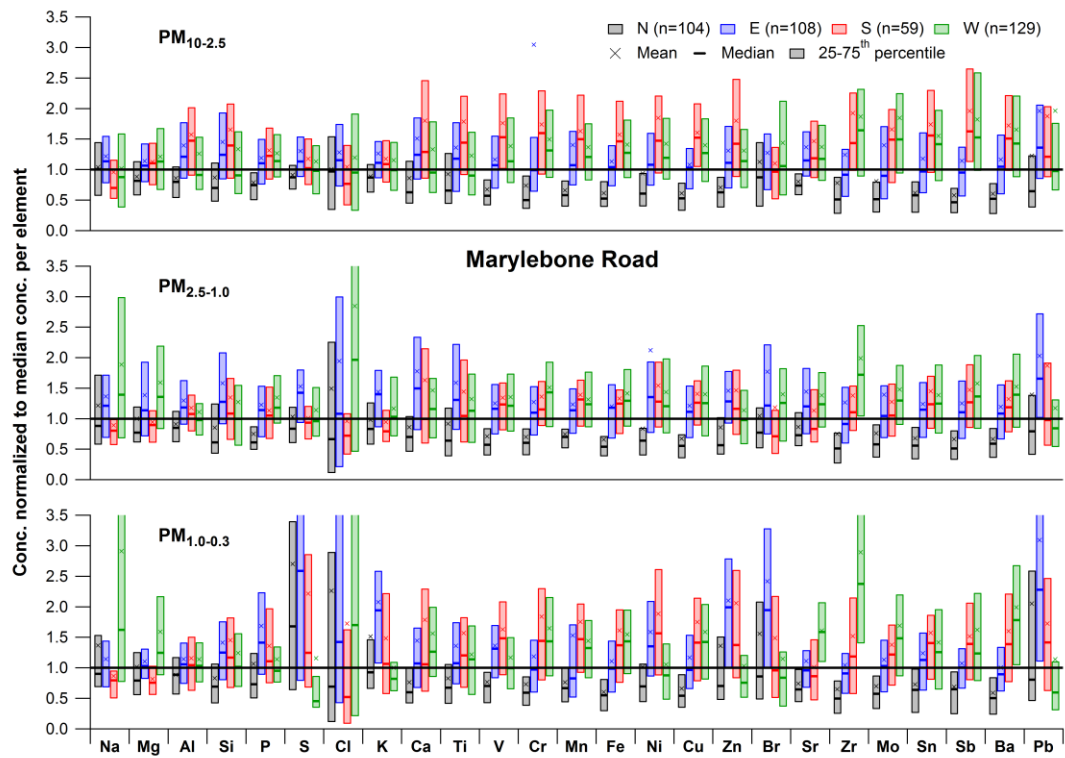
1  
 2 **Figure 2.** Relative contribution for trace elements in PM<sub>10-2.5</sub>, PM<sub>2.5-1.0</sub> and PM<sub>1.0-0.3</sub> to  
 3 total PM<sub>10</sub> mean concentration per element at MR (top), NK (middle) and DE  
 4 (bottom). Absolute mean total PM<sub>10</sub> element concentrations are shown above each  
 5 bar.  
 6



1  
2  
3  
4  
5

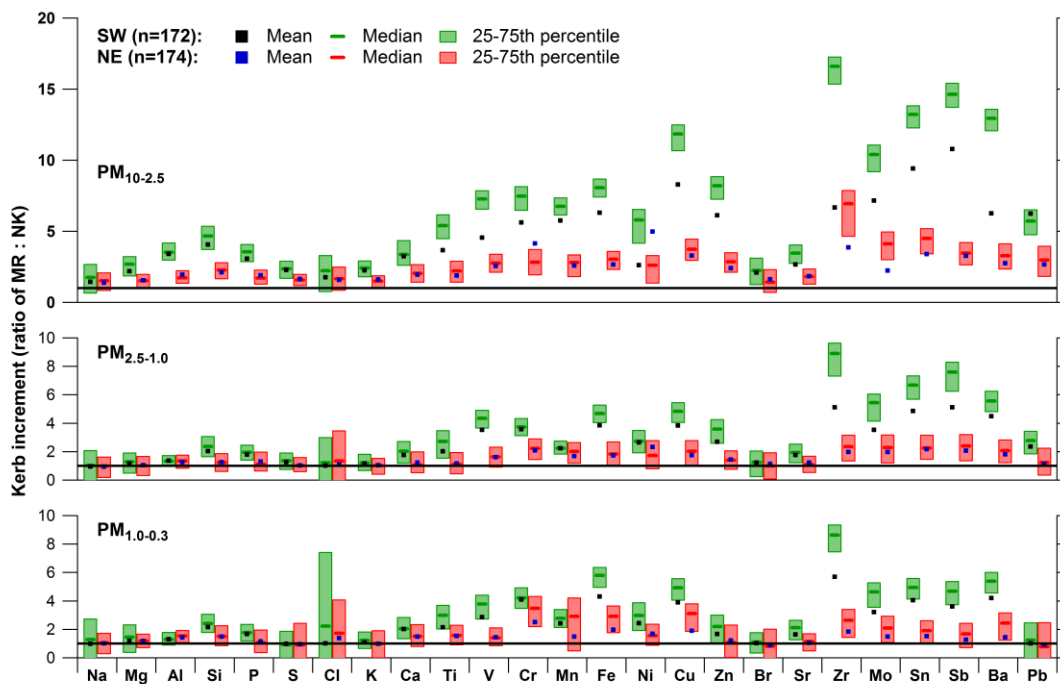
**Figure 3.** Mean, median and 25-75th percentile urban increment values for trace elements at NK relative to DE for PM<sub>10-2.5</sub> (top), PM<sub>2.5-1.0</sub> (middle) and PM<sub>1.0-0.3</sub> (bottom). Note that the median of Zr in PM<sub>10-2.5</sub> is below detection limit.





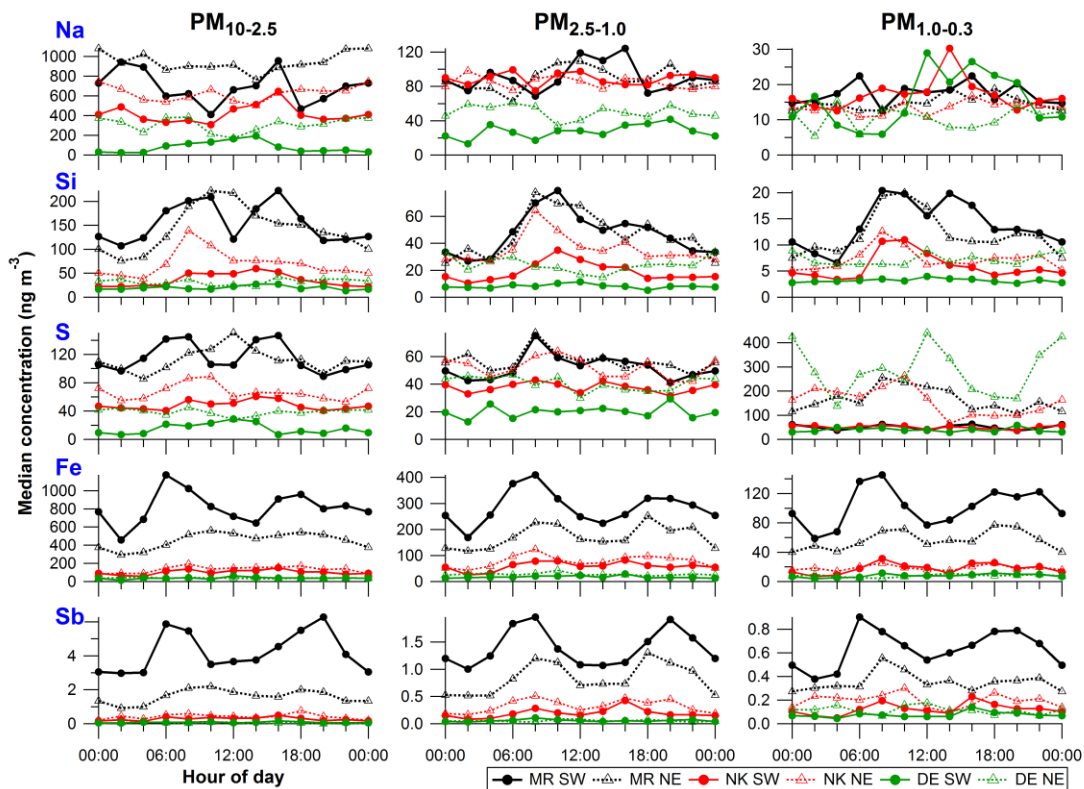
1  
2  
3  
4  
5  
6

**Figure 4.** Mean, median and 25-75th percentile trace element concentrations at MR split in four wind direction sectors (N, E, S, W) normalized to the global median concentration per element for  $PM_{10-2.5}$  (top),  $PM_{2.5-1.0}$  (middle) and  $PM_{1.0-0.3}$  (bottom). See Sect. 4.2.2 for the definition of the wind direction sectors.



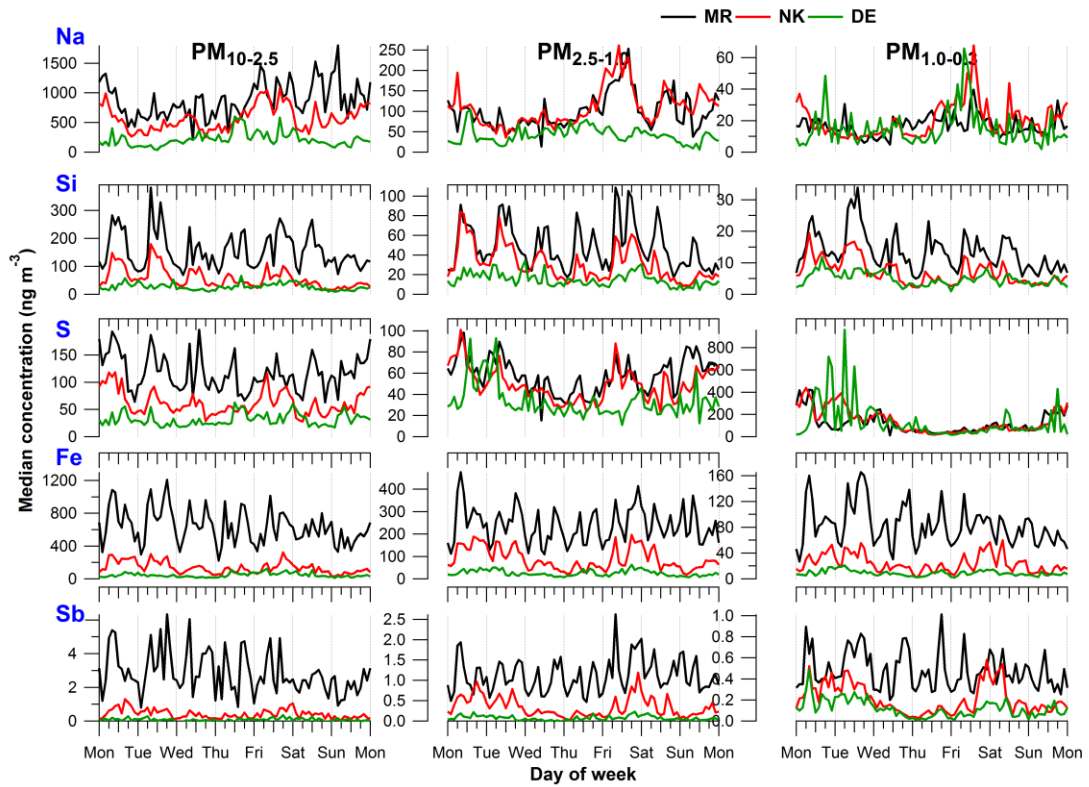
1  
2  
3  
4  
5  
6

**Figure 5.** Mean, median and 25-75th percentile kerb increment values for trace elements at MR relative to NK for  $PM_{10-2.5}$  (top),  $PM_{2.5-1.0}$  (middle) and  $PM_{1.0-0.3}$  (bottom) split in SW and NE wind sectors. See Sect. 4.2.2 for the definition of the wind direction sectors.



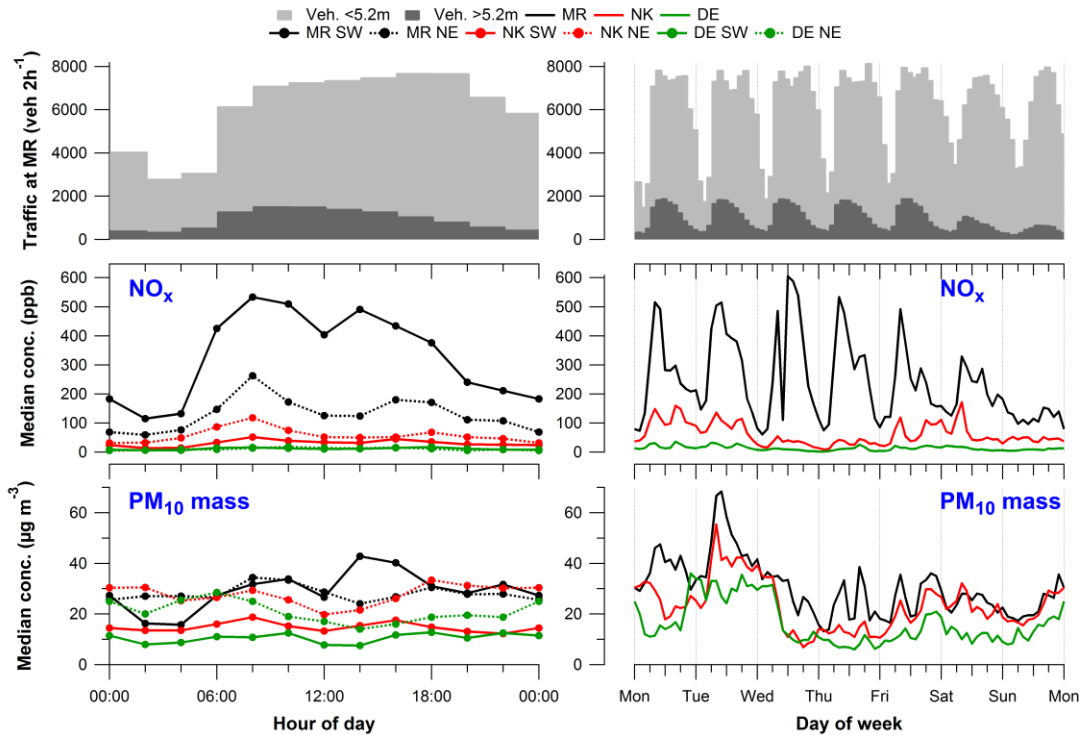
1  
2  
3  
4  
5  
6  
7

**Figure 6.** Diurnal cycles of 2 h median concentrations of Na, Si, S, Fe and Sb for  $PM_{10-2.5}$  (left),  $PM_{2.5-1.0}$  (middle) and  $PM_{1.0-0.3}$  (right) at MR, NK, DE split in SW and NE wind sectors. See Sect. 4.2.2 for the definition of the wind direction sectors. Hour of day is start of 2 h sampling period, so 00:00 LT means sampling from 00:00 to 02:00 LT.



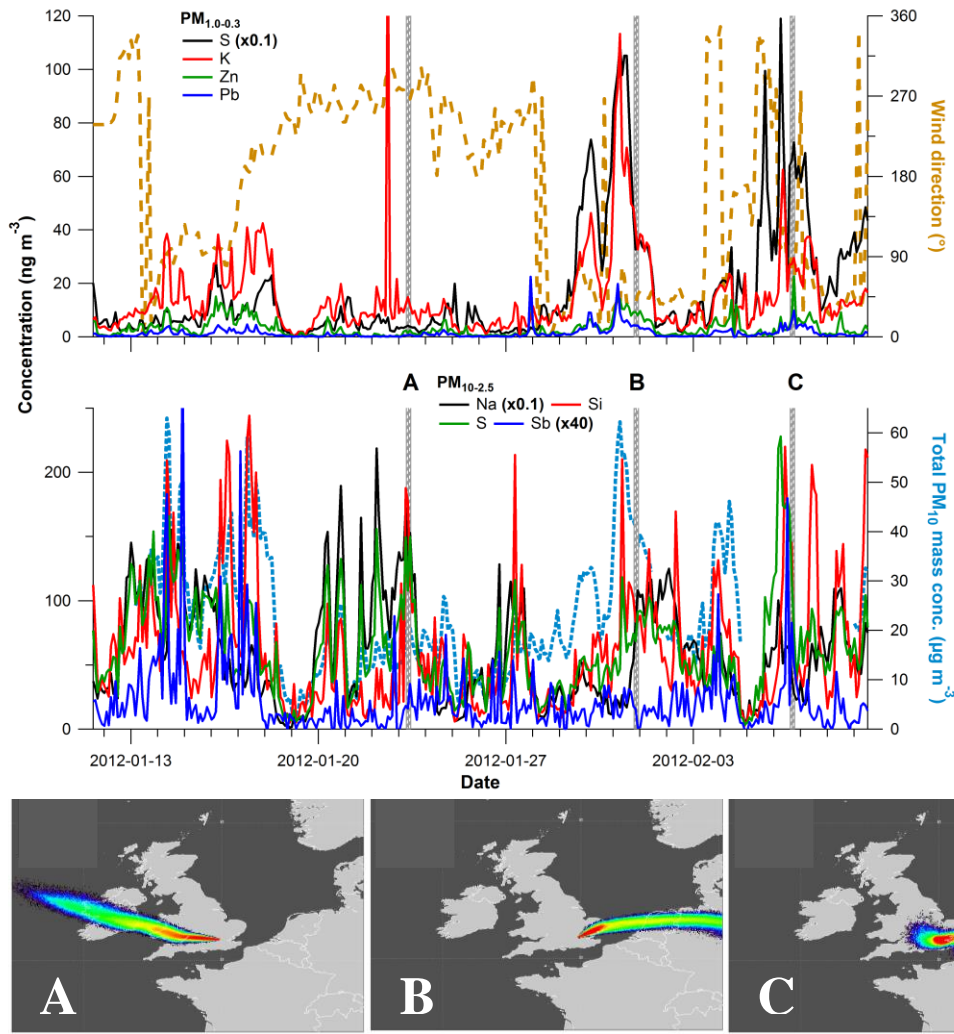
1  
2  
3  
4

**Figure 7.** Weekly cycles of 2 h median concentrations of Na, Si, S, Fe and Sb for PM<sub>10-2.5</sub> (left), PM<sub>2.5-1.0</sub> (middle) and PM<sub>1.0-0.3</sub> (right) at MR, NK, DE.



1  
2  
3  
4  
5  
6  
7  
8  
9

**Figure 8.** (top) Diurnal (left) and weekly (right) cycles of traffic flow at MR, (middle and bottom left) diurnal cycles of 2 h median NO<sub>x</sub> and total PM<sub>10</sub> mass concentrations at MR, NK and DE split in SW and NE wind sectors, and (middle and bottom right) weekly cycles of 2 h median NO<sub>x</sub> and total PM<sub>10</sub> mass concentrations at MR, NK and DE. See Sect. 4.2.2 for the definition of the wind direction sectors. Time stamp is start of 2 h averaging period, so 00:00 LT means averaging between 00:00 and 02:00 LT.



1  
2 **Figure 9.** (top panel) Time series of (top left axis)  $PM_{1.0-0.3}$  S, K, Zn and Pb  
3 concentrations at NK and (top right axis) wind direction from BT Tower, time series of  
4 (bottom left axis)  $PM_{10-2.5}$  Na, Si, S and Sb concentrations at NK and (bottom right  
5 axis) total  $PM_{10}$  mass concentration at NK; (bottom panel) three NK footprints  
6 simulated with the NAME model corresponding to the vertical lines (A, B, C) indicated  
7 in the top panel. Trajectories are simulated for particles released from NK and  
8 followed back at 0-100 m a.g.l. for the previous 24 h at: **(A)** 23 January 2012 09:00  
9 LT, **(B)** 31 January 2012 21:00 LT, **(C)** 6 February 2012 18:00 LT; particle  
10 concentrations increase from blue to red.  
11

## 1 Supplement A: RDI backup filter and PM<sub>1.0</sub> cut off analysis

### 2 RDI backup filter analysis

3 RDI backup filters (Balston 050-11-BQ 2 µm, microfiber, fluorocarbon resin binder)  
4 from the ClearLo winter campaign were immersed in water and sonicated for about  
5 1.5 h. One filter per measurement site was available. Total sulphate (SO<sub>4</sub><sup>2-</sup>) mass  
6 was obtained by analysing the solutions with ion chromatography and converted to  
7 concentrations by dividing by the total air volume that passed through the filter during  
8 the campaign.

9 Table S1 compares the S concentrations from the RDI PM<sub>1.0-0.3</sub> stage with S (from  
10 SO<sub>4</sub><sup>2-</sup>) collected by the backup filter. The sum of both (Total S < 1 µm) is compared  
11 with S from AMS sulphate measurements. The ratio in the last column reveals mass-  
12 closure between the RDI and AMS within 25 %.

13

14 **Table S1.** Comparison between S from RDI PM<sub>1.0-0.3</sub> fractions and backup filters (S from  
15 SO<sub>4</sub><sup>2-</sup>) with S from the AMS (S from SO<sub>4</sub><sup>2-</sup>). Units in ng m<sup>-3</sup>. The ratio of S in the RDI to the  
16 AMS is given in the last column (ratio of RDI Total S < 1 µm to AMS S).

	RDI			AMS	Ratio
Site	PM <sub>1.0-0.3</sub> S	S in backup filter	Total S <1 µm	S	RDI : AMS
MR	195	398	593	476	1.25
NK	174	405	579	607	0.95
DE	224	359	583	715	0.82

17

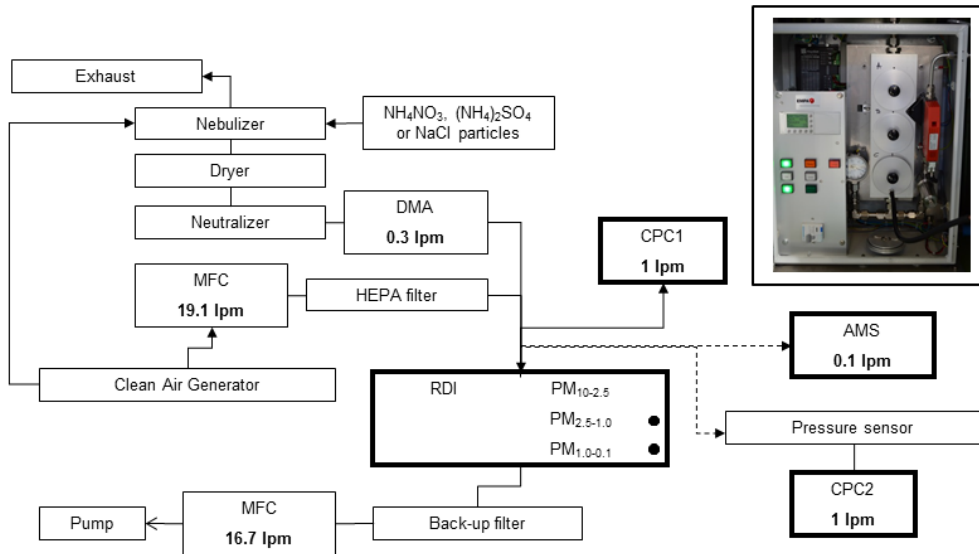
18

### 19 RDI PM<sub>1.0</sub> cut off analysis

20 As noted in the main text and in Supplement C, elements whose mass is dominated  
21 by the PM<sub>1.0</sub> fraction are typically underestimated by RDI-SR-XRF relative to external  
22 measurements like the AMS and 24 h filter measurements. One explanation is that  
23 the collection efficiency of the RDI PM<sub>1.0</sub> stage is smaller than expected, e.g. by a  
24 larger-than-expected size cut off. We therefore performed new laboratory  
25 measurements of the RDI size-dependent collection efficiency, and compare these to  
26 earlier characterisations by Bukowiecki et al. (2009c) and Richard et al. (2010).

27 Figure S1 shows the setup used for the collection efficiency measurements.  
28 (NH<sub>4</sub>)<sub>2</sub>SO<sub>4</sub>, NH<sub>4</sub>NO<sub>3</sub> and NaCl particles were nebulized, dried and size-selected  
29 using a differential mobility analyser (DMA, TSI, Inc., Shoreview, MN, USA), and then  
30 sampled with the RDI. The DMA was operated with sample and sheath flow rates of  
31 0.3 and 3.0 L min<sup>-1</sup>, respectively. A condensation particle counter (CPC1, TSI, Inc.,  
32 Shoreview, MN, USA) with a flow rate of 1.0 L min<sup>-1</sup> was continuously connected at  
33 the inlet stage of the RDI to measure the particles entering the RDI, and to correct for  
34 fluctuations in nebulizer performance. A second line led to an additional CPC (CPC2,  
35 1 L min<sup>-1</sup>) and an Aerodyne aerosol mass spectrometer (AMS, Aerodyne Research,  
36 Inc., Billerica, MA, USA) with a flow rate of 0.1 L min<sup>-1</sup>. This line could be connected  
37 at the inlet, after the PM<sub>2.5-1.0</sub> (B) stage or after the PM<sub>1.0-0.3</sub> (C) stage. Measurements  
38 following the B and C stages were made by connecting the line to a small hole in the  
39 lid covering these stages, resulting in sampling of the air flow at a 90° angle (see  
40 picture in Figure S1). The total flow through the system was controlled by a mass  
41 flow controller connected to a clean air generator pumping air into the nebulizer and  
42 RDI simultaneously. The RDI was operated using three wheels with freshly mounted

1 6  $\mu\text{m}$  polypropylene foils coated with Apiezon to minimize particle bouncing effects,  
 2 to simulate ambient field measurements. Tests ruled out differences in  
 3 measurements on the top or bottom side of the lid at the B and C stages. For the final  
 4 results, all data was collected at the bottom side of the B and C stages.



5  
 6 **Figure S1.** Setup of the collection efficiency measurements of the RDI  $\text{PM}_{1.0}$  impactor stage.  
 7 The line with the AMS and CPC2 was connected at the inlet, after the  $\text{PM}_{2.5-1.0}$  or after the  
 8  $\text{PM}_{1.0-0.3}$  stage. The picture of the RDI shows the connection at the bottom side of the lid of the  
 9  $\text{PM}_{1.0-0.3}$  stage.

10  
 11 As noted above, measurements were conducted at the RDI inlet, after the B stage  
 12 impactor (nominal size cut =  $1.0 \mu\text{m}$ ) and after the C stage impactor (nominal size cut  
 13 =  $0.1 \mu\text{m}$ ). RDI collection efficiency at each stage is defined as 1 minus transmission.  
 14 To correct for fluctuations in nebulizer concentrations, all data for a given set of  
 15 CPC2/AMS measurements were normalized to a constant inlet (CPC1)  
 16 concentration. Transmission from the inlet across the B stage impactor was between  
 17 90 and 100 % for all sizes (aerodynamic diameter  $d < 950 \text{ nm}$ ), indicating negligible  
 18 particle losses and/or unintended collection of small particles. C stage collection  
 19 efficiency ( $\text{CE}_C$ ) was therefore calculated using Eq. (S1):

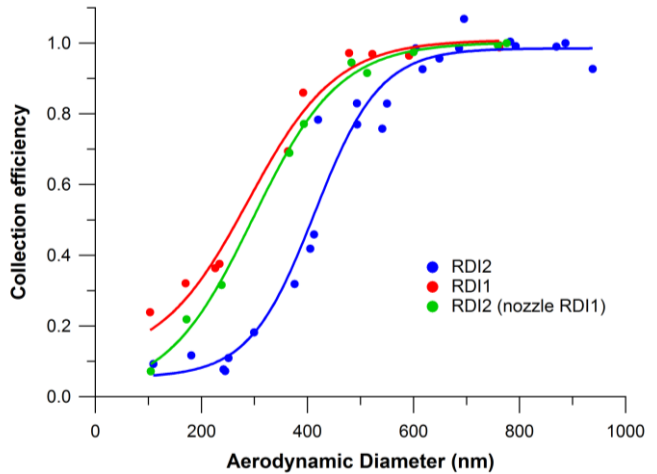
$$20 \quad \text{CE}_C = 1 - \left( \text{Conc}_C * \frac{\text{CPC1}_{ref}}{\text{CPC1}_{measC}} \right) / \left( \text{Conc}_B * \frac{\text{CPC1}_{ref}}{\text{CPC1}_{measB}} \right) \quad (\text{S1})$$

21 Concentrations were measured using both CPC2 and the AMS. For large particles,  
 22 where the fraction of multiple charged particles passed by the DMA is negligible,  
 23 these two methods yield similar results. For smaller particles, collection efficiency as  
 24 calculated by the CPC2 is biased low due to the presence of multiple charged  
 25 particles with larger diameters, as clearly evidenced from AMS size distributions. For  
 26 simplicity, we therefore present only the AMS results here. RDI collection efficiencies  
 27 are calculated by fitting a lognormal distribution to each mode and using the resulting  
 28 mass concentrations in Eq. S1. This allows simultaneous calculation of RDI collection  
 29 efficiencies for several sizes, providing an internal consistency and stability check for  
 30 the measurements.

31



1 Figure S2 shows the collection efficiency of the  $PM_{1.0-0.3}$  (C stage) nozzle for two  
 2 RDIs (RDI1 and RDI2) as a function of  $d$  for  $NH_4NO_3$  particles.  $D$  is calculated from  
 3 AMS size measurements, assuming a density of 1.74 and a Jayne shape factor  
 4 (DeCarlo et al., 2004) of 0.8. Cut points are estimated by a sigmoidal fit to the  
 5 collection efficiency curves, and yield different cut points for the two RDIs. RDI1 has  
 6 a cut point of  $290 \pm 25$  nm and RDI2 a cut point of  $410 \pm 15$  nm. This discrepancy  
 7 was investigated using RDI2 equipped with the  $PM_{1.0-0.3}$  nozzle of RDI1 (RDI2 (nozzle  
 8 RDI1)), demonstrating that the difference between the two RDIs is governed by  
 9 nozzle performance, because the cut point of this system is  $300 \pm 20$  nm and  
 10 therefore closer to the RDI1 performance. Similar cut points for the various systems  
 11 were obtained using  $(NH_4)_2SO_4$  and NaCl particles (not shown).



12  
 13  
 14 **Figure S2.** Collection efficiency of the RDI  $PM_{1.0-0.3}$  impactor stage as a function of  
 15 aerodynamic diameter.  
 16

17 Measurements of the nozzle sizes under a microscope reveal small differences  
 18 between the RDIs. A  $1.0 \mu m$  cut point at the B stage impactor is obtained with a  
 19 nozzle size of  $0.68 \times 10$  mm. The RDI1 and RDI2 B stage nozzles were  $0.70 \times 10$   
 20 mm, and a third RDI that was used at Marylebone Road during ClearLo had a size of  
 21  $0.71 \times 10$  mm. The C stage nozzle size should measure  $0.30 \times 10$  mm for a cut point  
 22 of  $0.1 \mu m$ . However, the nozzle sizes were  $0.30-0.31 \times 10$ ,  $0.30-0.32 \times 10$  and  $0.32 \times$   
 23  $10$  for RDI1, RDI2 and the third RDI, respectively. We expect the deviations from  
 24 these measurements from the machining of the nozzles, resulting in higher cut points  
 25 than expected for the  $PM_{1.0}$  stage, and possibly also for the  $PM_{2.5-1.0}$  stage.

26  
 27 **Conclusions**

28 The  $PM_{1.0-0.3}$  collection efficiency curves are different for the two RDIs. RDI2 has a  
 29 larger small-end cut point of  $410 \pm 15$  nm than RDI1 of  $290 \pm 25$  nm. RDI2 with the  
 30  $PM_{1.0-0.3}$  nozzle of RDI1 resulted in a similar cut point of RDI1 of  $300 \pm 20$  nm. The  
 31 slightly larger nozzles than theoretically calculated are the likely reason for the  
 32 observed increase in the small-end cut point of the  $PM_{1.0-0.3}$  nozzle and thus in  
 33 reduced particle collection at the C stage.

34  
 35

## 1 Supplement B: Changes in SR-XRF analysis

2 The data described in the main text was obtained with RDI-SR-XRF analysis. The  
3 following significant changes were made in the SR-XRF analysis compared to the  
4 methodology described in Bukowiecki et al. (2005, 2008) and Richard et al. (2010):

5 1. At SLS, we replaced the silicon drift detector (Roentec Xflash 2001 type 1102,  
6 Bruker AXS) with an e2v SiriusSD detector (SiriusSD-30133LE-IS). This detector is  
7 equipped with a thin polymer window resulting in a wider energy range down to about  
8 300 eV and a better energy resolution of 133 eV (Mn K $\alpha$  at 5.9 keV). In addition, the  
9 setup accepts a higher throughput resulting in negligible dead time effects. We also  
10 replaced the helium chamber with an in-house built vacuum chamber (sample  
11 exposure system for micro-X-ray fluorescence measurements, SESmiX) which  
12 reaches about 10<sup>-6</sup> bar. This extended the measured range of elements down to Na  
13 and Mg.

14 2. Reference standards for calibration of element fluorescence counts to mass  
15 concentrations were produced on the same 6  $\mu$ m PP substrate as used for RDI  
16 sampling, in contrast to the previous standard where a much thicker 100  $\mu$ m PET foil  
17 (Folex, BG-32.5 RS plus) was used. Two standards suitable for measurements at  
18 both SLS and HASYLAB contained elements in equal concentrations, and have a  
19 similar mix of elements as the standard previously used. Two additional standards  
20 containing only specifically selected light elements were produced. One standard  
21 contained Na, Al, P and Ca; the other Mg, Si, S, K and Ca. The concentrations of  
22 these elements were increased by a factor 3.8 relative to the other two standards to  
23 improve signal-to-noise ratios in the SR-XRF calibration. Co was added to these  
24 additional standards, but in the same concentration as in the other two foils and was  
25 used as a quality check of the fabrication procedure of the four standards. The  
26 concentration difference of the light elements was taken into account before applying  
27 the relative calibration of the sample elements. The new reference standards allowed  
28 the use of identical geometry and irradiation time for RDI samples and reference  
29 standards, meaning that all SR-XRF measurements exhibit the same scattering and  
30 secondary fluorescence excitation. This reduced uncertainties in both the absolute  
31 and relative calibration of the samples.

32 3. Previously, spectra were fitted with the WinAxil software package (Canberra Inc;  
33 Van Espen et al., 1986). This rather old spectral fitting package allows little flexibility  
34 in spectrum continuum correction and peak fitting. PyMCA (Sole et al., 2007) on the  
35 other hand, is more flexible, but lacks the possibility to save uncertainty calculations  
36 in batch mode. In this study, spectra were fitted with an in-house developed software  
37 package called Spectral Analysis for Multiple Instruments – toolkit for XRF (SAMI-  
38 XRF) using the IGOR Pro software environment (Wavemetrics, Inc., Portland, OR,  
39 USA) to evaluate the data and create custom interfaces to accomplish specialized  
40 tasks. SAMI sequentially determines (1) energy calibration of the X-ray line as a  
41 function of detector channel; (2) spectrum continuum correction; (3) peak width  
42 calibration as a function of energy (assuming Gaussian peak shape and a general  
43 square root law of the full-width-half-maximum (FWHM) energy relation); and (4)  
44 peak fitting of the entire spectrum, at which stage only peak heights are fitted as a  
45 free parameter and all other parameters are fixed. Steps (1) and (3) are performed  
46 with user-selected reference peaks, and incorporates fitting of complex (multi-  
47 Gaussian) peak shapes caused by nearly complete overlapping K $\alpha$ <sub>1</sub> and K $\alpha$ <sub>2</sub> lines.  
48 Step (2) utilizes collected spectra of a blank foil as a reference for the continuum  
49 shape, and scales this reference to user-selected element-free regions of the  
50 processed spectra. Step (4) allows lines to be fitted freely or fixed to another line, e.g.

1 to the strongest line in a shell. For example, the  $K\alpha_2$  and  $K\beta$  lines can be fixed to the  
2  $K\alpha_1$  line according to the relative intensities given by Bearden (1967). In this study, all  
3 lines within an electron shell were fitted fixed to the strongest line in that shell.  
4 Additionally, Ni, Cu and Zn  $L\alpha_{1,2}$  lines were fixed to the  $K\alpha_1$  line to reduce the  
5 influence of peak overlap with Na. The ratios of  $L\alpha_{1,2}$  to  $K\alpha_1$  for Ni, Cu and Zn were  
6 determined by fitting calibration standards having these elements but low Na. Final  
7 fits were then obtained using the acquired relations, thereby reducing uncertainties in  
8 the Na concentrations due to peak overlap and improving Na quantification.  
9  
10

## 1 Supplement C: Data intercomparison

2 A short description of the data intercomparison between RDI-SR-XRF data and  
3 independent filter data is given in Sect. 3 of the main text. Here the details of this  
4 comparison are given. We compare XRF data with filter data (24 h PM<sub>10</sub> trace  
5 element data analysed with ICP-MS; roughly 9 % uncertainty at a 95 % confidence  
6 interval and calibrated with NIST standards) for 18 elements collected at MR and NK  
7 (no filter data was available at DE). For this comparison, the three size ranges of the  
8 RDI were summed up to total PM<sub>10</sub> and averaged to the filter collection period. The  
9 intercomparison results are shown in Fig. S3, and are divided into four groups to  
10 facilitate discussion. Fit coefficients and Pearson's *R* values for the intercomparison  
11 are shown in Table S2, while XRF uncertainties and detection limits are given in  
12 Table S3. For all elements, except Mn and the lightest elements, the sample  
13 inhomogeneity provides the largest source of uncertainty of maximal 20 %.  
14 Significant uncertainties of 54-35 % in Na-Si arise from corrections on self-absorption  
15 effects for the calibration standards. We assume a static size distribution of the  
16 coarse and intermediate fraction ambient samples. Therefore, no additional  
17 uncertainties arise from self-absorption corrections in the samples. RDI flow rate  
18 fluctuations are estimated at a maximum of 5 %. Absolute and relative calibration  
19 uncertainties are larger for lighter elements due to their low fluorescence yields,  
20 making them harder to detect. For Na-K these uncertainties are 13 %, for Ca-Pb only  
21 2 %. The last source of uncertainty is the energy calibration of an X-ray line as  
22 function of detector channel and shows the effect of line overlap in the detection of a  
23 specific line. The uncertainties range between 1 and 22 % for most elements, but are  
24 around 60 % for Mn due to the overlap with Fe being present in much higher  
25 concentrations (on average a factor of 55). Overall, ~~an estimate of~~ the total  
26 uncertainties are estimated at 21-30 % for most elements (46-83 % for Mn; 60-43 %  
27 for Na-Si)for the median of all data points lies between 21 and 27 % (46 % for Mn) for  
28 ~~all elements in the three size fractions~~. All RDI data points lie well above their  
29 detection limits (last column Table S3).

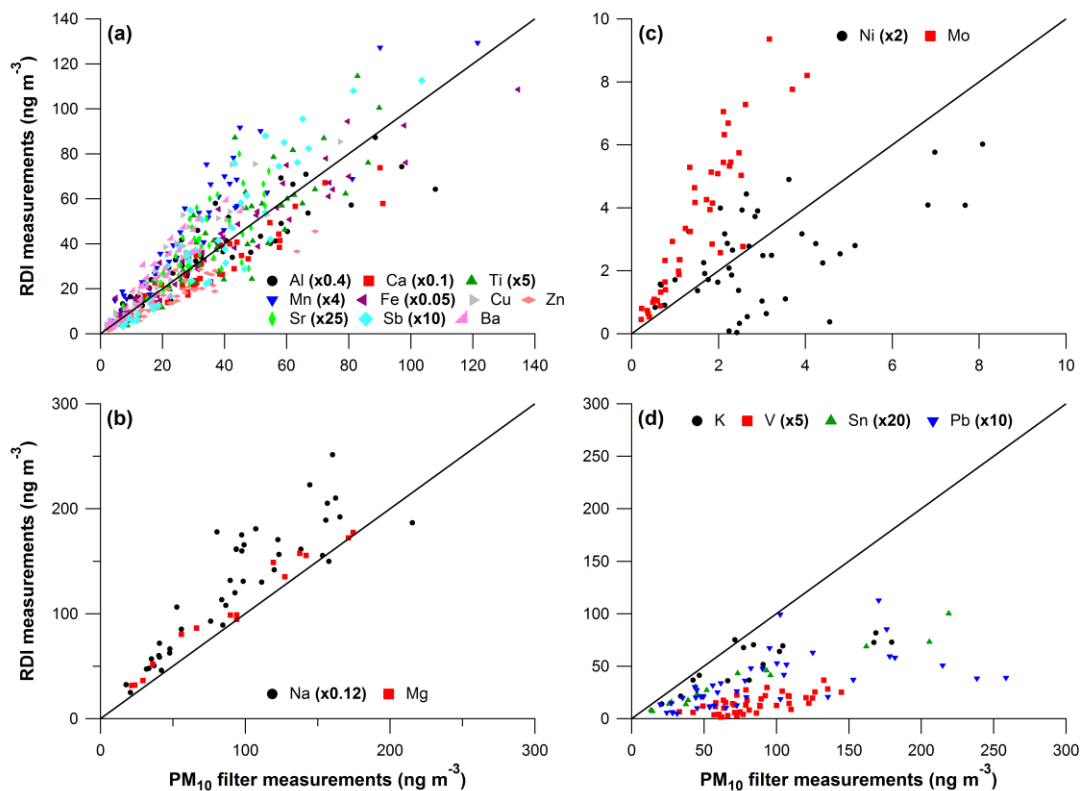
30 Elements shown in Fig. S3a (Al, Ca, Ti, Mn, Fe, Cu, Zn, Sr, Sb, Ba) agree within  
31 approximately  $\pm 50$  % with good correlations (Pearson's *R* > 0.78). Na and Mg are  
32 shown separately in Fig. S3b, because these elements are strongest affected by  
33 XRF self-absorption. In Fig. S3bc-d, we show elements for which the intercomparison  
34 shows significant biases and/or no significant correlation between RDI and filters.  
35 Note that the elements exhibiting good agreement in Fig. 3a-b span orders of  
36 magnitude difference in concentration (and fluorescence counts), suggesting that  
37 there are no global or concentration-dependent biases in the RDI-SR-XRF data. For  
38 elements exhibiting lesser agreement (Fig. S3cb-d), this leaves the element relative  
39 calibration (i.e. element fluorescence yield as a function of line energy), spectral peak  
40 fitting, and instrument size cut points as potential sources of error in the XRF  
41 analysis.

42 Figure S3b shows good agreement for Na and Mg within a factor of 1.10-1.30 and  
43 good correlations (Pearson's *R* 0.89-0.99) despite the large correction of the RDI  
44 data due to self-absorption effects in the calibration standards and the coarse and  
45 intermediate ambient samples. This leads to significant uncertainty in the absolute  
46 concentrations of those elements. Furthermore, the XRF relative calibration curve for  
47 Na and Mg is difficult to constrain due to the low response of these elements, but  
48 only led to an uncertainty of 13 % (for Na-K compared to 2 % for Ca-Pb).

49 Figure S3bc shows good correlations for Mo (Pearson's *R* = 0.90), but the RDI  
50 measures a factor 2.4 higher concentrations than found on the filters, whereas ~~V and~~

1 | Ni shows no significant correlation between RDI and filters (Pearson's  $R$  0.56-0.66).  
 2 | The most likely reason for the discrepancy between both methods is the ICP-MS  
 3 | extraction efficiency. This was 66 % for Ni, but unknown for ~~V and Mo~~, leading to  
 4 | increased uncertainties in the absolute concentrations of the filter data ~~and potentially~~  
 5 | ~~underestimated concentrations~~. As shown in the main text, the RDI time series of  
 6 | these elements (including both urban/kerb increments and diurnal/weekly cycles) are  
 7 | consistent with those of elements expected to be co-emitted by the same sources.  
 8 | Visual inspection of the spectrum indicates that significant interferences between  
 9 | lines are unlikely, and this is confirmed by peak fitting sensitivity tests investigating  
 10 | the response of the calculated concentrations to uncertainties in line energy  
 11 | calibration (i.e. energy as a function of detector channel). We estimate a 3 %  
 12 | uncertainty in the measurement of Mo due to spectral analysis and an overall  
 13 | uncertainty of 21 %. Mo falls in a well-constrained region of the calibration curve  
 14 | (although is not directly measured on calibration foils), so relative calibration errors  
 15 | would require a systematic bias across this entire region of the calibration curve.  
 16 | While there are not enough jointly measured elements within the intercomparison to  
 17 | evaluate this possibility, good agreement between RDI and filter measurements is  
 18 | obtained through Sr ( $K\alpha = 14.1$  keV) and at Sb ( $K\alpha = 26.4$  keV) (Mo  $K\alpha$  lines fall at  
 19 | 17.5 keV), suggesting such a bias is unlikely. Spectral analysis uncertainties are 6 %  
 20 | ~~for Ni are somewhat higher for V and Ni with about 19 % for V and 6 % for Ni~~ (overall  
 21 | uncertainty ~~ies~~ of 28 and 22 %). Unlike Mo, the relative calibration is well-constrained  
 22 | both in terms of elements directly measured on calibration foils and in terms of  
 23 | intercomparison with nearby elements in the XRF calibration curve, where ~~V falls just~~  
 24 | ~~above Ca and Ti and just below Mn and Fe, and Ni falls~~ just above Mn and Fe and  
 25 | just below Cu and Zn. RDI and filter measurements are shown to be in good  
 26 | agreement for these six elements in Fig. S3a.

27



28

1 **Figure S3.** Total PM<sub>10</sub> element mass concentrations measured by the RDI (sum of PM<sub>10-2.5</sub>,  
 2 PM<sub>2.5-1.0</sub> and PM<sub>1.0-0.3</sub> fractions) at MR and NK averaged to 24 h versus 24 h PM<sub>10</sub> filter  
 3 measurements of elements for (a) elements that agree within ± 50 %, (b) elements that agree  
 4 but have a higher uncertainty due to self-absorption corrections, (c) elements with poor  
 5 correlations, ~~(c) elements with good correlations but a factor 2.5 higher with RDI~~, (d) other  
 6 elements. The one-to-one line is added in black. See Table S2 for fit coefficients and  
 7 Pearson's *R* values. Note that many elements are scaled to improve visualization.

8  
 9 **Table S2.** Fit coefficients and Pearson's *R* values for elements measured with the RDI (PM<sub>10-  
 10 2.5</sub>, PM<sub>2.5-1.0</sub> and PM<sub>1.0-0.3</sub> fractions summed to total PM<sub>10</sub> and averaged to 24 h) relative to 24 h  
 11 PM<sub>10</sub> filter measurements. Data points were fitted with an orthogonal fit and forced zero  
 12 intercept.  
 13

Element	Fit coefficient	Pearson's <i>R</i>
Na	<u>2-821.30</u>	0.89
Mg	<u>2-341.09</u>	0.99
Al	<u>4-550.89</u>	0.89
K	0.55	0.78
Ca	0.81	0.94
Ti	1.04	0.86
V	0.17	0.66
Mn	1.37	0.91
Fe	0.95	0.96
Ni	0.71	0.56
Cu	1.30	0.95
Zn	0.70	0.94
Sr	1.21	0.78
Mo	2.35	0.90
Sn	0.43	0.98
Sb	1.18	0.93
Ba	1.36	0.94
Pb	0.34	0.61

14  
 15 ~~Figure S3c shows good correlations for Na and Mg (Pearson's *R* > 0.89), but the RDI~~  
 16 ~~concentrations are a factor 2.5 higher than the filters. The two measurement~~  
 17 ~~techniques each provide internally consistent results, with the Mg to Na ratio for the~~  
 18 ~~filter data at NK of 0.13 and the RDI data at NK and MR of 0.12, both of which are in~~  
 19 ~~very good agreement with the theoretical sea salt ratio of 0.12. The XRF relative~~  
 20 ~~calibration curve for Na and Mg is difficult to constrain due to the low response of~~  
 21 ~~these elements, but only led to an uncertainty of 13 % (for Na-K compared to 2 % for~~  
 22 ~~Ca-Pb). The extraction efficiency for Mg in ICP-MS was 90 %, which does not explain~~  
 23 ~~the discrepancy between both methods, but was unknown for Na. Unfortunately, it~~  
 24 ~~remains unclear why the results of both methods differ for these two elements on an~~  
 25 ~~absolute scale. But since most analyses in the main text focus on relative~~  
 26 ~~changes/ratios per element across sites, the conclusions remain unaffected~~  
 27 ~~independent by the exact absolute concentrations.~~

28 The elements K, V, Sn and Pb in Fig. S3d show good-reasonable correlations  
 29 between RDI and filter measurements (Pearson's *R* > 0.~~7861~~) but the RDI data is  
 30 less than half the filter data (filter measurements of K and Sn only at NK). Pb has a  
 31 significant fraction of the mass in the fine fraction (see Fig. 2 in main text).  
 32 Underestimation by the RDI is explained by its small-end cut point of 290-410 nm.  
 33 Typically, K, V and Sn are also mainly emitted in the fine fraction~~also have a~~  
 34 ~~significant fraction of their mass in the fine fraction~~, and might be affected by the cut  
 35 off similarly to Pb.

1 S is a useful element for evaluation of the small-end cut off, as it is dominant in the  
2 fine fraction and measurable by several techniques. Therefore, we compared S data  
3 obtained with the RDI to simultaneous S mass calculated from sulphate ( $\text{SO}_4$ )  
4 measured by an AMS at MR, NK, and DE. The results in Supplement A show that the  
5 S mass in the RDI is on average about three times lower than that measured by the  
6 AMS. This is consistent with the difference between RDI and filter measurements for  
7 fine fraction dominated elements. The RDI backup filter, which collects particles too  
8 small to impact at the  $\text{PM}_{1.0-0.3}$  stage, was analysed for  $\text{SO}_4^{2-}$  using ion  
9 chromatography (Supplement A). Adding the S from this analysis to the S collected  
10 at the RDI  $\text{PM}_{1.0-0.3}$  stage yielded mass closure with the S from AMS measurements  
11 within 25 % at all three sites. This suggests that elements with considerable mass in  
12 the small end of the  $\text{PM}_{1.0}$  size range are not sampled by the  $\text{PM}_{1.0-0.3}$  stage. This  
13 affects S and Pb, and potentially also K, V, Zn, Br and Sn. To further investigate this  
14 effect, new RDI collection efficiency measurements for the  $\text{PM}_{1.0}$  deposition stage  
15 were performed (Supplement A). The actual small-end cut off was determined to be  
16 290-410 nm, rather than the previously measured value of 100 nm (Bukowiecki et al.,  
17 2009c; Richard et al., 2010), and found to be very sensitive to the machining  
18 tolerances of the  $\text{PM}_{1.0}$  nozzle.

19 Only a small fraction of the measured elements are affected by this cut off issue in  
20 the sense that absolute values are smaller than with a  $\text{PM}_{1.0-0.1}$  stage. Further,  
21 because the analyses presented in the main text depends on site-to-site ratios (for  
22 the same element) and relative concentration changes, potential biases are reduced  
23 by the similar (though not identical, see Fig. S2 in Supplement A) cut offs of the  
24 different RDI units. The conclusions presented in the main text are thus not  
25 significantly affected by this artefact.

26  
27

1 **Table S3.** Estimated total uncertainty (% of measured value) of the calculated element  
 2 concentrations per size fraction, and detection limits for each element ( $\text{ng m}^{-3}$ ).

Element	PM <sub>10-2.5</sub> (%) <sup>a</sup>	PM <sub>2.5-1.0</sub> (%) <sup>a</sup>	PM <sub>1.0-0.3</sub> (%) <sup>a</sup>	DL ( $\text{ng m}^{-3}$ ) <sup>b</sup>
Na <sup>c</sup>	<u>2559</u>	<u>2559</u>	<u>2560</u>	2.552
Mg	<u>2455</u>	<u>2455</u>	<u>2455</u>	0.962
Al	<u>2448</u>	<u>2548</u>	<u>2548</u>	1.709
Si	<u>2443</u>	<u>2443</u>	<u>2443</u>	0.420
P	25	25	25	0.118
S	24	24	24	0.503
Cl	24	24	24	0.158
K	24	24	24	0.031
Ca	21	21	21	0.267
Ti	24	26	27	0.024
V	30	30	24	0.008
Cr	27	27	26	0.015
Mn	83	69	46	0.042
Fe	21	21	21	0.033
Ni	22	22	21	0.005
Cu	21	21	21	0.028
Zn	21	21	21	0.058
Br	21	21	21	0.117
Sr	21	21	21	0.036
Zr	21	21	21	0.036
Mo	21	21	21	0.037
Sn	21	21	21	0.061
Sb	21	21	21	0.052
Ba	21	21	21	0.254
Pb	21	21	21	0.137

3 <sup>a</sup> Combination of uncertainties regarding sample inhomogeneity (20 %), self-absorption  
 4 corrections (Na-Si 54-35 %)<sup>d</sup>, RDI flow rate (5 %), absolute and relative calibration (Na-K 13  
 5 %, Ca-Pb 2 %) and spectral analysis specific per element and size fraction (median  
 6 uncertainties for all data points).

7 <sup>b</sup> Taken asAs 3x the standard deviation of the spectra signals used for continuum corrections.

8 <sup>c</sup> Na uncertainties might be underestimated due to the overlap with the L lines of Ni, Cu and  
 9 Zn. In the current analysis the ratio of the L $\alpha$  to K $\alpha$  lines are determined empirically, and  
 10 quantification of the associated uncertainties is under investigation.

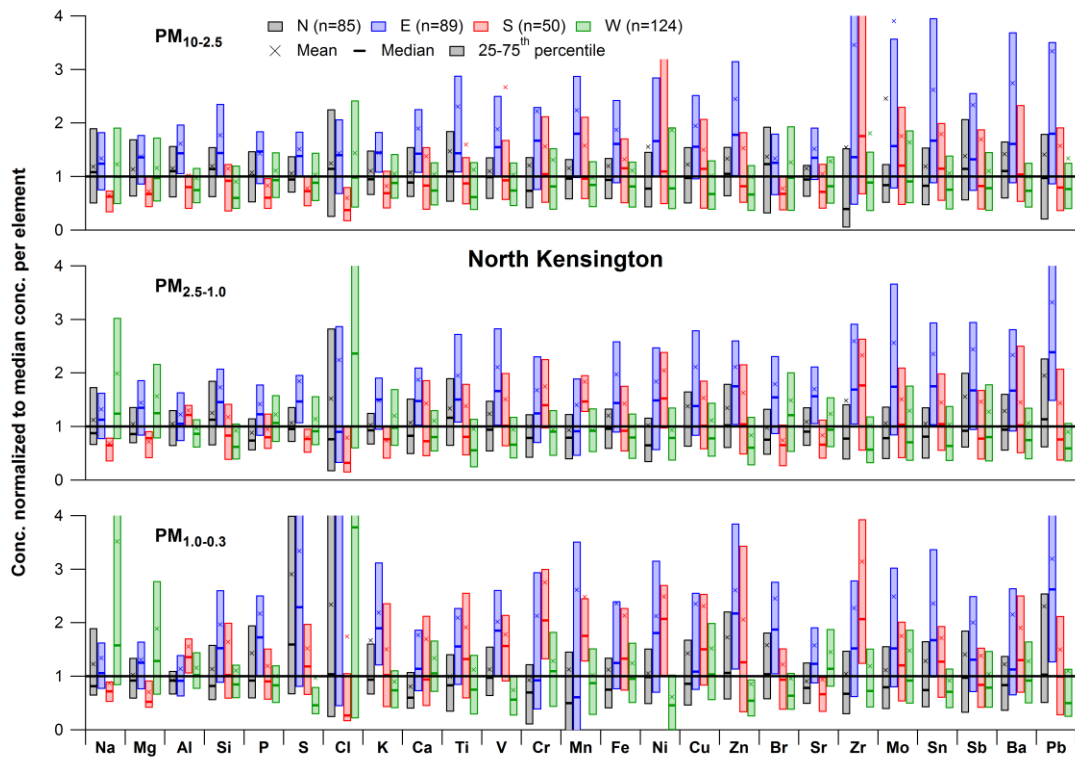
11 <sup>d</sup> Uncertainties regarding self-absorption corrections are based on the microscopic analysis of  
 12 the particle size on the calibration standards. The particle size of the dried droplets shows a  
 13 geometric mean of the volume size distribution of 9  $\mu\text{m}$ , and 50 % of the particles are in the  
 14 range 4-14  $\mu\text{m}$ .

15

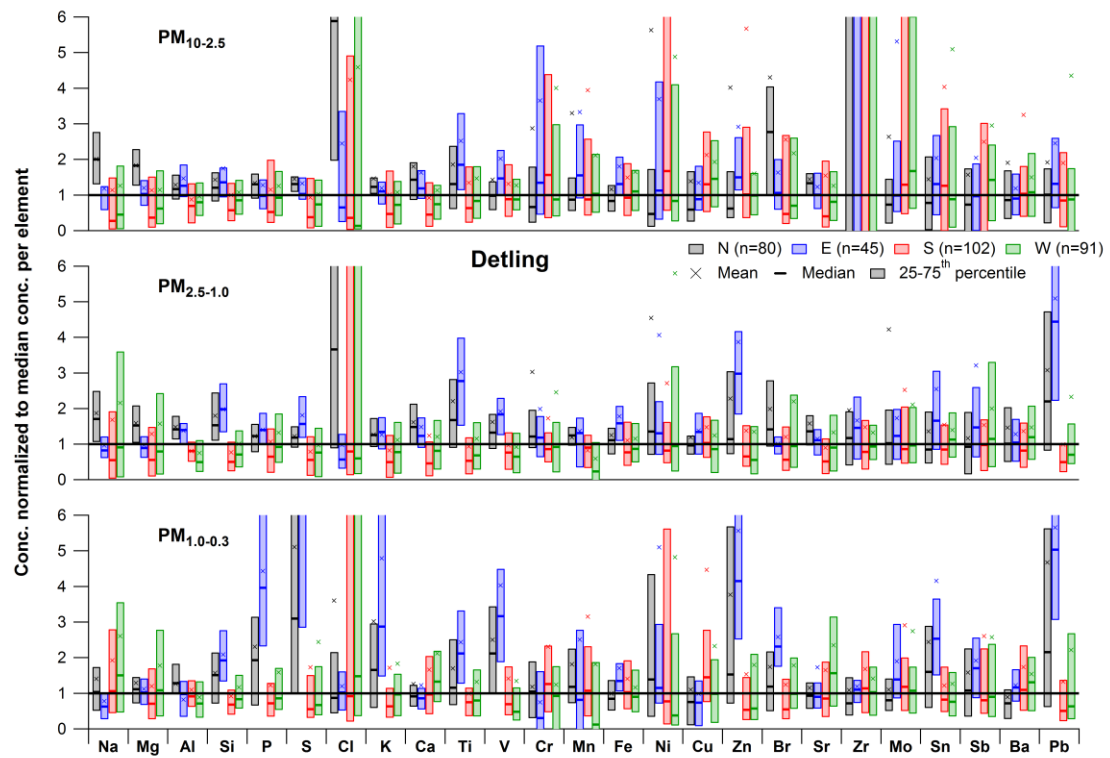
16



1 **Supplement D: Additional tables and figures**

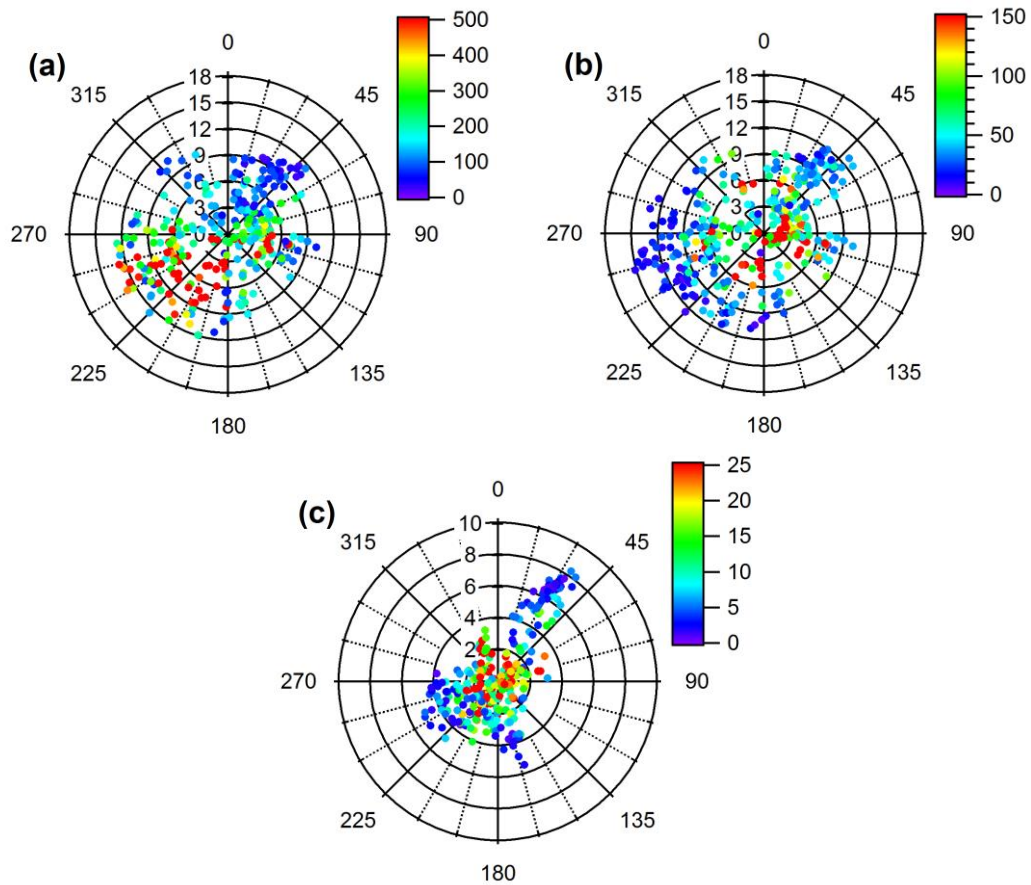


2  
 3 **Figure S4.** Same as Fig. 4 in main text, but for NK with mean, median and 25-75th percentile  
 4 trace element concentrations split in four wind direction sectors (N, E, S, W) normalized to the  
 5 global median concentration per element for  $PM_{10-2.5}$  (top),  $PM_{2.5-1.0}$  (middle) and  $PM_{1.0-0.3}$   
 6 (bottom). See Sect. 4.2.2 for the definition of the wind direction sectors.



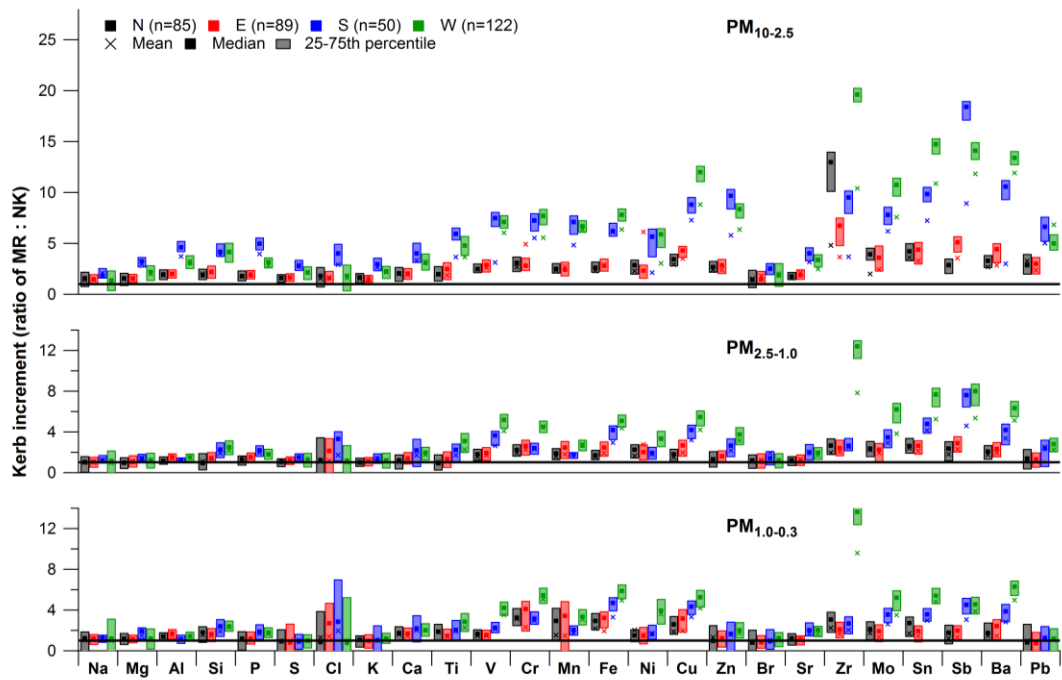
1  
2  
3  
4  
5  
6

**Figure S5.** Same as Fig. 4, but for DE with mean, median and 25-75th percentile trace element concentrations split in four wind direction sectors (N, E, S, W) normalized to the global median concentration per element for  $PM_{10-2.5}$  (top),  $PM_{2.5-1.0}$  (middle) and  $PM_{1.0-0.3}$  (bottom). See Sect. 4.2.2 for the definition of the wind direction sectors.

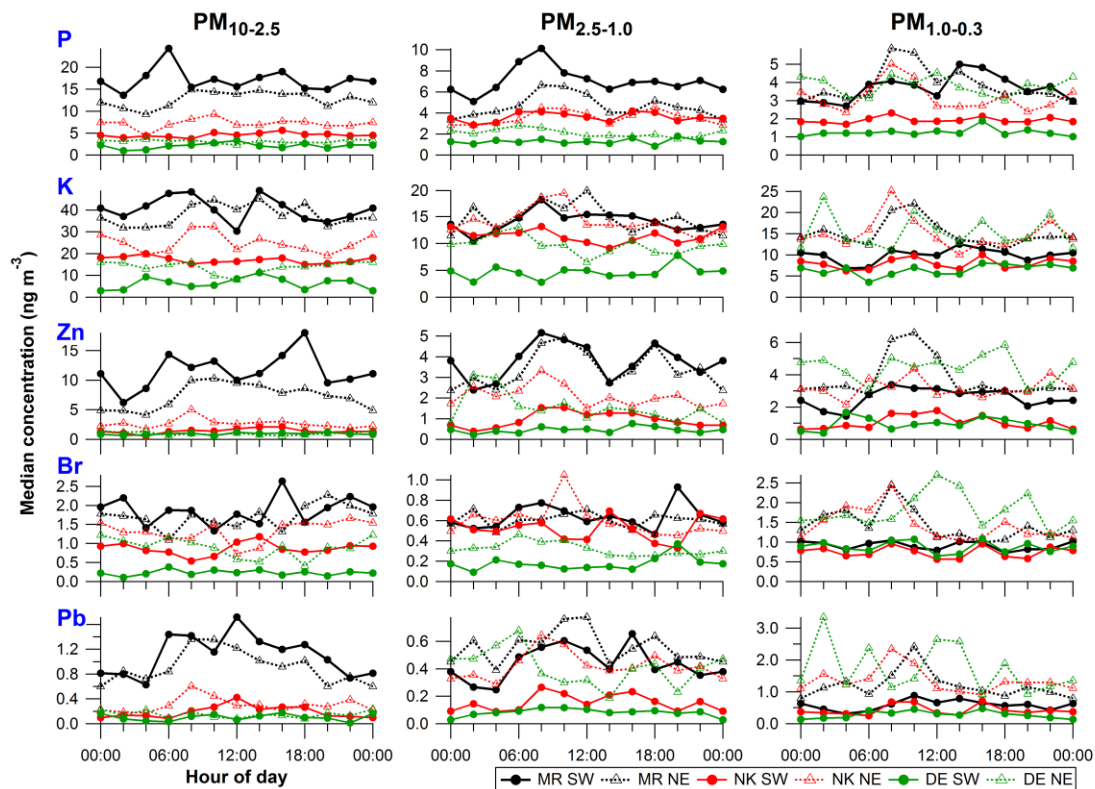


1  
2  
3  
4  
5  
6  
7

**Figure S6.** Wind roses as a function of wind direction (angle) and wind speed (diameter) at (a) BT Tower, color-coded by NO<sub>x</sub> concentrations (ppb) at MR, (b) BT Tower, color-coded by NO<sub>x</sub> concentrations (ppb) at NK, (c) DE, color-coded by NO<sub>x</sub> concentrations (ppb) at DE for the RDI sampling periods (see Table 1 in main text).

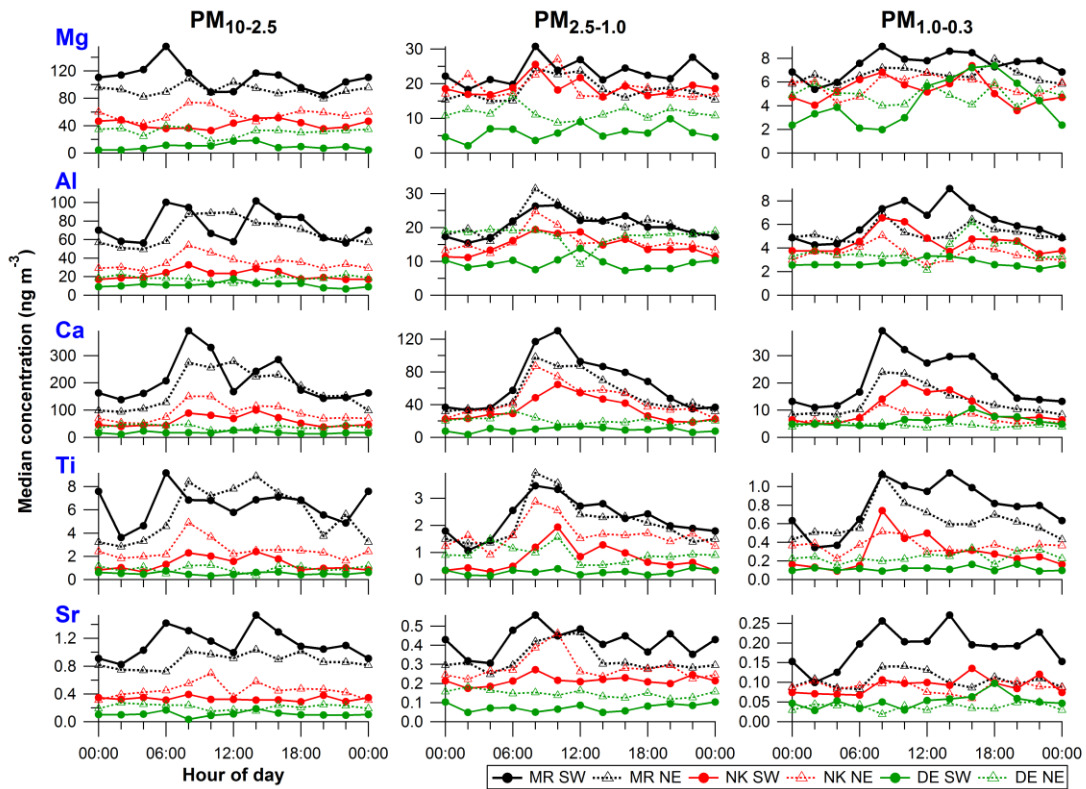


1  
 2 **Figure S7.** Same as Fig. 5, but with mean, median and 25-75th percentile kerb increment  
 3 values for trace elements at MR relative to NK for PM<sub>10-2.5</sub> (top), PM<sub>2.5-1.0</sub> (middle) and PM<sub>1.0-0.3</sub>  
 4 (bottom) split in N, E, S and W wind sectors. See Sect. 4.2.2 for the definition of the wind  
 5 direction sectors.  
 6



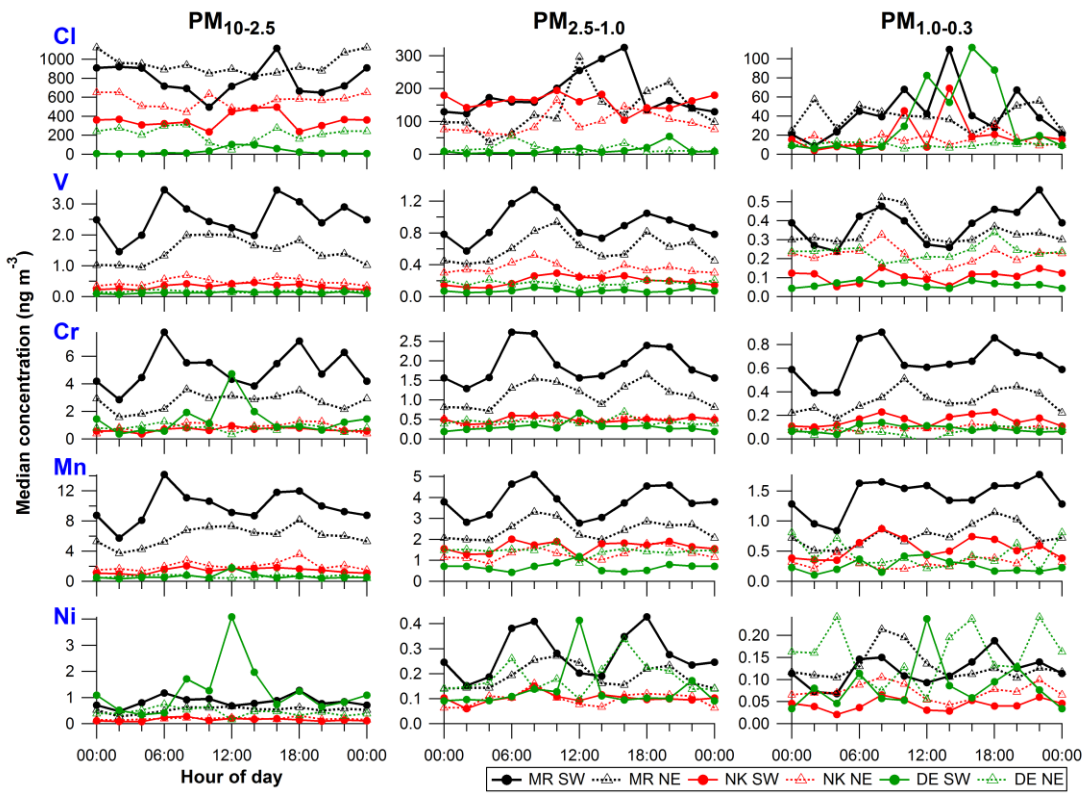
1  
2  
3  
4  
5  
6  
7  
8

**Figure S8.** Same as Fig. 6, but for all other elements: P, K, Br, Zn, Pb (regional background); Mg (sea salt), Al, Ca, Ti, Sr (mineral dust); Cl (sea salt), V, Cr, Mn, Ni (traffic-related); Cu, Zr, Mo, Sn, Ba (brake wear). Diurnal cycles of 2 h median concentrations for PM<sub>10-2.5</sub> (left), PM<sub>2.5-1.0</sub> (middle) and PM<sub>1.0-0.3</sub> (right) at MR, NK, DE split in SW and NE wind sectors. See Sect. 4.2.2 for the definition of the wind direction sectors. Hour of day is start of 2 h sampling period, so 00:00 LT means sampling from 00:00 to 02:00 LT.



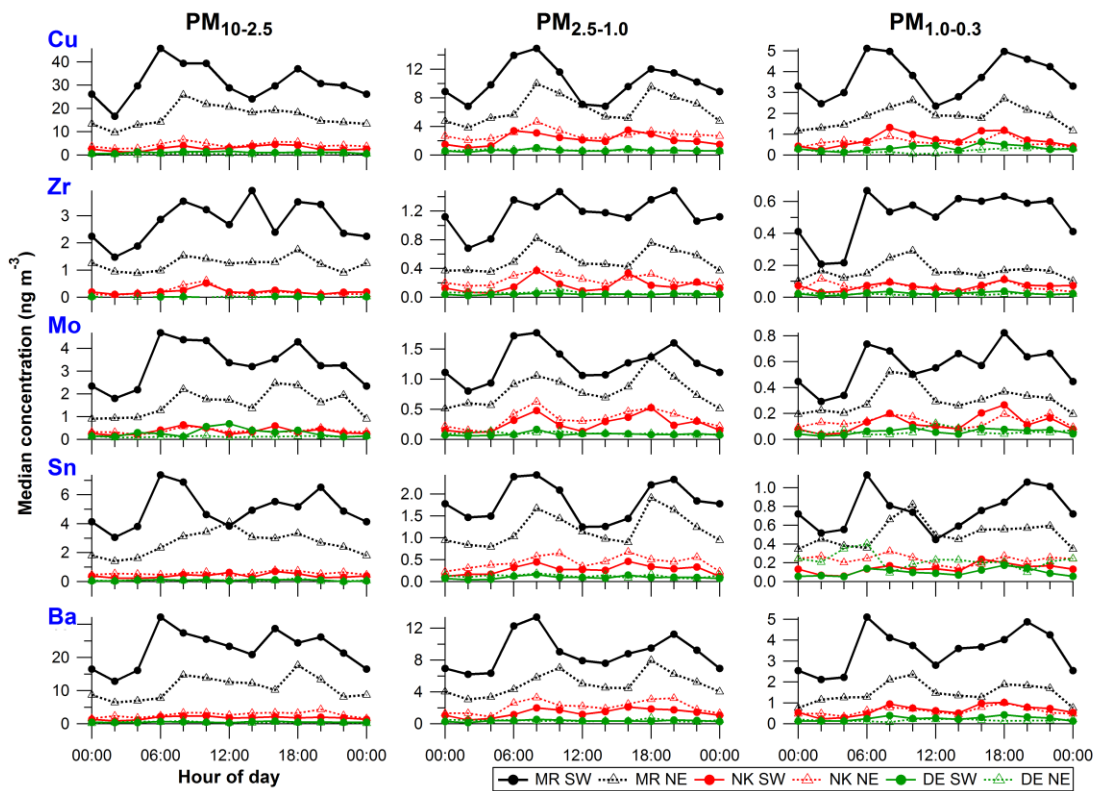
1  
2  
3

Figure S8. Continued.



4  
5

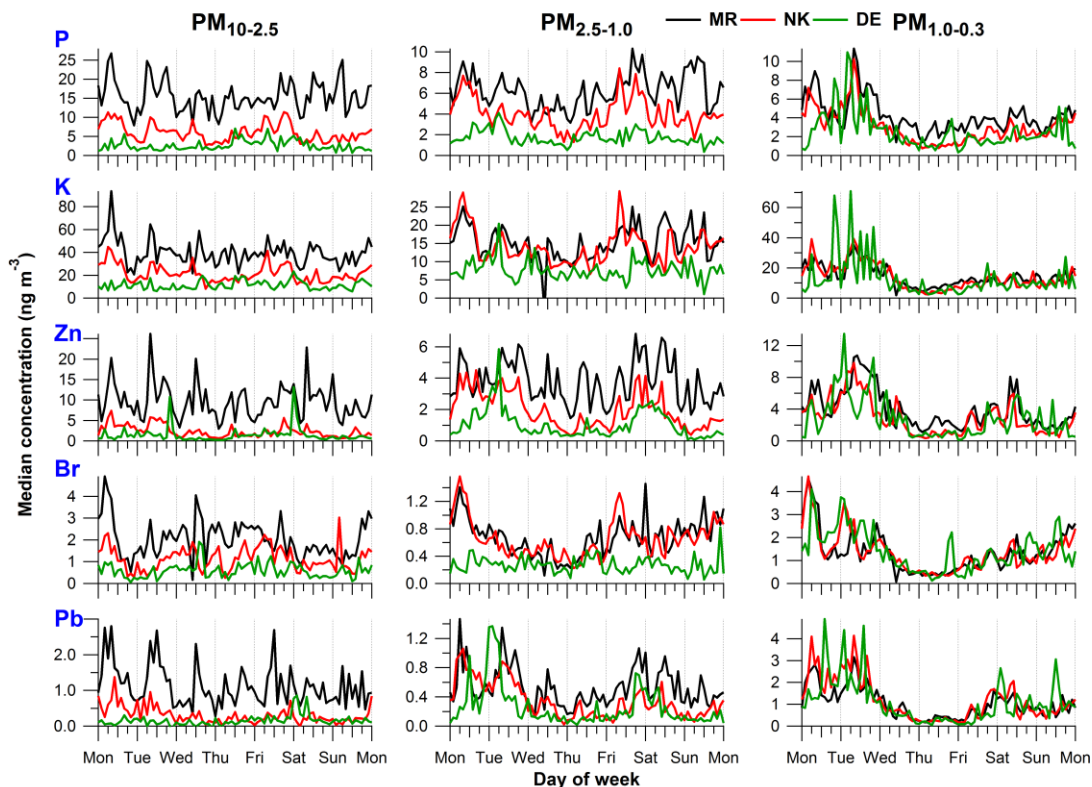
Figure S8. Continued.



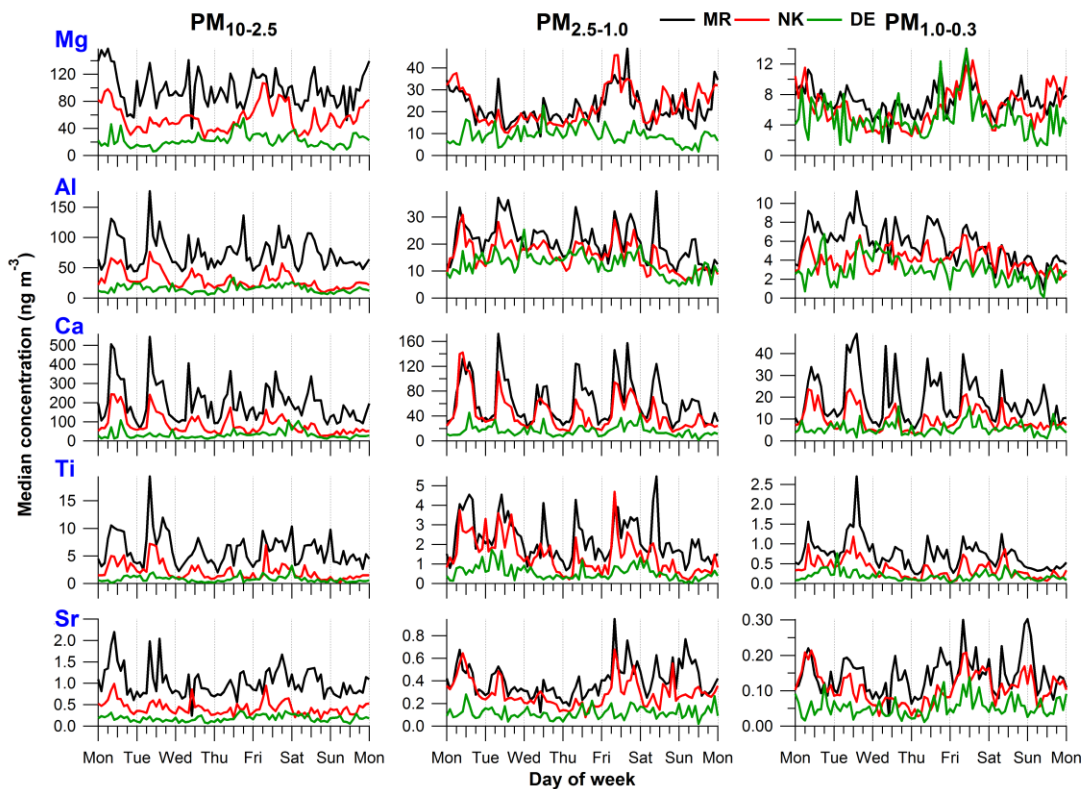
1  
2  
3  
4

Figure S8. Continued.



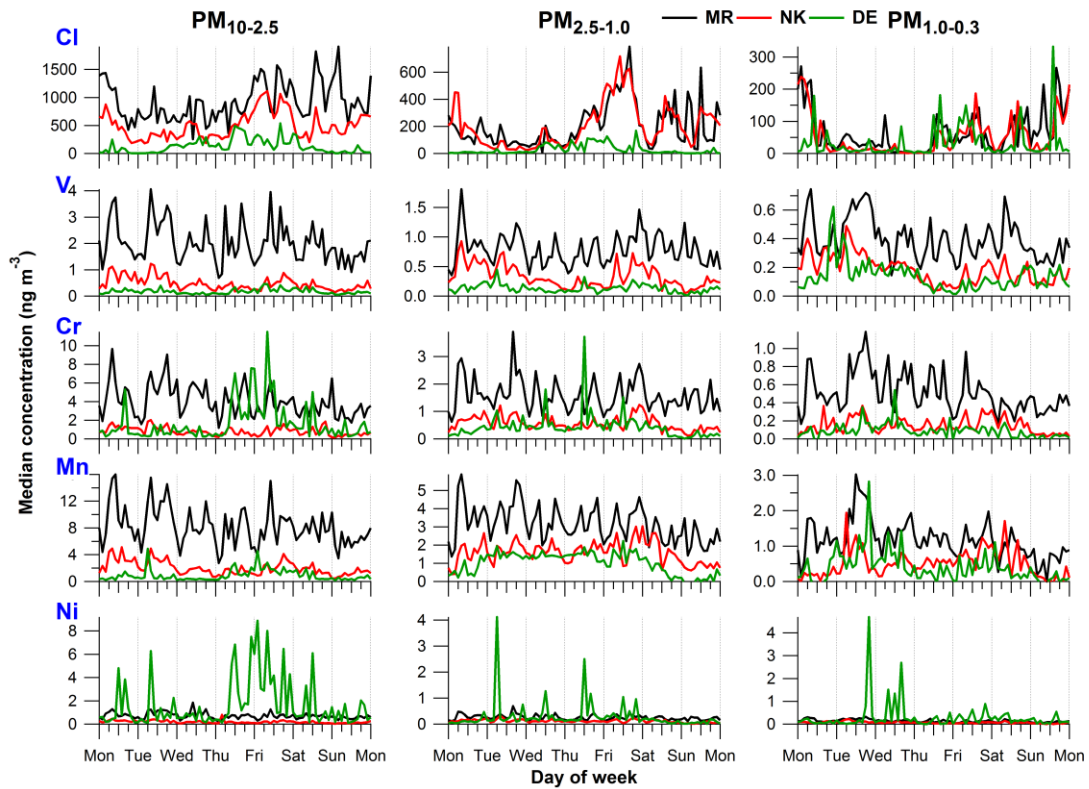


1  
 2 **Figure S9.** Same as Fig. 7, but for all other elements: P, K, Br, Zn, Pb (regional background);  
 3 Mg (sea salt), Al, Ca, Ti, Sr (mineral dust); Cl (sea salt), V, Cr, Mn, Ni (traffic-related); Cu, Zr,  
 4 Mo, Sn, Ba (brake wear). Weekly cycles of 2 h median concentrations for PM<sub>10-2.5</sub> (left), PM<sub>2.5-</sub>  
 5 1.0 (middle) and PM<sub>1.0-0.3</sub> (right) at MR, NK, DE.



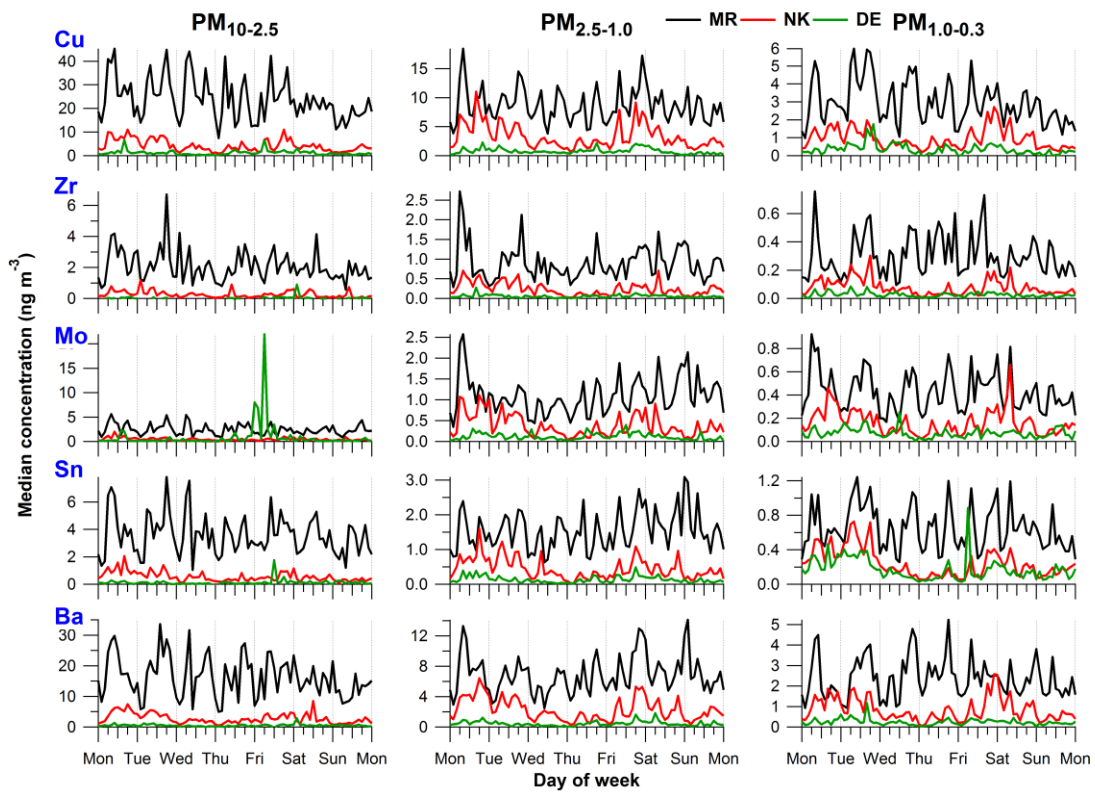
6  
 7 **Figure S9.** Continued.





1  
2  
3

Figure S9. Continued.



4  
5  
6

Figure S9. Continued.

1 **References**

- 2 Bearden, J. A.: X-ray wavelengths, *Rev. Mod. Phys.*, 39, 78-124,  
3 doi:10.1103/revmodphys.39.78, 1967.
- 4 Bukowiecki, N., Hill, M., Gehrig, R., Zwicky, C. N., Lienemann, P., Hegedus, F.,  
5 Falkenberg, G., Weingartner, E., and Baltensperger, U.: Trace metals in ambient air:  
6 Hourly size-segregated mass concentrations determined by synchrotron-XRF,  
7 *Environ. Sci. Technol.*, 39, 5754-5762, 2005.
- 8 Bukowiecki, N., Lienemann, P., Zwicky, C. N., Furger, M., Richard, A., Falkenberg,  
9 G., Rickers, K., Grolimund, D., Borca, C., Hill, M., Gehrig, R., and Baltensperger, U.:  
10 X-ray fluorescence spectrometry for high throughput analysis of atmospheric aerosol  
11 samples: The benefits of synchrotron X-rays, *Spectrochim. Acta B*, 63, 929-938,  
12 2008.
- 13 Bukowiecki, N., Richard, A., Furger, M., Weingartner, E., Aguirre, M., Huthwelker, T.,  
14 Lienemann, P., Gehrig, R., and Baltensperger, U.: Deposition uniformity and particle  
15 size distribution of ambient aerosol collected with a rotating drum impactor, *Aerosol*  
16 *Sci. Technol.*, 43, 891-901, 2009.
- 17 DeCarlo, P. F., Slowik, J. G., Worsnop, D. R., Davidovits, P., and Jimenez, J. L.:  
18 Particle morphology and density characterization by combined mobility and  
19 aerodynamic diameter measurements. Part 1: Theory, *Aerosol Sci. Technol.*, 38,  
20 1185-1205, doi:10.1080/027868290903907, 2004.
- 21 Richard, A., Bukowiecki, N., Lienemann, P., Furger, M., Fierz, M., Minguillon, M. C.,  
22 Weideli, B., Figi, R., Flechsig, U., Appel, K., Prevot, A. S. H., and Baltensperger, U.:  
23 Quantitative sampling and analysis of trace elements in atmospheric aerosols:  
24 impactor characterization and synchrotron-XRF mass calibration, *Atmos. Meas.*  
25 *Tech.*, 3, 1473-1485, 2010.
- 26 Sole, V. A., Papillon, E., Cotte, M., Walter, P., and Susini, J.: A multiplatform code for  
27 the analysis of energy-dispersive X-ray fluorescence spectra, *Spectrochim. Acta B*,  
28 62, 63-68, 2007.
- 29 Van Espen, P., Janssens, K., and Nobels, J.: AXIL-PC, software for the analysis of  
30 complex X-ray spectra, *Chemometrics Intell. Lab. Syst.*, 1, 109-114, 1986.
- 31  
32